"I learned very early the difference between knowing the name of something and knowing something"

Richard P. Feynman

"The most exciting phrase to hear in science, the one that heralds new discoveries, is not 'Eureka!' (I found it!) but 'That's funny...' "

Isaac Asimov

University of Alberta

An Investigation of Magnetically Active Terahertz Devices

by

Cameron Joseph Edgar Straatsma

A thesis submitted to the Faculty of Graduate Studies and Research in partial fulfillment of the requirements for the degree of

Master of Science

in

Photonics and Plasmas

Department of Electrical and Computer Engineering

Fall 2011
Edmonton, Alberta

To my family, for all your love and support

Abstract

This thesis work focuses on the investigation of utilizing magnetoresistance phenomena in ferromagnetic metals to control the propagation of terahertz electromagnetic radiation confined to subwavelength structures. The purpose of this investigation is to study these phenomena as a potential candidate for use in active plasmonic devices at terahertz frequencies. To accomplish this task, a terahertz time-domain spectroscopy system incorporating a high field strength electromagnet is designed, built and characterized. Next, the effects of particle size on the near-field coupling of localized surface plasmon modes in a random terahertz plasmonic metamaterial are presented. Following this, evidence is given for the use of the giant magnetoresistance effect in modulating the transparency of a random terahertz plasmonic metamaterial. The final study utilizes the new terahertz time-domain spectroscopy system to investigate the effects of magnetoresistance on the electromagnetic response of periodic terahertz plasmonic metamaterials.

Acknowledgements

First and foremost, I would like to graciously thank my supervisor, Prof. Abdul Y. Elezzabi, for his unwavering help and support over the course of this degree. His endless encouragement, helpful criticisms and passion for science have greatly helped me develop as a researcher.

Secondly, I would like to extend my appreciation to Prof. Jan A. Jung and Prof. Kim H. Chow for providing access to their laboratory and deposition equipment. In particular, I would like to thank Mohamed Elsayed for taking time out of his busy schedule to help me make samples on countless occasions.

I would also like to acknowledge Dr. Mark Johnson of the Naval Research Laboratory for his helpful discussions and insights.

Thank you to the excellent academic and administrative support staff of the Electrical and Computer Engineering department. In particular, I would like to acknowledge the excellent work of Herbert Dexel, Reiner Schwarze and Martin Riedner in the machine shop, whose expertise, endless patience and friendly demeanor has helped me complete much of my thesis work.

Let me not forget the wonderful company of my colleagues who were there throughout the course of my degree: Pouya Maraghechi, Shawn Sederberg, Mike Startsev and Corey Baron. I wish you all the best in future endeavours.

Finally, I would like to thank my family for their continued support throughout the course of my studies.

Contents

List of Tables

List of Figures

List of Symbols and Abbreviations

Fundamental Constants

$\epsilon_0 = 8.854187817 \times 10^{-12}$ F/m	electric permittivity of vacuum
$\mu_0 = 4\pi \times 10^{-7}$ H/m	magnetic permeability of vacuum
$c = 2.99792458 \times 10^{8}$ m/s	speed of light in vacuum
$q_e \approx -1.60217657^{-19}$ C	elementary charge of an electron

Symbols

$\mathbf{M}$	magnetization
$\mathbf{P}$	polarization
ρ_b	bound charge
$\mathbf{J}_b$	bound current
$\mathbf{E}$	electric field
$\mathbf{B}$	magnetic induction
$\mathbf{D}$	electric displacement
ρ_f	free charge
$\mathbf{H}$	magnetic field
$\mathbf{J}_f$	free current

χ_e	electric susceptibility
χ_m	magnetic susceptibility
ϵ	electric permittivity
μ	magnetic permeability
σ	electric conductivity
σ_f	free surface charge density
$\mathbf{K}_f$	free surface current density
$\tilde{\mathbf{k}}$	wavevector
$\mathbf{r}$	position
ω	angular frequency
ϕ	phase
$\tilde{n}$	refractive index
m^*	effective mass of electron
γ	resonance damping rate
$\mathbf{a}$	acceleration
$\mathbf{v}$	velocity
$\mathbf{p}$	dipole moment
N	number of electrons per unit volume
f	resonance strength
ω_p	plasma frequency
k_z	SPP wavevector
ω_{SP}	surface plasmon frequency
L	SPP energy attenuation length
α	SPP energy confinement factor
λ	wavelength
Φ	electric potential
P_l	Legendre polynomials of order l

E_F	Fermi energy
$\mathbf{M}_s$	saturation magnetization
$\mathbf{M}_r$	remanent magnetization
$\mathbf{H}_c$	coercive field
ρ_0	background resistivity
$\rho_{Lorentz}$	Lorentz force contribution to resistivity
ρ_{AMR}	anisotropic magnetoresistance contribution to resistivity
R	electrical resistance
f_{SPP}	surface plasmon polariton resonance frequency
f_{HW}	half-wavlength resonance frequency
f_{SRR}	split ring resonator resonance frequency
T	transmission coefficient
δ_{skin}	radiation absorption skin depth
σ^*	magnetic conductivity
$\mathbf{J}_p$	electric polarization current density

Abbreviations

2D	two dimensional
3D	three dimensional
ADE	auxiliary differential equation
AF	antiferromagnetic
AMR	anisotropic magnetoresistance
ASE	amplified spontaneous emission
a.u.	arbitrary units
BS	beam splitter
CW	continuous wave

ECDC	extra-cavity dispersion compensation
EEMR	electrically excited magnetic resonance
EMT	effective medium theory
EO	electro-optic
FDTD	finite-difference time-domain
FL	free layer
FM	ferromagnetic
FWHM	full-width at half-maximum
GMR	giant magnetoresistance
GUI	graphical user interface
HM	hard magnet
OC	output coupler
PC	photoconductive
PL	pinned layer
RKKY	Ruderman-Kittel-Kasuya-Yosida
RR	retro reflector
SEM	scanning electron microscopy
SL	spacer layer
SM	soft magnet
SNR	signal-to-noise ratio
SRR	split ring resonator
TE	transverse electric
THz	terahertz
THz-TDS	terahertz time-domain spectroscopy
TM	transverse magnetic
WP	Wollaston prism

Chapter 1

Introduction

1.1 Motivation

The growing demand for high-speed, high-bandwidth information technology has led to an increased research interest in exploring alternative, light-based technologies. Electronic elements based on semiconductor device technology represent the heart of modern day information processing. However, there exists an inherent bottleneck in these technologies such that researchers worldwide have begun to actively pursue the development of photonic elements for next generation communication and computing devices. Novel subwavelength, active photonic device architectures can be implemented by utilizing the principles of spinplasmonics. Here, the electron spin state is used to modulate electromagnetic radiation confined to subwavelength metallic structures. Electron spin-based photonic devices create a number of new possibilities for photonic circuitry, particularly in the implementation of photonic-based memories and data storage. Thus, the work outlined in this thesis represents an investigation of electron spin-based photonic devices operating in the terahertz (THz) regime.

In the the THz frequency range there is an inherent lack of materials which exhibit a natural electromagnetic response. To fill this void, a significant research effort focused on the development of artificial materials is underway. These materials, known as metamaterials, provide researchers with a way to engineer the electromagnetic response of matter. Metamaterials offer a number of degrees of freedom in their design allowing for unprecedented control over light, and, because of this, they represent the next generation of photonic-based devices. In particular, plasmonic metamaterials have been proposed for a number of applications including sub-wavelength microscopy [1, 2] and even cloaking [3]. Furthermore, both periodic and randomly ordered structures have been utilized as plasmonic metamaterials in the THz regime. In terms of periodic metamerials, planar metallic resonators have shown potential as both THz filters [4–6] and thin-film sensors [7, 8]. On the other hand, random plasmonic metamaterials were studied extensively by Chau et al., who performed a series of experiments demonstrating the transparency of a random ensemble of subwavelength metallic microparticles to THz radiation [9, 10]. Furthermore, they successfully modulated this transparency via magnetoresistance effects in ferromagnetic media [11–13] demonstrating a potential candidate for active THz devices. It is this mechanism for active control over THz electromagnetic radiation that is of interest in the current study.

THz radiation is attractive because it possesses a number of desirable characteristics, which has lead to the widespread use of THz time-domain spectroscopy (THz-TDS) for a number of different applications. Specifically, it has a low penetration depth, non-ionizing radiation and a large number of organic compounds exhibit characteristic spectral "fingerprints" in this frequency range. Also, due to the large wavelengths in the THz regime ($\sim$ 10 µm $-$ 3 mm) fabrication processes are generally straightforward and simple

to execute with present day micro- and nanofabrication technologies. However, perhaps the most useful attribute of THz-TDS is that it is inherently a time-domain technique allowing for direct detection of both the amplitude and phase of the electric field vector. This allows for straightforward characterization of the ultrafast electric response of materials effectively eliminating the need for tedious Kramers-Kronig analysis [14], which is typically used to find the complex permittivity of a material. In addition, coherent sampling schemes provide polarization sensitive detection allowing for further characterization of materials and devices. All of these properties make THz-TDS an extremely attractive technique in the development of modern day THz technologies, hence its inclusion in this thesis work.

The thesis presented here investigates a class of active plasmonic metamaterials using THz-TDS. These metamaterials incorporate ferromagnetic metals such that their electromagnetic response can be altered by the application of an external magnetic field. Therefore, the purpose of this work is to investigate the use of magnetoresistance phenomena as a tool for the active control of THz electromagnetic radiation. The goals of this thesis work are to: (1) design and construct a THz-TDS system incorporating a high field strength electromagnet and (2) use this system to study the effects of magnetoresistance phenomena on the electromagnetic response of subwavelength metallic structures at THz frequencies.

1.2 Theoretical Framework

The following subsections are meant to provide the reader of this thesis work with a background on the subsequent chapters and the motivation behind them. It is meant to be a refresher and is far from exhaustive. The interested

reader should consult the provided references as well as any number of textbooks on the subjects. In terms of textbooks, Griffiths [15] and Jackson [16] are the standard for electrodynamics theory; for plasmonics Maier [17] provides the most recent comprehensive survey on theory and applications; for solid-state physics theory Kittel [18], Ashcroft and Mermin [19] and Marder [20] are all well-known; and for magnetism theory and magnetic devices Spaldin [21] provides a good introductory survey.

1.2.1 Classical Electrodynamics in Matter

When electromagnetic fields interact with matter they induce a net electric and magnetic dipole moment per unit volume, or a polarization, $\mathbf{P}$, and magnetization, $\mathbf{M}$, respectively. The result of $\mathbf{P}$ and $\mathbf{M}$ is an accumulation of bound charge and current within the material, which are governed by the relations

$$\rho_b = -\nabla \cdot \mathbf{P} \tag{1.2.1.1a}$$

$$\mathbf{J}_b = \nabla \times \mathbf{M} \tag{1.2.1.1b}$$

where ρ_b represents the bound charge density and $\mathbf{J}_b$ represents the bound current density. It is important to note that bound charges and currents are *induced* and; therefore, they depend solely on the microscopic properties of the material in which they reside. In this way, any charge and current that is not a result of polarization or magnetization is assumed to be free. It is these free charges and currents that give rise to the macroscopic electromagnetic fields

as defined through Maxwell's original set of equations

$$\nabla \times \mathbf{E} + \frac{\partial \mathbf{B}}{\partial t} = 0 \tag{1.2.1.2a}$$

$$\nabla \cdot \mathbf{D} = \rho_f \tag{1.2.1.2b}$$

$$\nabla \times \mathbf{H} - \frac{\partial \mathbf{D}}{\partial t} = \mathbf{J}_f \tag{1.2.1.2c}$$

$$\nabla \cdot \mathbf{B} = 0 \tag{1.2.1.2d}$$

Equations (1.2.1.2) describe how the macroscopic field quantities, $\mathbf{E}$ (electric field); $\mathbf{H}$ (magnetic field); $\mathbf{D}$ (electric flux density); and $\mathbf{B}$ (magnetic flux density), arise from densities of free charge, ρ_f, and free current, $\mathbf{J}_f$. It is these relations that govern the wide variety of phenomena that lie within the realm of classical electrodynamics.

The auxiliary field quantities, $\mathbf{D}$ and $\mathbf{B}$, conveniently account for any effects caused by the presence of materials since they include the polarization and magnetization in their definitions

$$\mathbf{D} = \epsilon_0 \mathbf{E} + \mathbf{P} \tag{1.2.1.3a}$$

$$\mathbf{B} = \mu_0 \left(\mathbf{H} + \mathbf{M} \right) \tag{1.2.1.3b}$$

where ϵ_0 and μ_0 represent the permittivity and permeability of freespace, respectively. When considering materials which are isotropic, homogeneous and linear with respect to the electromagnetic fields, $\mathbf{P}$ and $\mathbf{M}$ take on the following form

$$\mathbf{P} = \epsilon_0 \chi_e \mathbf{E} \tag{1.2.1.4a}$$

$$\mathbf{M} = \chi_m \mathbf{H} \tag{1.2.1.4b}$$

where χ_e and χ_m represent the electric and magnetic susceptibility of the material, respectively. By defining the electric permittivity, $\epsilon = \epsilon_0 (1 + \chi_e)$, and the magnetic permeability, $\mu = \mu_0 (1 + \chi_m)$, of the material, equations (1.2.1.3) are rewritten as

$$\mathbf{D} = \epsilon \mathbf{E} \tag{1.2.1.5a}$$

$$\mathbf{B} = \mu \mathbf{H} \tag{1.2.1.5b}$$

Equations (1.2.1.5) are known as constitutive relations since they supplement Maxwell's equations by giving the auxiliary field quantities in terms of the electromagnetic fields. A third constitutive relation, known as Ohm's law, is often used in the case of conducting materials. It relates the free current density to the electric field through

$$\mathbf{J}_f = \sigma \mathbf{E} \tag{1.2.1.6}$$

where σ is known as the material conductivity. In fact, σ is related to the electric permittivity function through the relation $\epsilon(\omega) = \epsilon_0 + i\frac{\sigma(\omega)}{\omega}$. Based on the above, it becomes readily apparent that the electrodynamics of matter is governed essentially by two parameters: the electric permittivity, ϵ, and the magnetic permeability, μ. In general these quantities are complex valued and frequency dependent such that $\epsilon \to \tilde{\epsilon}(\omega)$ and $\mu \to \tilde{\mu}(\omega)$.

Before proceeding, it is important to note that without appropriate boundary conditions Maxwell's equations, (1.2.1.2), do not provide a unique solution to a given problem. Generally, both the electromagnetic and auxiliary fields have discontinuous vector components at a material boundary. In the case of materials with free surface charge or current present, these boundary condi-

tions take the following form

$$\mathbf{E}_1^t - \mathbf{E}_2^t = 0 \tag{1.2.1.7a}$$

$$\mathbf{H}_1^t - \mathbf{H}_2^t = \mathbf{K}_f \times \hat{\mathbf{n}} \tag{1.2.1.7b}$$

$$D_1^n - D_2^n = \sigma_f \tag{1.2.1.7c}$$

$$B_1^n - B_2^n = 0 \tag{1.2.1.7d}$$

where σ_f is the free surface charge, $\mathbf{K}_f$ is the free surface current and $\hat{\mathbf{n}}$ is a unit vector normal to the interface. Also, the superscripts specify the field component (either tangential (t) or normal (n) to the boundary surface) and the subscripts represent the materials which make up the boundary. This means that the tangential electric field and normal magnetic flux density are continuous across the boundary, while the normal electric flux density and tangential magnetic field are discontinuous across the boundary by an amount equal to the free surface charge and free surface current, respectively.

At this stage it is relevant to discuss the transport of electromagnetic energy from one point to another through the travelling wave solutions of Maxwell's equations. As before, materials which are isotropic, homogeneous and linear with respect to the electromagnetic fields will be considered such that equations (1.2.1.5) apply. Under these assumptions, equations (1.2.1.2) can be decoupled by taking the curl of (1.2.1.2a) and (1.2.1.2c), and using the vector identity $\nabla \times (\nabla \times \mathbf{A}) = \nabla (\nabla \cdot \mathbf{A}) - \nabla^2 \mathbf{A}$

$$\nabla \times (\nabla \times \mathbf{E}) = \nabla \underbrace{\left(\cancel{\nabla \cdot \mathbf{E}}\right)}_{0} - \nabla^2 \mathbf{E} = -\tilde{\mu} \frac{\partial}{\partial \mathrm{t}} (\nabla \times \mathbf{H})$$

$$\nabla \times (\nabla \times \mathbf{H}) = \nabla \underbrace{\left(\cancel{\nabla \cdot \mathbf{H}}\right)}_{0} - \nabla^2 \mathbf{H} = \tilde{\epsilon} \frac{\partial}{\partial \mathrm{t}} (\nabla \times \mathbf{E})$$

where it is assumed that no free charge or current is present. Simplification yields

$$\nabla^2\mathbf{E} = \tilde{\mu}\tilde{\epsilon}\frac{\partial^2\mathbf{E}}{\partial \mathrm{t}^2}$$
$$\nabla^2\mathbf{H} = \tilde{\mu}\tilde{\epsilon}\frac{\partial^2\mathbf{H}}{\partial \mathrm{t}^2} \tag{1.2.1.8}$$

For simplicity, consider the case of time-harmonic[1], plane wave solutions to these equations taking the general form

$$\tilde{\mathbf{E}}(\mathbf{r},t) = \tilde{\mathbf{E}}_0 e^{i\left(\tilde{\mathbf{k}}\cdot\mathbf{r}-\omega t\right)}$$
$$\tilde{\mathbf{H}}(\mathbf{r},t) = \tilde{\mathbf{H}}_0 e^{i\left(\tilde{\mathbf{k}}\cdot\mathbf{r}-\omega t\right)} \tag{1.2.1.9}$$

where $\tilde{\mathbf{E}}_0 = \mathbf{E}_0 e^{i\phi}$ and $\tilde{\mathbf{H}}_0 = \mathbf{H}_0 e^{i\phi}$ are the complex wave amplitudes for the electric and magnetic fields, respectively, and ϕ represents the phase of the wavefront at time $t = 0$. The wave vector, $\tilde{\mathbf{k}} = \sqrt{\tilde{\mu}\tilde{\epsilon}}\omega\hat{\mathbf{n}} = \frac{\tilde{n}\omega}{c}\hat{\mathbf{n}}$, has been introduced to facilitate waves travelling in an arbitrary direction defined by $\hat{\mathbf{k}}\cdot\hat{\mathbf{r}}$. The index of refraction, $\tilde{n} = \sqrt{\frac{\tilde{\mu}\tilde{\epsilon}}{\mu_0\epsilon_0}}$, is used to describe the electromagnetic properties of the medium in which the waves are propagating, and $c = \frac{1}{\sqrt{\mu_0\epsilon_0}}$ represents the speed of an electromagnetic wave in freespace (the speed of light).

Although (1.2.1.9) are solutions to equations (1.2.1.8), they do not satisfy Maxwell's equations in their present form. It can be shown that Maxwell's equations impose constraints on $\tilde{\mathbf{E}}_0$ and $\tilde{\mathbf{H}}_0$. Taking the divergence of (1.2.1.9) and using equations (1.2.1.2b) and (1.2.1.2d) with no source terms it is found that

$$\tilde{E}_{0\left(\hat{\mathbf{k}}\cdot\hat{\mathbf{r}}\right)} = \tilde{H}_{0\left(\hat{\mathbf{k}}\cdot\hat{\mathbf{r}}\right)} = 0$$

[1]The assumption of harmonic time-dependence does not result in a loss of generality since an arbitrary time signal can be constructed through the principle of Fourier superposition

implying that the waves are *transverse* (i.e. there are no components of the electromagnetic fields along the direction of propagation). Furthermore, by substituting (1.2.1.9) into equation (1.2.1.2a) or (1.2.1.2c) it is found that

$$\tilde{\mathbf{H}}_0 = \frac{\tilde{n}}{c}\left(\hat{\mathbf{r}} \times \tilde{\mathbf{E}}_0\right)$$

implying that the electric and magnetic fields are in phase and mutually orthogonal. Under these constraints, the general solutions to the wave equations given by (1.2.1.9) can be rewritten such that they also satisfy Maxwell's equations

$$\begin{aligned} \tilde{\mathbf{E}}(\mathbf{r}, t) &= \tilde{E}_0 e^{i\left(\tilde{\mathbf{k}}\cdot\mathbf{r} - \omega t\right)}\hat{\mathbf{n}} \\ \tilde{\mathbf{H}}(\mathbf{r}, t) &= \frac{\tilde{n}}{c}\left(\hat{\mathbf{k}} \times \tilde{\mathbf{E}}\right) \end{aligned} \tag{1.2.1.10}$$

where $\hat{\mathbf{n}}$ is the polarization vector representing the oscillation direction of the electric field, $\tilde{\mathbf{E}}$. Note that the *physical* electric and magnetic fields are the real parts of equations (1.2.1.10).

1.2.2 Modelling the Permittivity of Linear Media

The majority of the problem in describing the interaction of electromagnetic fields with matter is in finding a suitable relationship between the macroscopic field quantities and the polarization and magnetization of the material. In general, this relationship can be rather complex; however, for the purposes of this thesis work materials that are isotropic, homogeneous and linear with respect to the macroscopic fields will be considered. Under these assumptions there exist intuitive classical models for material response to an electric field based on the damped harmonic motion of electric dipoles.

Consider the interaction between a harmonic electromagnetic wave of frequency ω and the bound electrons of an atom with a single resonance frequency at $\omega = \omega_0$. In this scenario, the incident electromagnetic wave causes the bound electrons to oscillate resulting in a time-varying displacement between the electrons and their binding nuclei. By making the assumption that this motion is akin to that of a damped harmonic oscillator, where damping is a result of collisional processes, the equation of motion for a single electron in this scenario is given by

$$m^* \frac{d^2\mathbf{r}}{d\mathrm{t}^2} + m^* \gamma_0 \frac{d\mathbf{r}}{d\mathrm{t}} + m^* \omega_0^2 \mathbf{r} = q_e \mathbf{E} \tag{1.2.2.1}$$

where m^* is the effective electron mass, γ_0 is the resonance damping rate and $q_e = -e$ is the elementary charge of the electron. This particular form of damped harmonic motion is known as the Lorentz oscillator model. The left-hand side of the equation represents the sum of the forces acting on the electron: acceleration ($F_a = m^*\mathbf{a}$), where $\mathbf{a}$ is the acceleration vector; damping ($F_d = m^*\gamma_0\mathbf{v}$), where $\mathbf{v}$ is the velocity vector; and restoration ($F_r = m^*\omega_0^2\mathbf{r}$), where $\mathbf{r}$ is the position vector. The right-hand side is the result of the driving force due to the presence of an electric field ($F_e = q_e\mathbf{E}$). As noted above, harmonic time-dependence is assumed such that the driving electric field takes the general, complex form

$$\tilde{\mathbf{E}}(t) = \tilde{\mathbf{E}}_0 e^{-i\omega t}$$

This provides solutions to the differential equation for the electron's displacement, which take the form

$$\tilde{\mathbf{r}}(t) = \tilde{\mathbf{R}}_0 e^{-i\omega t}$$

where $\tilde{\mathbf{R}}_0$ is the complex amplitude of the electron's oscillations. Substitution of these quantities into equation (1.2.2.1) gives the freqeuncy-dependent form

of the electron's oscillation amplitude

$$\tilde{\mathbf{R}}_0 = -\left(\frac{e}{m^*}\right)\left(\frac{1}{\omega_0^2 - \omega^2 - i\gamma_0\omega}\right)\tilde{\mathbf{E}}_0 \tag{1.2.2.2}$$

This displacement gives rise to a time-varying electric dipole moment given by $\tilde{\mathbf{p}}(t) = -e\tilde{\mathbf{r}}(t)$. Now, if N electrons per unit volume are present in the material, then the net dipole moment induced by a harmonic electric field results in a time-dependent macroscopic polarization of the form

$$\tilde{\mathbf{P}}(t) = N\tilde{\mathbf{p}}(t) = \left(\frac{Ne^2}{m^*}\right)\left(\frac{1}{\omega_0^2 - \omega^2 - i\gamma_0\omega}\right)\tilde{\mathbf{E}}(t) \tag{1.2.2.3}$$

where equation (1.2.2.2) has been used. In general, equation (1.2.2.3) can be extended to handle an arbitrary number of resonances at frequencies $\omega = \omega_j$ with characteristic damping γ_j, and strength f_j such that

$$\tilde{\mathbf{P}}(t) = \left(\frac{Ne^2}{m^*}\right)\sum_j \frac{f_j}{\omega_j^2 - \omega^2 - i\gamma_j\omega}\tilde{\mathbf{E}}(t) \tag{1.2.2.4}$$

Note that the strength of a resonance (f_j) is determined by the portion of N which takes part in that particular resonance, and $\sum_j f_j = 1$.

From the previous section it is known that for linear, isotropic, homogeneous materials the electric polarization takes the form $\mathbf{P} = \epsilon_0\chi_e\mathbf{E}$. Based on this fact the complex electric susceptibility of a material with an electric polarization given by (1.2.2.4) takes the following form

$$\tilde{\chi}_e = \left(\frac{Ne^2}{\epsilon_0 m^*}\right)\sum_j \frac{f_j}{\omega_j^2 - \omega^2 - i\gamma_j\omega}$$

from which the frequency-dependent electric permittivity can be deduced

$$\tilde{\epsilon}(\omega) = \epsilon_0 \left(1 + \sum_j \frac{f_j \omega_p^2}{\omega_j^2 - \omega^2 - i\gamma_j \omega}\right) \tag{1.2.2.5}$$

where the plasma frequency $\omega_p = \sqrt{\frac{Ne^2}{\epsilon_0 m^*}}$ has been introduced, which represents the natural oscillation frequency of the system of electrons.

With the most general form of the electric permittivity in hand it is pertinent to study one of its limiting cases. Equation (1.2.2.5) is based on the fact that the electrons in the material are bound, which is not always the case. The conduction electrons in a metal, for example, are essentially free such that they are not subjected to resonances as is the case for bound electrons. Therefore, by letting $\omega_j \to 0$ and removing the summation in equation (1.2.2.5), the frequency-dependent electric permittivity of a free electron gas is found to be

$$\tilde{\epsilon}(\omega) = \epsilon_0 \left(1 - \frac{f_0 \omega_p^2}{\omega^2 + i\gamma_0 \omega}\right) \tag{1.2.2.6}$$

This particular form of the electric permittivity is based on the free electron model of Drude, which was originally proposed to model the frequency-dependent conductivity of metals. In fact, the Drude model for conductivity is reproduced from equation (1.2.2.6) by using the relation $\tilde{\epsilon}(\omega) = \epsilon_0 + i\frac{\tilde{\sigma}(\omega)}{\omega}$, which connects the electric permittivity to the conductivity of a material as specified previously.

1.2.3 Surface Plasmons

Surface plasmons are collective excitations of a conductor's free electron gas. This phenomenon describes the coupling of electromagnetic waves to the surface of conducting media, which, in general, is represented as either a propagat-

ing or localized surface mode. The following subsections outline this interaction in terms of Maxwell's equations and the models of the electric permittivity function introduced in the previous section.

Propagating Modes

In the simplest case, a propagating surface plasmon mode, or surface plasmon polariton (SPP), arises when an electromagnetic wave is evanescently confined at the interface of a conductor (medium 1) and a dielectric (medium 2). Consider the two-dimensional geometry of Figure 1.2.3.1, where such a wave propagates in the z-direction along an interface located at $x = 0$. It is assumed

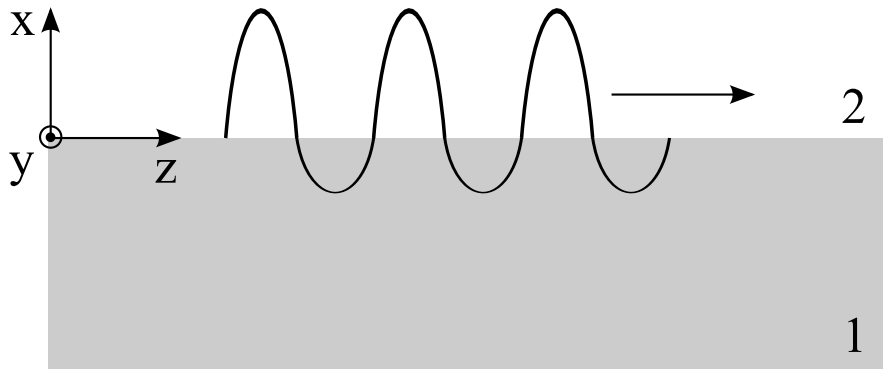

Figure 1.2.3.1: Example geometry for surface plasmon polariton propagation along a semi-infinite interface at $x = 0$. Medium 1 represents a conductor while medium 2 represents a dielectric.

here that the wave amplitude extends to infinity in the y-direction; therefore, it is dependent only on the x-direction. The plane wave solutions from before, equations (1.2.1.9), can be applied here by allowing the wave amplitude to depend on x. For propagation in the $+z$-direction this looks like

$$\tilde{\mathbf{E}}(\mathbf{r}, t) = \tilde{\mathbf{E}}(x)\, e^{i\left(\tilde{k}_z z - \omega t\right)}$$

$$\tilde{\mathbf{H}}(\mathbf{r}, t) = \tilde{\mathbf{H}}(x)\, e^{i\left(\tilde{k}_z z - \omega t\right)}$$

The Maxwell curl equations, (1.2.1.2a) and (1.2.1.2c), can then be used to find explicit expressions for the electromagnetic fields. Based on the given wave solutions it is apparent that $\frac{\partial}{\partial y} = 0$, $\frac{\partial}{\partial z} = i\tilde{k}_z$ and $\frac{\partial}{\partial t} = -i\omega$, which results in

$$-i\tilde{k}_z E_y = i\omega\tilde{\mu} H_x \tag{1.2.3.1a}$$

$$i\tilde{k}_z E_x - \frac{\partial E_z}{\partial x} = i\omega\tilde{\mu} H_y \tag{1.2.3.1b}$$

$$\frac{\partial E_y}{\partial x} = i\omega\tilde{\mu} H_z \tag{1.2.3.1c}$$

$$-i\tilde{k}_z H_y = -i\omega\tilde{\epsilon} E_x \tag{1.2.3.1d}$$

$$i\tilde{k}_z H_x - \frac{\partial H_z}{\partial x} = -i\omega\tilde{\epsilon} E_y \tag{1.2.3.1e}$$

$$\frac{\partial H_y}{\partial x} = -i\omega\tilde{\epsilon} E_z \tag{1.2.3.1f}$$

This system of equations sustains two separate solution sets depending on the polarization of the propagating surface mode. If there is no electric field component along the direction of propagation then the propagating mode is termed transverse electric (TE). On the other hand, if there is no magnetic field component along the direction of propagation then the mode is termed transverse magnetic (TM). The TE modes are governed by equations (1.2.3.1a), (1.2.3.1c) and (1.2.3.1e) such that

$$\begin{aligned} \frac{\partial^2 E_y}{\partial x^2} &= \left(\tilde{k}_z^2 - \tilde{k}^2\right) E_y \\ H_x &= -\left(\frac{\tilde{k}_z}{\omega\tilde{\mu}}\right) E_y \\ H_z &= -\left(\frac{i}{\omega\tilde{\mu}}\right) \frac{\partial E_y}{\partial x} \end{aligned} \tag{1.2.3.2}$$

while the TM modes are governed by equations (1.2.3.1b), (1.2.3.1d) and (1.2.3.1f) such that

$$\begin{aligned} \frac{\partial^2 H_y}{\partial x^2} &= \left(\tilde{k}_z^2 - \tilde{k}^2\right) H_y \\ E_x &= \left(\frac{\tilde{k}_z}{\omega\tilde{\epsilon}}\right) H_y \\ E_z &= \left(\frac{i}{\omega\tilde{\epsilon}}\right) \frac{\partial H_y}{\partial x} \end{aligned} \tag{1.2.3.3}$$

where the wavevector $\tilde{k} = \sqrt{\tilde{\mu}\tilde{\epsilon}}\omega$ has been introduced in the simplification.

With the functional dependance of the electromagnetic fields in the given geometry (Figure 1.2.3.1) determined, it is possible to find a relationship for the wavevector of the SPP, $\tilde{k}_z$, in terms of the electromagnetic properties of medium 1 and 2 (i.e. $\tilde{\epsilon}$ and $\tilde{\mu}$). As mentioned above, SPP waves are evanescently confined to the material interface at $x = 0$; therefore, confined wave solutions will be sought. Consider first a TM mode SPP. Following from equations (1.2.3.3), the fields for $x > 0$ (medium 2) take the form

$$H_y(x) = A_2 e^{-\tilde{\beta}_2 x} e^{i\tilde{k}_z z} \tag{1.2.3.4a}$$

$$E_x(x) = A_2 \left(\frac{\tilde{k}_z}{\omega\tilde{\epsilon}_2}\right) e^{-\tilde{\beta}_2 x} e^{i\tilde{k}_z z} \tag{1.2.3.4b}$$

$$E_z(x) = -iA_2 \left(\frac{\tilde{\beta}_2}{\omega\tilde{\epsilon}_2}\right) e^{-\tilde{\beta}_2 x} e^{i\tilde{k}_z z} \tag{1.2.3.4c}$$

and the fields for $x < 0$ (medium 1) take the form

$$H_y(x) = A_1 e^{\tilde{\beta}_1 x} e^{i\tilde{k}_z z} \tag{1.2.3.5a}$$

$$E_x(x) = A_1 \left(\frac{\tilde{k}_z}{\omega \tilde{\epsilon}_1} \right) e^{\tilde{\beta}_1 x} e^{i\tilde{k}_z z} \tag{1.2.3.5b}$$

$$E_z(x) = iA_1 \left(\frac{\tilde{\beta}_1}{\omega \tilde{\epsilon}_1} \right) e^{\tilde{\beta}_1 x} e^{i\tilde{k}_z z} \tag{1.2.3.5c}$$

where equations (1.2.3.4a) and (1.2.3.5a) are solutions to the TM mode wave equation given by (1.2.3.3) such that

$$\begin{aligned} \tilde{\beta}_1^2 &= \tilde{k}_z^2 - \tilde{k}_1^2 \\ \tilde{\beta}_2^2 &= \tilde{k}_z^2 - \tilde{k}_2^2 \end{aligned} \tag{1.2.3.6}$$

To proceed from here the solutions in the two half spaces must be matched at the interface $x = 0$. Continuity of H_y at $x = 0$ demands that the amplitudes be equal, or $A_1 = A_2$, while matching E_z at $x = 0$ gives

$$\frac{\tilde{\beta}_1}{\tilde{\beta}_2} = -\frac{\tilde{\epsilon}_1}{\tilde{\epsilon}_2} \tag{1.2.3.7}$$

Since $Re\left[\tilde{\beta}_1\right], Re\left[\tilde{\beta}_2\right] > 0$ for confined waves, equation (1.2.3.7) imposes a constraint on the electric permittivity of the two mediums: $Re\left[\tilde{\epsilon}_1\right]$ and $Re\left[\tilde{\epsilon}_2\right]$ must be of opposite sign. This is precisely the case for an interface between a conductor ($Re\left[\tilde{\epsilon}_1\right] < 0$) and a dielectric ($Re\left[\tilde{\epsilon}_2\right] > 0$). Finally, by combining (1.2.3.6) and (1.2.3.7) the dispersion relation for a TM mode SPP is realized

$$\tilde{k}_z = \frac{\omega}{c} \sqrt{\tilde{\epsilon}_1 \tilde{\epsilon}_2} \sqrt{\frac{\tilde{\epsilon}_1 \tilde{\mu}_2 - \tilde{\epsilon}_2 \tilde{\mu}_1}{\tilde{\epsilon}_1^2 - \tilde{\epsilon}_2^2}} \tag{1.2.3.8}$$

where the relation $\tilde{k} = \sqrt{\tilde{\mu}\tilde{\epsilon}}\omega$ has been used in the simplification. The importance of the dispersion relation lies in the fact that it contains all the information regarding the propagation of a given wave mode. This will be discussed in more detail, but first consider a TE mode SPP.

An analogous procedure to that used in finding the dispersion relation for a TM mode SPP can be applied in the TE case using equations (1.2.3.2). Once again, the SPP is a solution to the TE mode wave equation such that equation (1.2.3.6) still applies. Continuity of E_y at $x = 0$ gives $A_1 = A_2$, while matching H_z at $x = 0$ gives

$$\frac{\tilde{\beta}_1}{\tilde{\beta}_2} = -\frac{\tilde{\mu}_1}{\tilde{\mu}_2} \tag{1.2.3.9}$$

Similar to the TM case, $Re\left[\tilde{\beta}_1\right], Re\left[\tilde{\beta}_2\right] > 0$ for confined waves meaning that the real part of the permeabilities of the two mediums, $Re\left[\tilde{\mu}_1\right]$ and $Re\left[\tilde{\mu}_2\right]$, must be of opposite sign. Following an analogous procedure to the TM case, the dispersion relation for a TE mode SPP is given by

$$\tilde{k}_z = \frac{\omega}{c}\sqrt{\tilde{\mu}_1\tilde{\mu}_2}\sqrt{\frac{\tilde{\mu}_1\tilde{\epsilon}_2 - \tilde{\mu}_2\tilde{\epsilon}_1}{\tilde{\mu}_1^2 - \tilde{\mu}_2^2}} \tag{1.2.3.10}$$

It should be noted that most naturally occurring materials have $Re\left[\tilde{\mu}\right] > 0$ such that a TE mode SPP does not always exist. However, TE mode SPPs have been demonstrated with both antiferromagnetic materials [22] and plasmonic metamaterials [23].

Figure 1.2.3.2 (a) and (b) plots the real and imaginary parts of equation (1.2.3.8) for an SPP mode at the interface between gold ($\tilde{\mu}_1 = \mu_0$) and lossless silicon ($\tilde{\epsilon}_2 = 11.7\epsilon_0, \tilde{\mu}_2 = \mu_0$). The permittivity of gold can be well approximated by a combination of the Drude and Lorentz models with parameters taken from [24]. Figure 1.2.3.2 (a) and (b) has two regions of interest corresponding to $\omega < \omega_{SP}$ and $\omega > \omega_{SP}$, where ω_{SP} is the surface plasmon

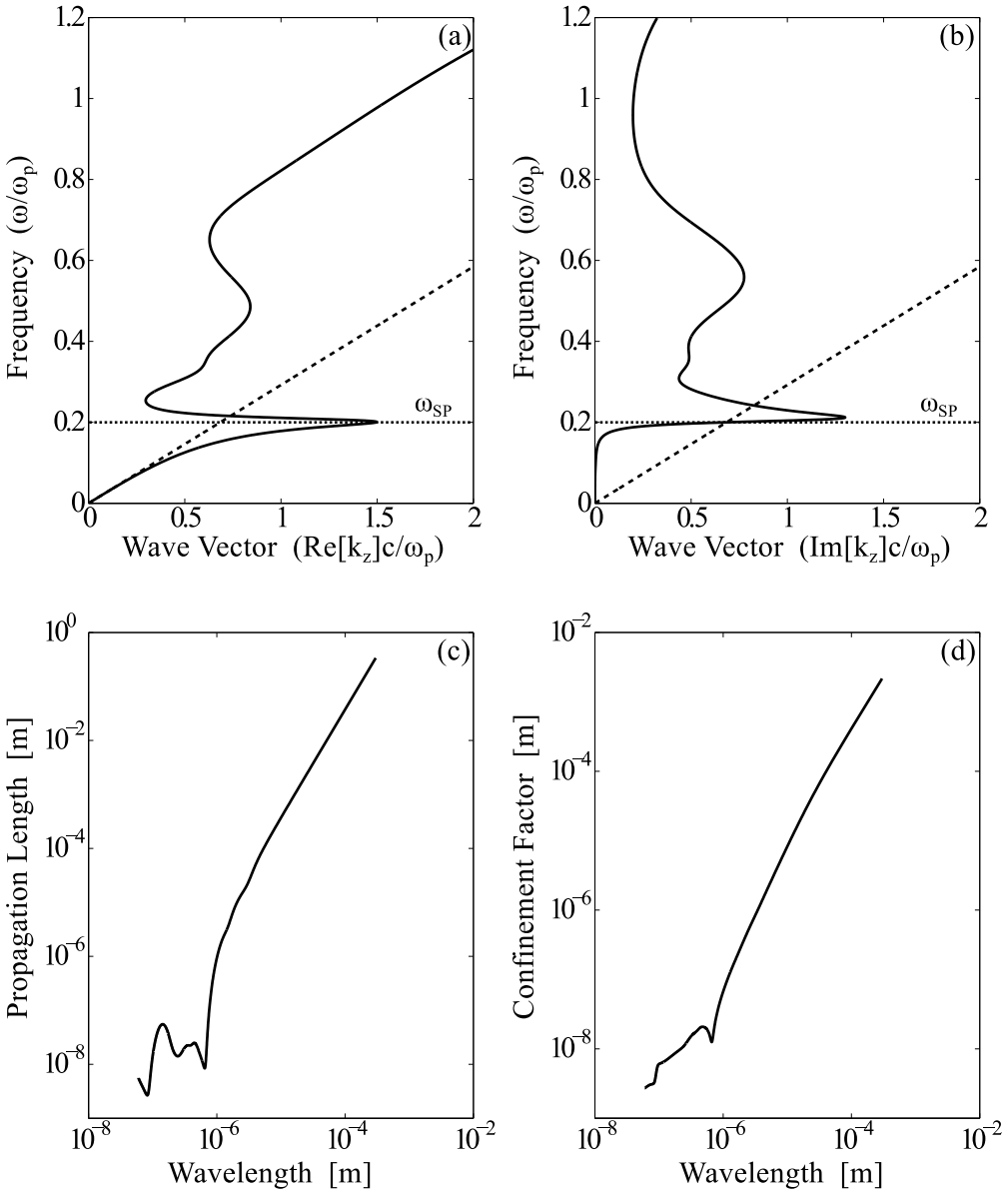

Figure 1.2.3.2: Real (a) and imaginary (b) parts of the dispersion relation for a TM mode SPP at a gold/silicon interface (solid). The light line for silicon (dashed) shows the frequency-wave vector relationship for a wave propagating in bulk, lossless silicon. The SPP propagation length and confinement factor in the dielectric are plotted in (c) and (d), respectively.

frequency. In the first regime, the mode is bound to the interface with a characteristic energy attenuation length and confinement factor along the x direction given by $L = \left(2Im\left[\tilde{k}_z\right]\right)^{-1}$ and $\alpha_i = 1/|\beta_i|$, respectively, where the subscript $i = 1, 2$ corresponds to either the metal or dielectric layer as specified above. These quantities are plotted in Figure 1.2.3.2 (c) and (d). At visible wavelengths, say $\lambda = 500$ nm, the mode is highly confined with $\alpha_2 \approx 20$ nm, but propagates only a short distance given by $L \approx 20$ nm. On the other hand, at THz frequencies, say $\lambda = 300$ µm, the mode is loosely bound with $\alpha_2 \approx 2$ mm, but propagates a long distance given by $L \approx 330$ mm. Therefore, SPP characteristics can be seen to vary greatly depending on the wavelength of the incident light. In the second regime, where $\omega > \omega_{SP}$, the mode is quasibound, or leaky, and is no longer confined to the interface.

One other piece of information that the dispersion relation provides is related to the actual excitation of SPP modes. Looking at Figure 1.2.3.2 (a) it is apparent that for $\omega < \omega_{SP}$ the SPP mode never intersects with the light line for silicon. This means that a wave propagating in the bulk dielectric material cannot directly excite a SPP mode at the interface with a conductor since momentum is not conserved (i.e. the wave incident on the conductor must gain momentum for this excitation to occur). To overcome this constraint common coupling schemes for SPPs have been developed, the simplest of which include prism and grating coupling. The prism coupling scheme makes use of a three-layer system where a thin conducting film is sandwiched between two dielectric materials having different permittivities. An electromagnetic wave travelling in the higher index dielectric attains sufficient momentum upon reflection from the thin conducting film to excite a SPP mode at the interface between the conducting film and the lower index dielectric. The higher index dielectric is typically a prism, hence the name of the coupling scheme. Depicted in Fig-

ure 1.2.3.3 are two popular geometries for this scheme, which are known as the Kretschmann [25] and Otto [26] configurations. On the other hand, the

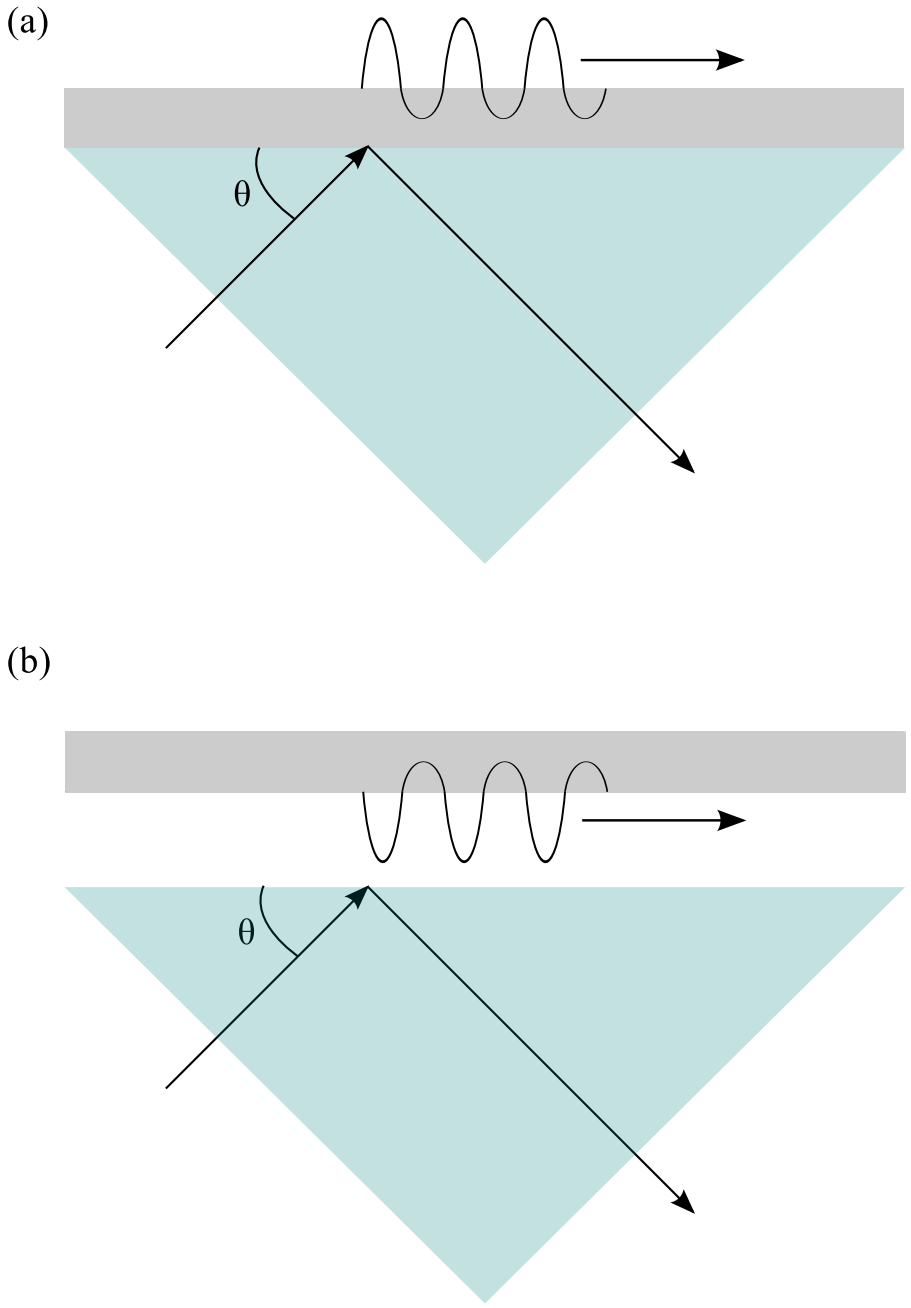

Figure 1.2.3.3: The Kretschmann (a) and Otto (b) prism coupling schemes for SPP excitation. The electromagnetic fields tunnel from a higher index dielectric (prism) to the interface between a thin conducting film and a lower index dielectric. The electromagnetic wave is incident at an angle θ.

grating coupling scheme makes use of a periodic grating patterned onto the

conducting surface to provide sufficient momentum for SPP excitation. Here, excitation will occur whenever $\tilde{k}_z = \tilde{k}\sin\theta \pm \frac{2\pi m}{a}$ where θ is the angle of incidence, a is the grating period and m is a real positive integer. This can be extended to a two-dimensional grating, which results in the following relation

$$\tilde{k}_z = \tilde{k}\sin\theta \pm \frac{2\pi m}{a} \pm \frac{2\pi n}{b} \tag{1.2.3.11}$$

where b is the grating period of the second dimension and n is a real positive integer.

Localized Modes

Unlike SPP modes, localized plasmon modes, or particle plasmons, are non-propagating and they arise through the scattering of electromagnetic waves from a subwavelength conductor. The simplest geometry to consider is that of a time-harmonic electromagnetic field interacting with a subwavelength spherical particle of diameter d. In the regime that $d << \lambda$ (i.e. subwavelength), this problem can be solved under the quasi-static approximation where the time-harmonic electromagnetic field is approximated as being both static and uniform over the volume occupied by the particle[2]. This approximation can be made in this case since the phase of the harmonic electromagnetic field is essentially uniform across the diameter of the particle meaning that spatial retardation effects can be neglected [17]. The geometry under investigation here is depicted in Figure 1.2.3.4, where a homogeneous sphere of radius a and electric permittivity $\tilde{\epsilon}_1$ is immersed in a uniform, static electric field given by $\mathbf{E} = E_0\hat{\mathbf{z}}$. The surrounding medium is a dielectric described by $\tilde{\epsilon}_2$.

Under the quasi-static approximation, a solution to the scattering problem depicted in Figure 1.2.3.4 is found through Laplace's equation for the electric

[2]In the electrostatic treatment that follows, harmonic time dependence of the fields can be included by multiplying the results by a factor of $e^{-i\omega t}$

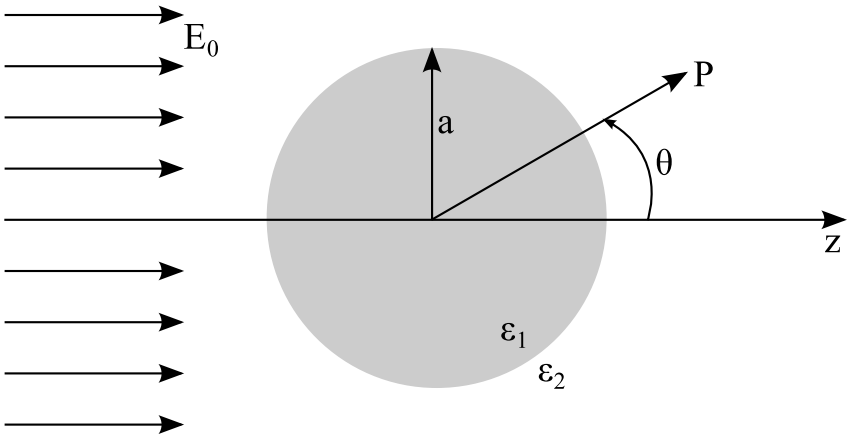

Figure 1.2.3.4: Geometry for the scattering problem of a homogeneous sphere of radius a in a static, uniform electric field. The vector P represents a position vector to an arbitrary point in space.

potential given by $\nabla^2\Phi = 0$[3]. Given the spherical symmetry of the problem, spherical coordinates offer the most intuitive approach to finding an analytical solution for Φ. As shown by Jackson [16], the solution to Laplace's equation inside and outside the sphere take the following form

$$\Phi_{in}(r,\theta) = \sum_{l=0}^{\infty} A_l r^l P_l(\cos\theta) \tag{1.2.3.12a}$$

$$\Phi_{out}(r,\theta) = \sum_{l=0}^{\infty} \left(B_l r^l + C_l r^{-(l+1)}\right) P_l(\cos\theta) \tag{1.2.3.12b}$$

where $P_l(\cos\theta)$ represent the Legendre polynomials of order l, and θ is as defined in Figure 1.2.3.4. Equations (1.2.3.12) are made unique through the application of appropriate boundary conditions, which place constraints on the coefficients A_l, B_l and C_l.

The first of these conditions is applied as $r \to \infty$ where it is required that $\Phi_{out} \to -E_0 r\cos\theta$. This results in

$$\begin{aligned}\Phi_{out}(r\to\infty,\theta) &= -E_0 r\cos\theta \\ &= \sum_{l=0}^{\infty} B_l r^l P_l(\cos\theta) \\ &= B_0 + B_1 r\cos\theta + \sum_{l=2}^{\infty} B_l r^l P_l(\cos\theta)\end{aligned}$$

which holds only when $B_1 = -E_0$ and $B_l = 0$ for all $l \neq 1$. The remaining boundary conditions are applied at $r = a$ where equation (1.2.3.12a) and (1.2.3.12b) must be matched. The tangential electric field is continuous across the boundary giving

$$\left.\frac{\partial\Phi_{in}}{\partial\theta}\right|_{r=a} = \left.\frac{\partial\Phi_{out}}{\partial\theta}\right|_{r=a}$$

[3]The electric field can be found from the electric potential using the relation $\mathbf{E} = -\nabla\Phi$

Assuming no free surface charge is present, the normal component of the electric flux density is also continuous across the boundary giving

$$\tilde{\epsilon}_1 \left.\frac{\partial \Phi_{in}}{\partial r}\right|_{r=a} = \tilde{\epsilon}_2 \left.\frac{\partial \Phi_{out}}{\partial r}\right|_{r=a}$$

In solving these two relations self-consistently it is found that $A_l = C_l = 0$ for all $l \neq 1$ leaving only A_1 and C_1 to be non-zero [16]. The resultant potentials inside and outside the sphere are then given by

$$\Phi_{in}(r,\theta) = -\left(\frac{3\tilde{\epsilon}_2}{\tilde{\epsilon}_1 + 2\tilde{\epsilon}_2}\right) E_0 r \cos\theta \tag{1.2.3.13a}$$

$$\Phi_{out}(r,\theta) = -E_0 r\cos\theta + \left(\frac{\tilde{\epsilon}_1 - \tilde{\epsilon}_2}{\tilde{\epsilon}_1 + 2\tilde{\epsilon}_2}\right)\left(\frac{a^3}{r^2}\right) E_0 \cos\theta \tag{1.2.3.13b}$$

from which the electric field distribution can be calculated

$$\mathbf{E}_{in} = \left(\frac{3\tilde{\epsilon}_2}{\tilde{\epsilon}_1 + 2\tilde{\epsilon}_2}\right) E_0 \hat{\mathbf{z}} \tag{1.2.3.14a}$$

$$\mathbf{E}_{out} = E_0\hat{\mathbf{z}} + \left(\frac{\tilde{\epsilon}_1 - \tilde{\epsilon}_2}{\tilde{\epsilon}_1 + 2\tilde{\epsilon}_2}\right)\left(\frac{a^3}{r^3}\right) E_0 \left(2\cos\theta\hat{\mathbf{r}} + \sin\theta\hat{\boldsymbol{\theta}}\right) \tag{1.2.3.14b}$$

The electric field induced inside the sphere is constant and parallel to the direction of the applied field. Interestingly, outside the sphere the electric field is equivalent to the applied field plus that caused by an induced electric dipole with a dipole moment along the direction of applied field given by

$$\mathbf{p} = 4\pi\tilde{\epsilon}_2 \left(\frac{\tilde{\epsilon}_1 - \tilde{\epsilon}_2}{\tilde{\epsilon}_1 + 2\tilde{\epsilon}_2}\right) a^3 E_0 \hat{\mathbf{z}} \tag{1.2.3.15}$$

Therefore, the solution to the given scattering problem is a superposition of the applied field and those fields resulting from an induced dipole moment. This purely electrostatic result can be extended to the scenario of a time-harmonic applied electric field by including a factor of $e^{-i\omega t}$. Under these circumstances

equation (1.2.3.15) will represent an oscillating dipole moment leading to radiation of electromagnetic energy.

To further elucidate the importance of the solution represented by equations (1.2.3.14), the magnitude and phase of the induced dipole moment is plotted in Figure 1.2.3.5. The sphere is assumed to be made of copper with a

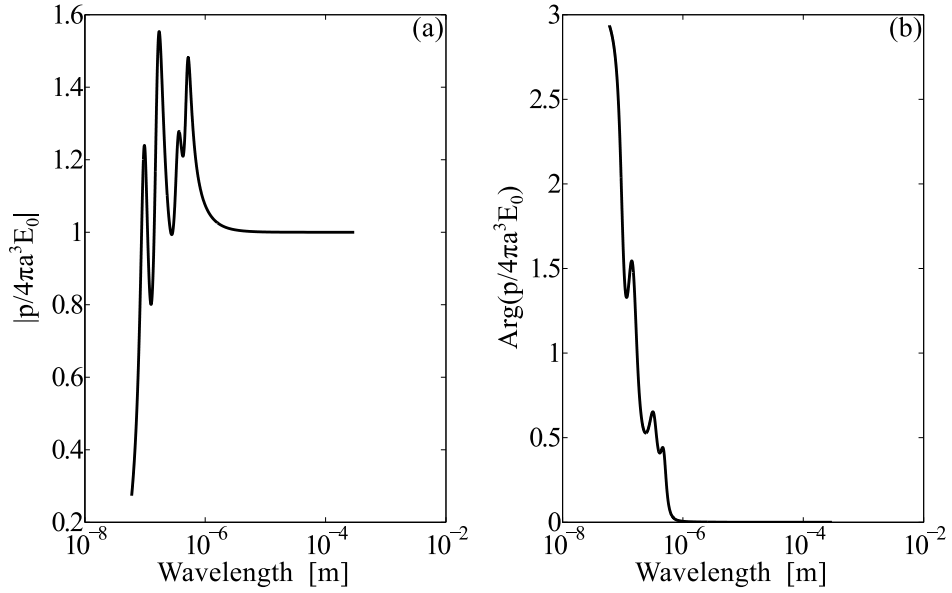

Figure 1.2.3.5: Magnitude (a) and phase (b) of the normalized induced dipole moment for a copper sphere immersed in a static, uniform electric field. The multiple resonances correspond to different state transitions of the conductor's free electron gas.

permittivity described by a Drude-Lorentz model with parameters taken from [24]. Also, the host medium is taken as air such that $\tilde{\epsilon}_2 = \epsilon_0$. A series of resonance phenomena arise as evidenced by the sharp increases in magnitude and phase flipping of the induced dipole moment. This in turn causes a resonant enhancement of the fields found in equation (1.2.3.14). It is these resonances that represent the phenomenon of localized surface plasmon modes. Interestingly, at longer wavelengths (i.e. THz regime) the induced dipole moment approaches a constant, non-zero value such that a dipolar response is still observed in this regime, albeit a non-resonant one.

1.2.4 Ferromagnetic Metals and Magnetoresistance

Thus far the theoretical background has mainly focused on electromagnetic theory where wave phenomena, material response and surface plasmons have been discussed. With these topics in hand it is now important to focus on some of the results from the field of solid state physics, particularly those dealing with the magnetism of ferromagnetic materials. As will be shown, ferromagnetic materials exhibit some interesting characteristics, such as spontaneous magnetization, hysteresis and magnetoresistivity.

For an individual atom, the presence of a magnetic moment is dictated by the interactions between the orbital and spin angular momenta of the bound electrons. Thus, the net magnetic moment of a group of atoms (i.e. a solid) will depend on how the individual atomic magnetic moments interact with one another through orbital-orbital, spin-spin and spin-orbital interactions of the electrons. It is these interactions that give rise to the magnetic properties of the solid and dictate whether it is diamagnetic, paramagnetic, ferromagnetic, ferrimagnetic or antiferromagnetic. Of particular interest in the category of magnetic solids are the ferromagnetic transition metals Fe, Ni and Co, whose properties will be the focus of this section's discussion.

It is easiest to utilize a band structure approach when discussing the magnetic ordering of the transition metal elements since it provides a straightforward picture, which explains, for example, why Ni is ferromagnetic and Cu is non-magnetic. These materials have their Fermi energy in a domain of overlapping 4s and 3d bands as indicated by Figure 1.2.4.1. States below the Fermi level are occupied while states above are vacant. Here, the density of states for spin-up and spin-down electrons in each band is shown along with the corresponding Fermi levels for Ni and Cu. Notice that the 3d sub band for spin-up electrons is shifted to lower energies than that of the the spin-down

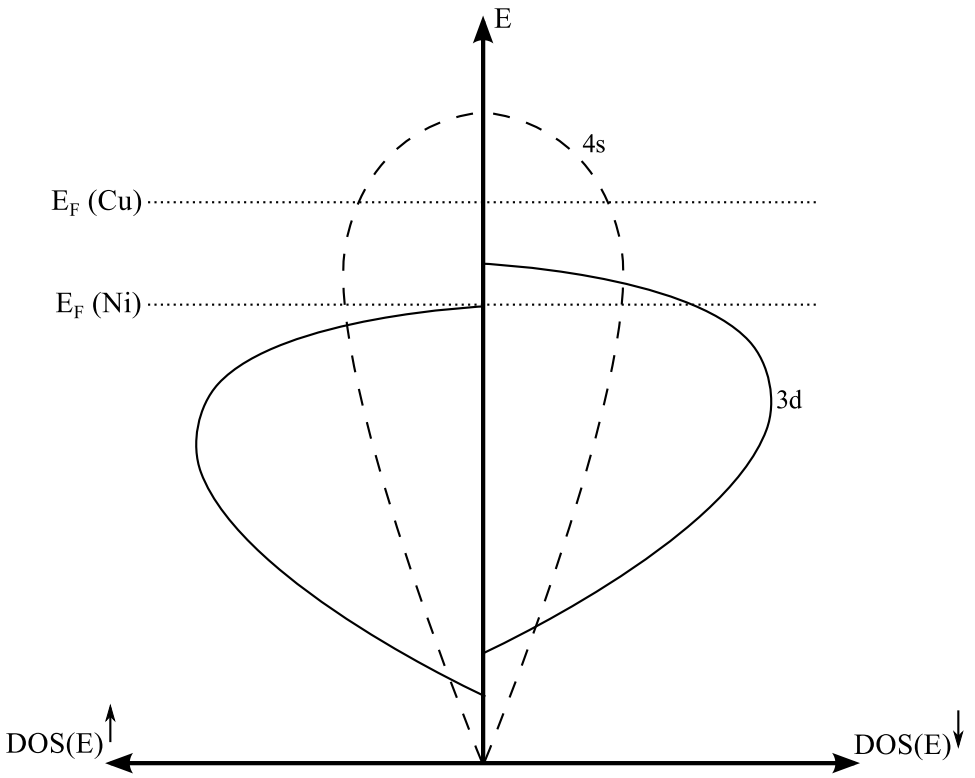

Figure 1.2.4.1: Theoretical band structure for a transition metal element showing the 4s and 3d spin-up and spin-down density of states.

sub band. This constant offset arises due to the exchange interaction[4], which plays a crucial role in determining the magnetic ordering of the solid. In this situation the exchange interaction places a certain constraint on a portion of the 3d electrons close to the Fermi level, requiring their spins to either be parallel or antiparallel to help minimize the total energy of the system. In the case of Ni, it is energetically favorable for these spins, and hence their magnetic moments, to be parallel resulting in ferromagnetic ordering and a spontaneous magnetization in the absence of an applied field. Therefore, as indicated by Figure 1.2.4.1, at the Fermi level Ni has a net spin polarization

[4]For ferromagnetic or antiferromagnetic materials, the quantum mechanical exchange interaction arises when neighbouring atoms are close enough together such that the wave functions of the electrons giving rise to their magnetic moments overlap. The result is a strong, but short range coupling of the magnetic moments which decreases as the atoms are moved farther apart. Depending on their separation distance, the exchange interaction causes the adjacent magnetic moments to be parallel (i.e. ferromagnetism) or antiparallel (i.e. antiferromagnetism)

with more 3d states occupied by spin-up electrons than spin-down electrons. On the other hand, Cu possesses a completely full 3d band and experiences no spin polarization since the exchange splitting of the 4s band is negligible; therefore, Cu is non-magnetic.

Before proceeding any further it is important to mention the situation when the exchange interaction forces the spins of the 3d electrons near the Fermi level to be antiparallel. This results in what is known as antiferromagnetic ordering of the solid. In this scenario, the magnetic moments of adjacent atoms are antiparallel and no net spontaneous magnetization of the material occurs. In addition, antiferromagnets exhibit a paramagnet-like magnetization curve where the magnetization of the solid is linear in the applied magnetic field. This is contrary to a ferromagnetic solid, which exhibits a phenomenon know as magnetic hysteresis, which leads to a much more interesting magnetization curve as will be discussed shortly.

Although the exchange interaction in the ferromagnetic transition metals promotes alignment of atomic magnetic moments and hence a spontaneous magnetization, these materials do not possess a net magnetization in their demagnetized state. Instead, the material is made up of a series of individual domains with magnetic moments that average to zero. The application of a strong magnetic field causes these magnetic moments to align parallel to the applied field effectively creating a single magnetic domain. This process is illustrated in Figure 1.2.4.2.

Due to the presence of magnetic domains it is clear that as the strength of the applied magnetic field increases from zero to some large value the magnetization of a ferromagnetic material will follow a similar trend. Once a large enough field is applied to create a single magnetic domain it is expected that the magnetization of the material will saturate and remain constant for any

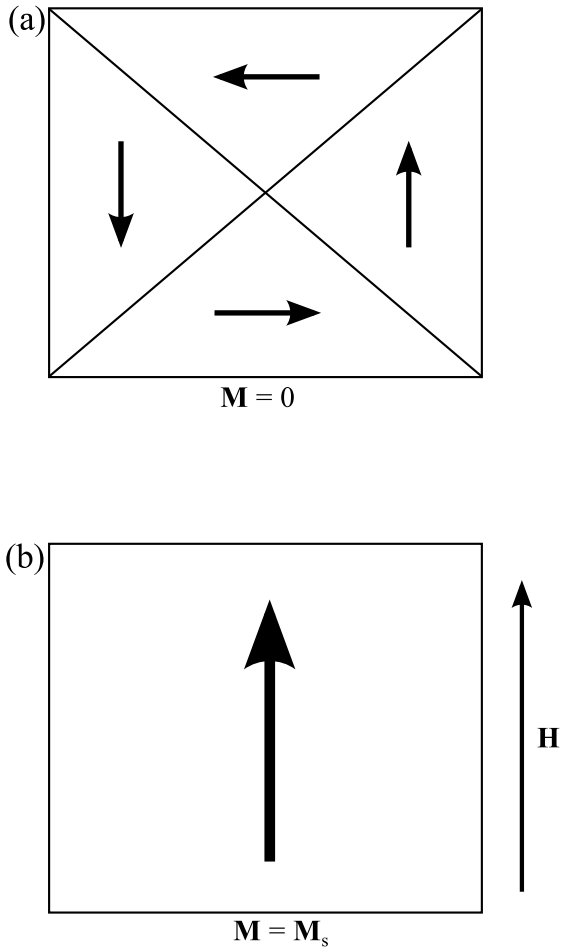

Figure 1.2.4.2: (a) A ferromagnetic material in its demagnetized state is made up of a series of domains. The net magnetization is zero. (b) The application of a strong magnetic field removes the domain walls and saturates the material.

further increase in the applied field. The interesting fact about ferromagnetic materials is that they maintain a net magnetization even after the applied field has been completely removed. A hypothetical magnetization curve for a ferromagnetic material is shown in Figure 1.2.4.3. The path from point A to C represents the initial magnetization of the material to saturation from a demagnetized state. The magnetization at point C is known as the saturation magnetization and is denoted by $\mathbf{M}_s$. As the applied field is reduced back to zero the path from point C to D is followed. At point D the material possesses a remanent magnetization denoted by $\mathbf{M}_r$, which is less than $\mathbf{M}_s$. The

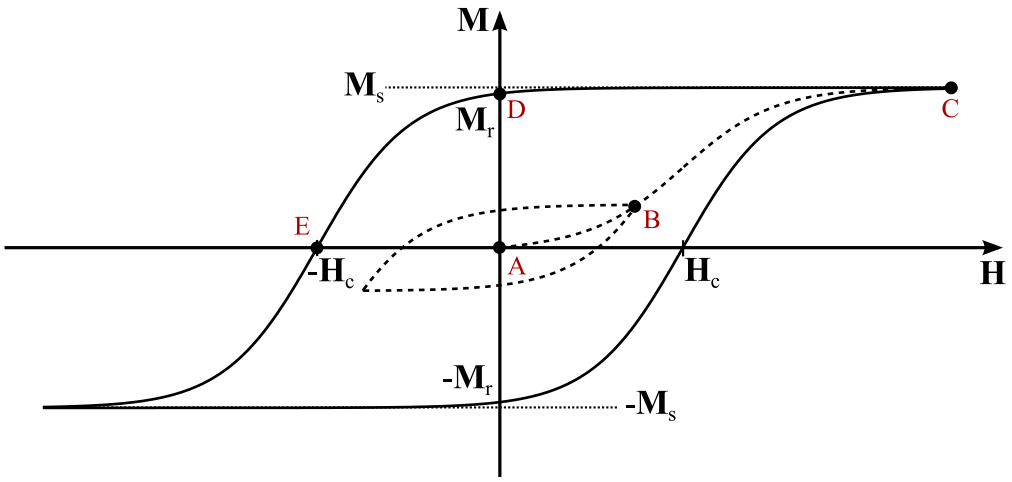

Figure 1.2.4.3: Hypothetical hysteresis loop for a ferromagnetic material. The solid loop represents the major, or limiting, hysteresis loop while the dashed loop represents a minor hysteresis loop. Initial magnetization is represented by the dashed path from point A to C.

application of a magnetic field in the opposite direction eventually decreases the magnetization of the sample back to zero at point E. The magnetic field strength required to achieve this is known as the coercive field strength and is denoted by $\mathbf{H}_c$. Further increase of the applied field in this direction will once again saturate the material. Cycling of the applied field between the saturation points of the material traces out the so-called *major* hysteresis loop. A *minor* hysteresis loop occurs when the material does not reach saturation upon initial magnetization of the sample. This is represented by the dashed path from point A to B and subsequent cycling of the applied field traces out the dashed loop.

Although it seems peculiar that a ferromagnetic material retains some of its magnetization after the applied magnetic field is removed, it can be understood using the domain theory of ferromagnetism. As mentioned above, a ferromagnetic material consists of a series of magnetized domains which average to zero in its demagnetized state. The application of a magnetic field causes the domain walls to move in such a way as to favor the growth of do-

mains with magnetic moments oriented along the direction of the applied field. As the domains grow, the walls encounter crystal imperfections which tend to pin the domain walls until sufficient energy is provided such that their motion can continue. Increasing the applied magnetic field will eventually eliminate all domain walls resulting in a single domain with its magnetic moment pointing along the direction of the applied field. This is where the magnetization of the material saturates. Once the applied field is removed, the demagnetizing field of the material promotes the growth of new domains to minimize the magnetostatic energy of the material. However, the demagnetizing field is not strong enough to completely remove the magnetization of the material since domain walls will again get pinned by crystal imperfections. This effect is the cause of the observed hysteresis, and the result is a finite magnetization in the material after the applied field is removed.

As a final note on ferromagnetism, it is important to note that the ferromagnetic ordering caused by the exchange interaction is constantly contested by the randomizing effects of thermal energy. These effects work to eliminate the spontaneous magnetization by randomizing the magnetic moments of the material. In fact, above a certain temperature the thermal energy of the electrons dominates over the exchange interaction effectively destroying the ferromagnetic ordering such that the material behaves paramagnetically. This temperature is known as the Curie temperature. A similar effect is exhibited by antiferromagnets where the antiferromagnetic ordering exists only below a certain temperature known as the Néel temperature.

Among all the interesting phenomena associated with magnetism, the magnetic field dependent resistivity (magnetoresistance) of metallic materials has found important technological applications. The final portion of this section will be devoted to consideration of a variety of magnetoresistance phenom-

ena, which come in a number of different "flavors" depending on the material configuration under study. To begin with, the simplest case of ordinary magnetoresistance will be discussed.

Resistance to current flow in a metal is a result of conduction electrons experiencing scattering events as they move through the lattice. In the absence of an applied magnetic field the electron trajectories follow straight line paths between these scattering events. However, under the influence of an applied magnetic field the conduction electrons are subject to the Lorentz force, which is given by $\mathbf{F}_L = -e\,(\mathbf{v} \times \mathbf{B})$ where $\mathbf{v}$ is the electron velocity and $\mathbf{B}$ is the applied magnetic field. The result of this force is to cause the electrons to follow helical trajectories between scattering events causing them to travel farther and scatter more frequently. Therefore, in the presence of an applied magnetic field, the resistivity of a metal increases by a small amount ($< 1\%$) [27]. The total resistivity of a metal under the influence of a magnetic field thus has a form given by $\rho\,(\mathbf{B}, \theta) = \rho_0 + \rho_{Lorentz}\,(\mathbf{B}, \theta)$ where ρ_0 is the resistivity of the metal in the absence of an applied magnetic field (i.e. background resistivity), $\rho_{Lorentz}$ is the contribution to the resistivity as result of the Lorentz force and θ is the angle between the applied field and current flow. The background resistivity arises due to conduction electrons scattering from crystal impurities and defects as well as thermal phonons.

In ferromagnetic metals there exists another form of magnetoresistance known as anisotropic magnetoresistance (AMR). For these types of metals, when a magnetic field is applied parallel (perpendicular) to the direction of current flow the resistance typically increases (decreases). The physical origin of the AMR effect in ferromagnetic metals lies in the coupling of the orbital and spin angular momenta of the 3d electrons. Essentially, as the magnetization direction of the material rotates, the spin-orbit coupling causes the 3d electron

cloud to deform slightly either increasing or decreasing the effective scattering cross section experienced by conduction electrons moving through the lattice. If the magnetization lies along the direction of current flow then the conduction electrons are scattered more and the resistivity increases. On the other hand, if the magnetization is perpendicular to the current flow then the conduction electrons scatter less and the resistivity decreases. This effect is depicted in Figure 1.2.4.4. As shown by Van Elst [28] and McGuire and Potter [29], AMR typically results in a room temperature resistivity change on the order of a few percent for ferromagnetic metals and their alloys. The total resistivity of a ferromagnetic metal is thus given by $\rho(\mathbf{B},\theta) = \rho_0 + \rho_{Lorentz}(\mathbf{B},\theta) + \rho_{AMR}(\mathbf{B},\theta)$, where $\rho_{AMR}(\mathbf{B},\theta)$ can be written as [29]

$$\begin{aligned}\rho_{AMR}(\mathbf{B},\theta) &= \rho_{\perp}(\mathbf{B})\sin^2\theta + \rho_{\parallel}(\mathbf{B})\cos^2\theta \\ &= \rho_{\perp}(\mathbf{B}) + \left[\rho_{\parallel}(\mathbf{B}) - \rho_{\perp}(\mathbf{B})\right]\cos^2\theta \\ &= \rho_{\perp}(\mathbf{B}) + \Delta\rho(\mathbf{B})\cos^2\theta \qquad (1.2.4.1)\end{aligned}$$

where $\rho_{\perp}(\mathbf{B})$ and $\rho_{\parallel}(\mathbf{B})$ are the resistivities of the metal when the magnetization is perpendicular and parallel to the current flow, respectively.

The final, most technologically useful form of magnetoresistance that will be presented here is known as giant magnetoresistance (GMR). GMR is an effect that occurs in thin-film metallic multilayers consisting of non-magnetic spacer layers sandwiched between ferromagnetic layers. This magnetoresistance effect typically shows resistivity changes of $\sim 10\%$ or greater at room temperature and can be engineered to do so with very small applied magnetic fields. There are essentially three different configurations of the metallic multilayers that lead to the GMR effect; they are known as the spin-valve [30], pseudo-spin-valve [31] and exchange coupled [32, 33] configurations. The easiest way to understand the basic functionality of these configurations is graph-

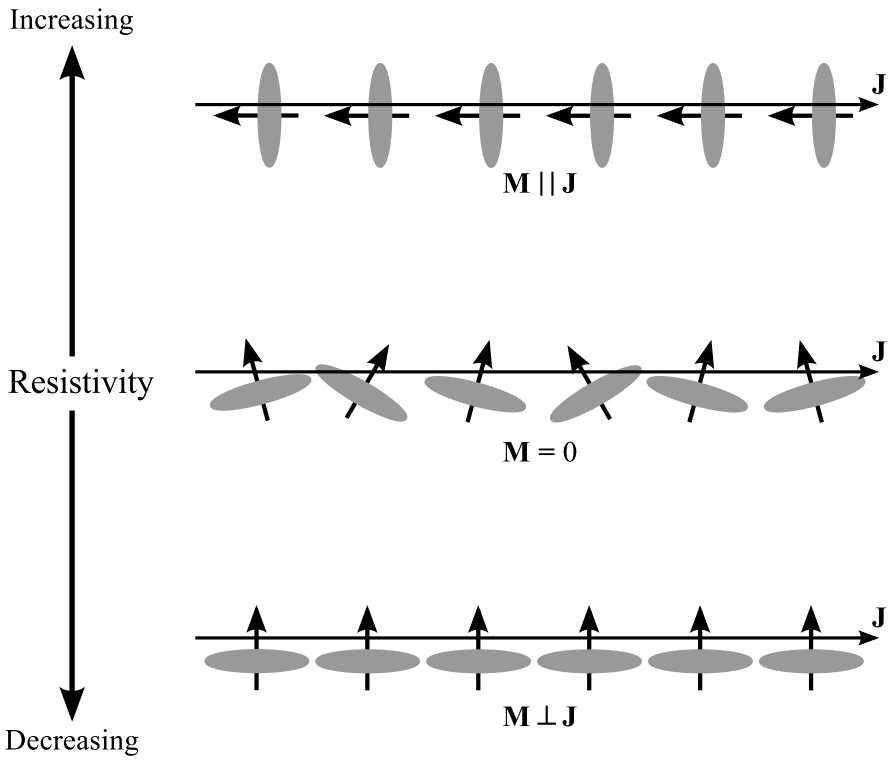

Figure 1.2.4.4: Schematic representation of the AMR effect. The atoms of the solid are represented by an atomic magnetic moment surrounded by a cloud of electrons.

ically; therefore, they are depicted in Figure 1.2.4.5 along with their corresponding hypothetical resistance change curves.

The spin-valve configuration (Figure 1.2.4.5(a)) utilizes an exchange biased antiferromagnetic (AF) and ferromagnetic (FM) layer to create a pinned layer (PL) with a fixed magnetization direction[5]. A second FM layer is isolated from the PL by means of a non-magnetic spacer layer (SL). This isolated FM layer is termed the free layer (FL) since its magnetization direction is free to follow the applied magnetic field. In the case of the diagram (Figure 1.2.4.5(a)), the PL has a magnetization along the negative field direction such that the magnetizations of the FL and PL are parallel for an applied magnetic field of $\mathbf{H} < 0$,

[5]This coupling mechanism arises when an AF/FM interface is cooled through the Néel temperature in the presence of an applied magnetic field. After the cooling process, the AF resists reorientation of its magnetic moments effectively pinning those of the FM along the direction of the applied field used during the cooling process.

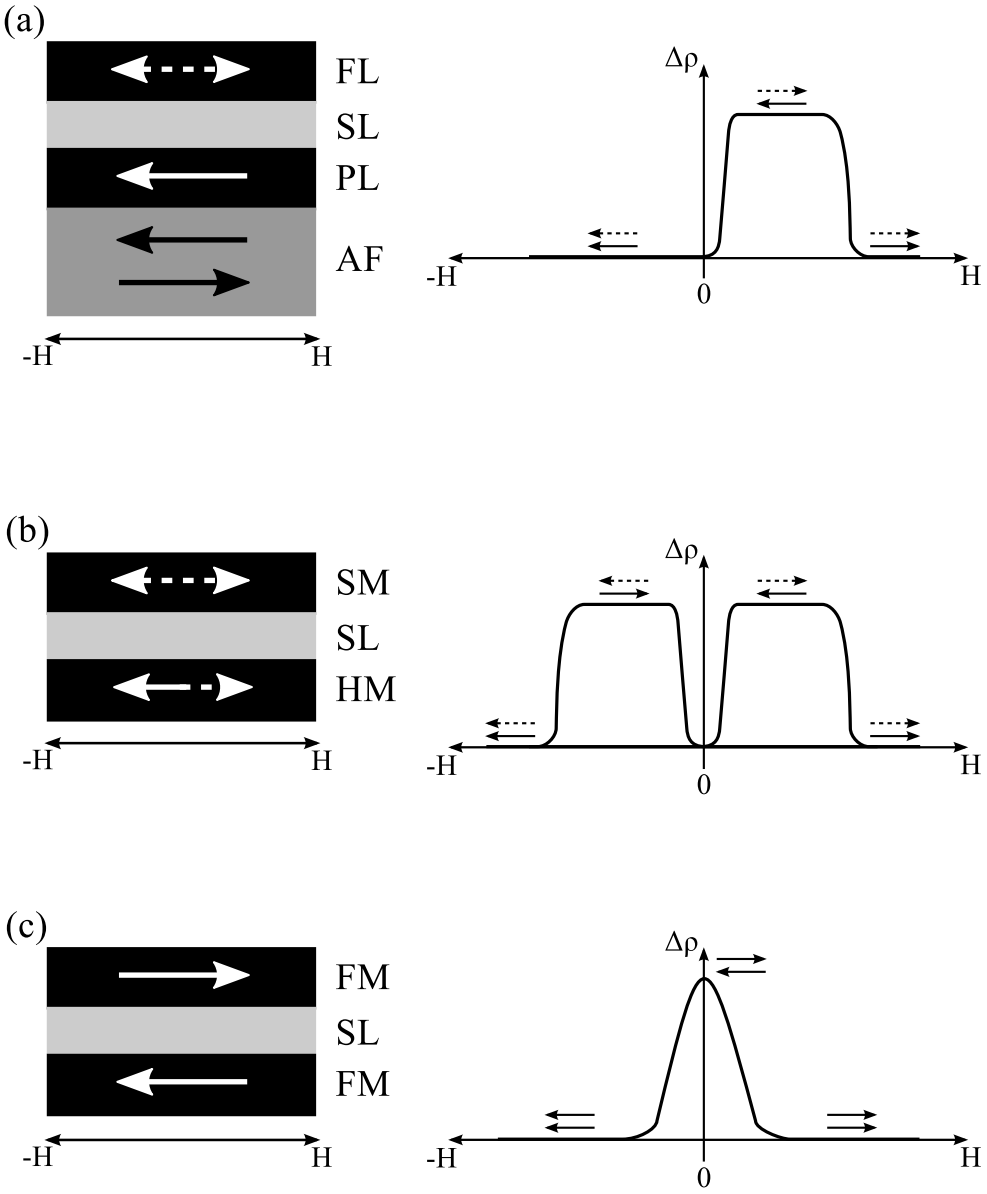

Figure 1.2.4.5: (a) Spin-valve configuration. The antiferromagnetic layer (AF) pins the magnetization of one of the ferromagnetic layers (PL). A non-magnetic spacer layer (SL) separates this from the free layer (FL), which is free to rotate with the applied magnetic field. (b) Pseudo-spin-valve configuration. A soft magnetic layer (SM) and hard magnetic layer (HM) are separated by SL. The coercivity mismatch between SM and HM causes SM to be more sensitive to magnetization reversal by an applied magnetic field. (c) Exchange coupled configuration. Two ferromagnetic layers (FM) are antiferromagnetically coupled across SL. The application of a magnetic field aligns the magnetizations of the FM layers.

resulting in a low magnetoresistance state. The application of a magnetic field $\mathbf{H} > 0$ switches the magnetization of the FL resulting in an antiparallel configuration between the magnetizations of the FL and PL. This is the high magnetoresistance state. Further increase of the applied field in this direction overcomes the effects of the exchange biasing such that the magnetization of the PL reorients parallel to the applied field. Once again, the magnetizations of the FL and PL are parallel resulting in a low magnetoresistance state. Spin-valve structures in this configuration typically exhibit resistance change ratios of $< 10\%$ at room temperature, but careful engineering and material selection can increase this to as high as 20% [34]. However, their usefulness lies not so much in the magnitude of their resistance change, but more in their ability to sense small magnetic fields since the initial change from low resistance to high resistance occurs at low magnetic field strengths. This is where spin-valve structures find technological applications [35].

The pseudo-spin-valve configuration (Figure 1.2.4.5(b)) is similar to the spin-valve, except no antiferomagnetically pinned layer is used. Instead, two different FM layers having different coercivities are utilized. The hard magnetic layer (HM) has a higher coercivity than the soft magnetic layer (SM) meaning that larger magnetic field strengths are required to reorient the magnetization of the HM layer. The application of a magnetic field (either $\mathbf{H} < 0$ or $\mathbf{H} > 0$) causes the magnetization of the SM layer to reorient along the applied field resulting in an antiparallel configuration between the magnetizations of the SM and HM layers. This is the high magnetoresistance state. Further increase of the applied field reorients the HM layer along the applied field resulting in a parallel configuration between the magnetizations of the SM and HM layers. This is the low magnetoresistance state. Pseudo-spin-valve structures typically exhibit resistance change ratios of $< 10\%$ [34] at room tem-

perature, and can find technological applications in magnetic random-access memory [36].

The exchange coupled configuration (Figure 1.2.4.5(c)) utilizes two interlayer exchange coupled FM layers separated by a non-magnetic SL. The exchange interaction in this situation is akin to that of the long-range Ruderman-Kittel-Kasuya-Yosida (RKKY) interaction [37–39][6] where the coupling oscillates between ferromagnetic and antiferromagnetic depending on the thickness of the SL [40, 41]. The high magnetoresistance state occurs in the absence of an applied magnetic field when the two FM layers are antiferromagnetically coupled. The application of a magnetic field aligns the magnetizations of the FM layers such that a low magnetoresistance state is observed. Exchange coupled structures exhibit resistance change ratios of $> 10\%$ at room temperature, and find applications as magnetic sensors [34].

As a final note, the actual conduction mechanism in GMR multilayers will be discussed in terms of a two-current model [42]. It is assumed here that the current passing through the GMR layer can be decomposed into two separate channels: one carrying spin-up electrons and one carrying spin-down electrons. In the ferromagnetic layers, the resistance to flow perceived by electrons when their spin is parallel to the magnetization is denoted as R_p; when their spin is antiparallel to the magnetization direction the resistance is denoted as R_{ap}. Based on this it is possible to construct a resistor network diagram for the two configurations of the GMR multilayer, namely the parallel and antiparallel configurations, based on the relative orientations of the FM layers. This is depicted in Figure 1.2.4.6. In the parallel configuration (Figure 1.2.4.6(a)) both FM layers are parallel to the spins of one current channel and antiparallel

[6]When two magnetic atoms are too far apart to interact directly with one another, they can utilize the surrounding conduction electrons to effectively couple their magnetic moments to one another. Depending on the distance between the two atoms this coupling is either antiferromagnetic or ferromagnetic.

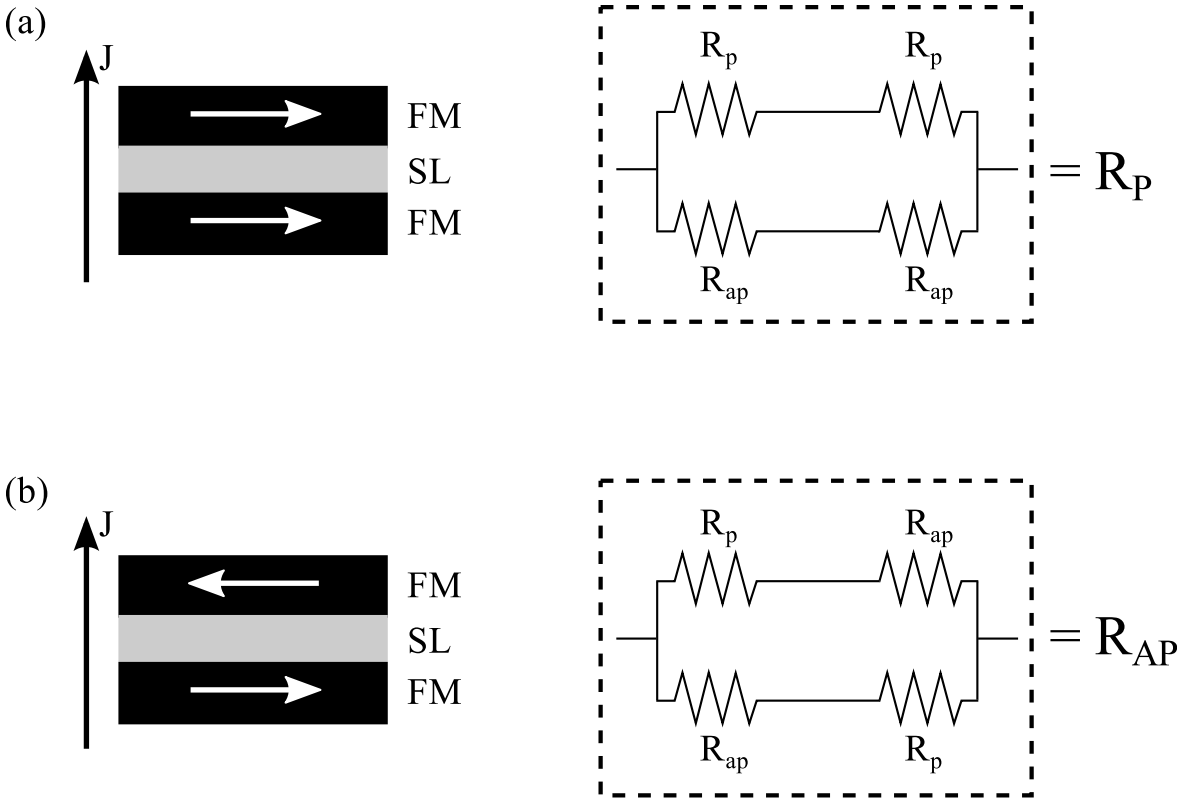

Figure 1.2.4.6: (a) Parallel configuration of the FM layers. The net resistance of the multilayer in this case is denoted as R_P. (b) Antiparallel configuration of the FM layers. The net resistance of the multilayer in this case is denoted as R_{AP}.

to the spins of the other. This results in one channel experiencing a resistance proportional to $2R_p$ while the other experiences a resistance proportional to $2R_{ap}$. In the antiparallel configuration (Figure 1.2.4.6(b)) both current channels experience a resistance proportional to $R_p + R_{ap}$. The net resistance of each configuration can thus be written as

$$R_P = \frac{2R_pR_{ap}}{R_p + R_{ap}} \tag{1.2.4.2a}$$

$$R_{AP} = \frac{R_p + R_{ap}}{2} \tag{1.2.4.2b}$$

Mott [43] showed that the majority of the current is carried by 4s electrons in the ferromagnetic transition metals, and that the resistivity is dominated by interband transitions from the 4s to the 3d band caused by spin-preserving scattering events. From Figure 1.2.4.1 it is apparent that the majority spin 3d sub band is full at the Fermi level such that 4s conduction electrons cannot scatter into these states. This means that only 4s electrons with spins antiparallel to the magnetization direction can make the transition to the 3d band; and, therefore it can be concluded that $R_{ap} > R_p$. Using this fact it can be shown that $R_{AP} > R_P$, which corroborates with the resistance change curves of Figure 1.2.4.5.

1.3 Thesis Scope

In Chapter 2, a THz-TDS system incorporating a high field strength electromagnet is presented. The system design and construction are discussed along with its performance. Several characterization processes are used to determine its range of functionality.

Near-field coupling of non-resonant, localized surface plasmon modes is responsible for the transmission of THz electromagnetic radiation through dense ensembles of subwavelength metallic microparticles. Due to the nature of this

interaction these particles represent a good platform for studying material junctions at THz frequencies. Therefore, Chapter 3 focuses on studying the effect of particle size on near-field particle plasmon coupling using THz-TDS. The results of this study provide an upper limit for the optimum particle diameter of the constituents of the ensemble such that induced localized plasmon modes remain dipolar and the transport of energy through the ensemble remains efficient.

In Chapter 4, the GMR effect is investigated as a potential candidate for introducing an active element to THz components. By modulating the resistivity of individual subwavelength metallic particles it is shown that an applied magnetic field can affect the transmission of THz radiation through an ensemble of these particles. This is accomplished by depositing GMR multilayers onto the surface of the particles and then using an applied magnetic field to adjust the resistivity of the multilayer. The results of this study provide preliminary evidence that the GMR effect can indeed be utilized to actively modulate THz radiation in the plasmonic regime.

In Chapter 5, a series of metallic resonators are studied with the THz-TDS system described in Chapter 2. Broadband simulations are utilized to first design the structures and then they are fabricated for experimental verification. Passive operation of these devices is demonstrated and active operation is investigated. For active operation, the structures are made of a ferromagnetic metallic film and the magnetoresistance effect is studied as a candidate for control of their resonant response.

In Chapter 6, a previous transmission experiment performed on a ferromagnetic metallic microparticle ensemble is re-visited. Using THz-TDS, the transparency of this ensemble is shown to depend on the magnitude and relative orientation of an applied magnetic field due to magnetoresistance effects,

as expected from previous experiments. Also, it is shown that modulation of the ensemble transparency due to magnetoresistance effects is sensitive to the index of refraction of the medium hosting the particle ensemble.

Chapter 1 References

[1] J. B. Pendry, "Negative Refraction Makes a Perfect Lens," *Phys. Rev. Lett.*, vol. 85, no. 18, pp. 3966–9, 2000.

[2] I. I. Smolyaninov, Y.-J. Hung, and C. C. Davis, "Magnifying Superlens in the Visible Frequency Range," *Science*, vol. 315, pp. 1699–1701, 2007.

[3] D. Schurig, J. J. Mock, B. J. Justice, S. A. Cummer, J. B. Pendry, A. F. Starr, and D. R. Smith, "Metamaterial Electromagnetic Cloak at Microwave Frequencies," *Science*, vol. 314, pp. 977–80, 2006.

[4] D. Qu, D. Grischkowsky, and W. Zhang, "Terahertz transmission properties of thin, subwavelength metallic hole arrays," *Opt. Lett.*, vol. 29, no. 8, pp. 896–8, 2004.

[5] Y. Ma, Q. Chen, A. Khalid, S. C. Saha, and D. R. S. Cumming, "Terahertz dual-band resonator on silicon," *Opt. Lett.*, vol. 35, no. 4, pp. 469–71, 2010.

[6] C. Jansen, I. A. I. Al-Naib, N. Born, and M. Koch, "Terahertz metasurfaces with high Q-factors," *Appl. Phys. Lett.*, vol. 98, no. 5, pp. 051 109/1–3, 2011.

[7] J. F. O'Hara, R. Singh, I. Brener, E. Smirnova, J. Han, A. J. Taylor, and W. Zhang, "Thin-film sensing with planar terahertz metamaterials: sensitivity and limitations," *Opt. Exp.*, vol. 16, no. 3, pp. 1786–95, 2008.

[8] I. A. I. Al-Naib, C. Jansen, and M. Koch, "Thin-film sensing with planar

asymmetric metamaterial resonators," *Appl. Phys. Lett.*, vol. 93, no. 8, pp. 083 507/1–3, 2008.

[9] K. J. Chau, G. D. Dice, and A. Y. Elezzabi, "Coherent Plasmonic Enhanced Terahertz Transmission through Random Metallic Media," *Phys. Rev. Lett.*, vol. 94, no. 17, pp. 173 904/1–4, 2005.

[10] K. J. Chau and A. Y. Elezzabi, "Terahertz transmission through ensembles of subwavelength-size metallic particles," *Phys. Rev. B*, vol. 72, no. 7, pp. 075 110/1–9, 2005.

[11] ——, "Photonic Anisotropic Magnetoresistance in Dense Co Particle Ensembles," *Phys. Rev. Lett.*, vol. 96, no. 3, pp. 033 903/1–4, 2006.

[12] K. J. Chau, M. Johnson, and A. Y. Elezzabi, "Electron-Spin-Dependent Terahertz Light Transport in Spintronic-Plasmonic Media," *Phys. Rev. Lett.*, vol. 98, no. 13, pp. 133 901/1–4, 2007.

[13] K. J. Chau, C. A. Baron, and A. Y. Elezzabi, "Isotropic photonic magnetoresistance," *Appl. Phys. Lett.*, vol. 90, no. 12, pp. 121 122/1–3, 2007.

[14] M. Hangyo, M. Tani, and T. Nagashima, "Terahertz Time-Domain Spectroscopy of Solids: A Review," *Int. J. Infrared Milli.*, vol. 26, no. 12, pp. 1661–90, 2005.

[15] D. J. Griffiths, *Introduction to Electrodynamics*, 3rd ed. Upper Saddle River, NJ: Prentice Hall, 1999.

[16] J. D. Jackson, *Classical Electrodynamics*, 3rd ed. New York, NY: John Wiley & Sons, 1999.

[17] S. A. Maier, *Plasmonics: Fundamentals and Applications*. New York, NY: Springer, 2007.

[18] C. Kittel, *Introduction to Solid State Physics*, 8th ed. New York, NY: John Wiley & Sons, 2005.

[19] N. W. Ashcroft and N. D. Mermin, *Solid State Physics*. Orlando, FL: Harcourt, 1976.

[20] M. P. Marder, *Condensed Matter Physics*. New York, NY: John Wiley & Sons, 2000.

[21] N. A. Spaldin, *Magnetic Materials: Fundamentals and Applications*, 2nd ed. Cambridge: Cambridge University Press, 2011.

[22] M. R. F. Jensen, S. A. Feiven, T. J. Parker, and R. E. Camley, "Experimental determination of magnetic polariton dispersion curves in FeF_2," *Phys. Rev. B*, vol. 55, no. 5, pp. 2745–8, 1997.

[23] J. N. Gollub, D. R. Smith, D. C. Vier, T. Perram, and J. J. Mock, "Experimental characterization of magnetic surface plasmons on metamaterials with negative permeability," *Phys. Rev. B*, vol. 71, no. 19, pp. 195 402/1–7, 2005.

[24] A. D. Rakić, A. B. Djurišić, J. M. Elazar, and M. L. Majewski, "Optical properties of metallic films for vertical-cavity optoelectronic devices," *Appl. Opt.*, vol. 37, no. 22, pp. 5271–83, 1998.

[25] E. Kretschmann and H. Raether, "Radiative decay of non radiative surface plasmons excited by light," *Z. Naturforschung A*, vol. 23A, no. 12, pp. 2135–6, 1968.

[26] A. Otto, "Excitation of nonradiative surface plasma waves in silver by the method of frustrated total reflection," *Z. Physik A*, vol. 216, no. 4, pp. 398–410, 1968.

[27] A. B. Pippard, *Magnetoresistance in Metals*. Cambridge: Cambridge University Press, 1989.

[28] H. C. Van Elst, "The Anisotropy in the Magneto-Resistance of Some Nickel Alloys," *Physica*, vol. 25, pp. 708–20, 1959.

[29] T. R. McGuire and R. I. Potter, "Anisotropic Magnetoresistance in Ferromagnetic 3d Alloys," *IEEE T. Magn.*, vol. 11, no. 4, pp. 1018–38, 1975.

[30] B. Dieny, V. S. Speriosu, S. S. P. Parkin, B. A. Gurney, D. R. Wilhoit, and D. Mauri, "Giant magnetoresistance in soft ferromagnetic multilayers," *Phys. Rev. B*, vol. 43, no. 1, pp. 1297–1300, 1991.

[31] A. V. Pohm, B. A. Everitt, R. S. Beech, and J. M. Daughton, "Bias field and end effects on the switching thresholds of "pseudo spin valve" memory cells," *IEEE T. Magn.*, vol. 33, no. 5, pp. 3280–2, 1997.

[32] M. N. Baibich, J. M. Broto, A. Fert, F. N. V. Dau, F. Petroff, P. Eitenne, G. Creuzet, A. Friederich, and J. Chazelas, "Giant Magnetoresistance of (001)Fe/(001)Cr Magnetic Superlattices," *Phys. Rev. Lett.*, vol. 61, no. 21, pp. 2472–5, 1988.

[33] G. Binasch, P. Grünberg, F. Saurenbach, and W. Zinn, "Enhanced magnetoresistance in layered magnetic structures with antiferromagnetic interlayer exchange," *Phys. Rev. B*, vol. 39, no. 7, pp. 4828–30, 1989.

[34] E. Hirota, H. Sakakima, and K. Inomata, *Giant Magneto-Resistance Devices*. Berlin: Springer-Verlag, 2002.

[35] S. Parkin, X. Jiang, C. Kaiser, A. Panchula, K. Roche, and M. Samant, "Magnetically Engineered Spintronic Sensors and Memory," *Proc. IEEE*, vol. 91, no. 5, pp. 661–80, 2003.

[36] H. Sakakima, Y. Irie, Y. Kawawake, and M. Satomi, "Spin-valve multilayers of [H/Cu/S](H = Co, Co-Pt, or Co-Fe, S = NiFeCo) and memory cells," *J. Magn. Magn. Mater.*, vol. 156, pp. 405–6, 1996.

[37] M. A. Ruderman and C. Kittel, "Indirect Exchange Coupling of Nuclear Magnetic Moments by Conduction Electrons," *Phys. Rev.*, vol. 96, no. 1, pp. 99–102, 1954.

[38] T. Kasuya, "A Theory of Metallic Ferro- and Antiferromagnetism on Zener's Model," *Prog. Theor. Phys.*, vol. 16, no. 1, pp. 45–57, 1956.

[39] K. Yosida, "Magnetic Properties of Cu-Mn Alloys," *Phys. Rev.*, vol. 106, no. 5, pp. 893–8, 1957.

[40] W. Baltensperger and J. S. Helman, "Ruderman-Kittel coupling between ferromagnets separated by a nonmagnetic layer," *Appl. Phys. Lett.*, vol. 57, no. 27, pp. 2954–5, 1990.

[41] S. S. P. Parkin, N. More, and K. P. Roche, "Oscillations in Exchange Coupling and Magnetoresistance in Metallic Superlattic Structures: Co/Ru, Co/Cr, and Fe/Cr," *Phys. Rev. Lett.*, vol. 64, no. 19, pp. 2304–7, 1990.

[42] E. Y. Tsymbal and D. G. Pettifor, *Solid State Physics*. Academic Press, 2001, vol. 56, ch. 2, pp. 113–237.

[43] N. F. Mott, "The Electrical Conductivity of Transition Metals," *Proc. R. Soc. Lon. Ser.-A*, vol. 153, no. 880, pp. 699–717, 1936.

Chapter 2

The Terahertz Spectroscopy System

2.1 Background

The THz band of the electromagnetic spectrum is loosely defined as those frequencies falling within the range of 0.1 - 30 THz [1, 2]. An increasingly high level of interest lies in this frequency range due to the existence of inherently broadband sources and phase sensitive detection schemes. In other words, generation and detection of THz radiation is typically a time-domain technique where the electric field vector is measured directly, providing access to both amplitude and phase information. Along with its subpicosecond temporal resolution, these attractive properties have led to the wide use of THz-TDS in areas including: the recognition [3, 4] and characterization [5, 6] of materials, the study of fundamental physical processes [7, 8], and even plasmonics [9] and metamaterials [10]. A review of THz spectroscopy techniques and applications can be found in [11, 12].

As outlined in the introduction, this thesis work makes use of the THz-TDS

technique to study magnetoresistance phenomena in subwavelength media. To do this, a system capable of generating and detecting broadband THz radiation within the coils of a high field strength electromagnet was constructed. Generation and detection of THz radiation is achieved through photoconductive (PC) switching [13, 14] and electro-optic (EO) sampling [15, 16], respectively, which will be outlined in the following subsections.

2.1.1 Terahertz Generation by Photoconductive Switching

The method used in this thesis work for generating THz radiation relies on the ultrafast gating of a biased metallic coplanar strip line antenna by femtosecond laser pulses. The antenna is fabricated on a high mobility, semiconducting substrate, which, when irradiated by an ultrafast above band-gap laser pulse, becomes conductive due to the generation of free charge carriers. These free charges are subsequently accelerated across the antenna gap by the biasing electric field resulting in an ultrafast current transient. It is this current transient that acts as a source of broadband electromagnetic radiation lying in the THz frequency range. Figure 2.1.1.1 gives a simplified depiction of this generation scheme. For a more detailed analysis of this process see [17], for example.

2.1.2 Terahertz Detection by Electro-Optic Sampling

To detect THz radiation a <111> ZnSe EO crystal is employed. Such a crystal experiences a change in its index ellipsoid under the influence of a dc, or nearly dc, electric field due to the Pockels effect [18]. Therefore, when a beam of THz radiation copropagates with a linearly polarized probe beam (i.e. ultrafast

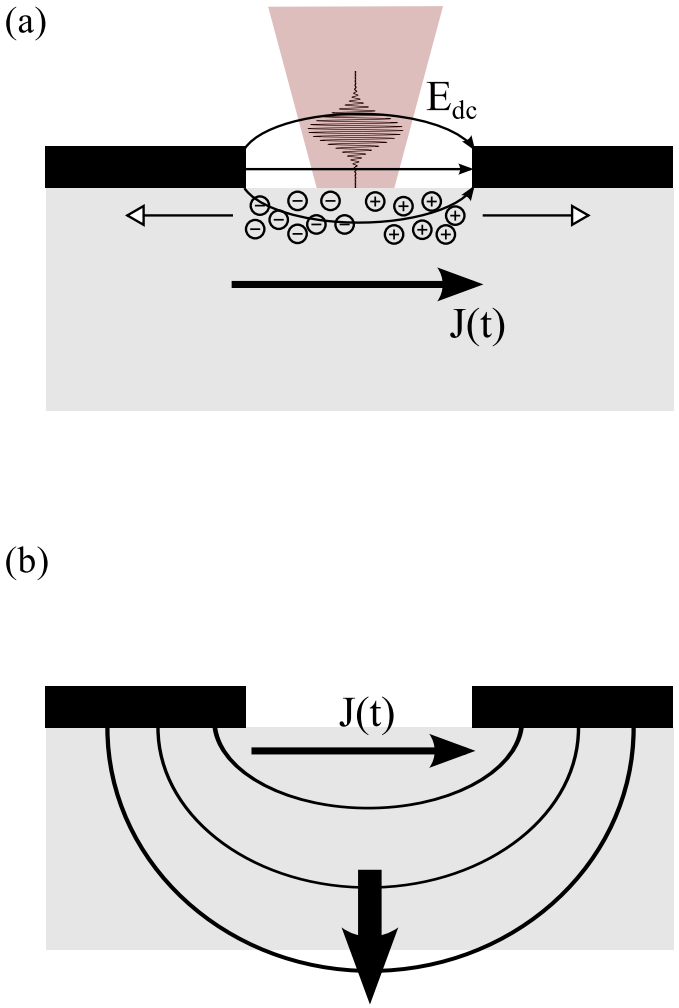

Figure 2.1.1.1: Cartoon representation of photoconductive generation of THz radiation. (a) An ultrafast laser pulse generates free carriers which are subsequently accelerated in the static electric field, E_{dc}, resulting in a current transient, $J(t)$. (b) The current transient radiates electromagnetic energy away from the transmission line.

laser pulse) through the crystal, the electric field of the probe beam experiences a retardation caused by the refractive index change induced by the THz electric field. This retardation is detected using a quarter wave-plate and Wollaston prism to split the probe beam into its orthogonal polarization components, which are then subtracted from each other via a balanced photodiode detector. It is this detected intensity difference between the two orthogonal components of the probe beam that is linearly proportional to the instantaneous THz electric field strength as [19]

$$\Delta \mathrm{I} \propto E_{THz} d \sin 3\theta$$

where E_{THz} is the amplitude of the THz electric field, d is the crystal thickness and θ is the polarization angle of the THz and probe beam electric field with respect to the azimuthal rotation of the crystal. The crystal is symmetric under 60° azimuthal rotation and antisymmetric under 30° azimuthal rotation. Therefore, the polarization state of the THz electric field can be mapped out by rotating the crystal and monitoring the balanced photodiode output. To acquire the full temporal waveform the relative delay between the arrival time of the THz and probe pulses in the crystal is adjusted while monitoring the output from the balanced photodiodes. For a more detailed treatment of EO sampling in zinc-blende crystals see the article by Planken et al. [20] and the thesis work of Jonathan Holzman [19]

2.2 System Design and Performance

The complete layout for the freespace THz-TDS system constructed for this thesis work is given in Figure 2.2.0.1. A Kerr-lens mode-locked Ti:Sapphire oscillator system (Femtolasers FEMTOSOURCE Scientific PRO) generates $\sim$ 10 fs laser pulses centered at 794 nm with a repetition rate of 75 MHz. This

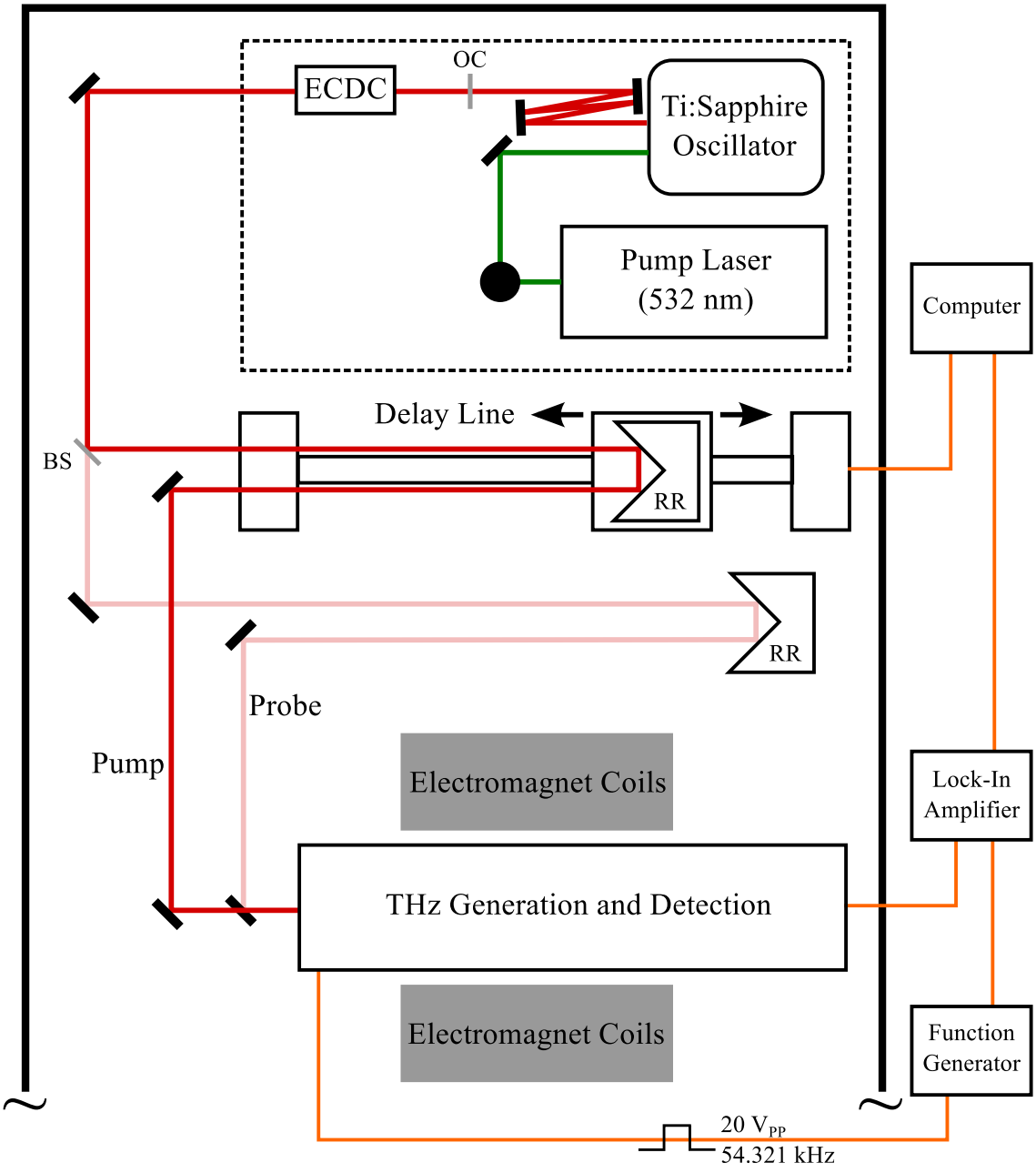

Figure 2.2.0.1: Birds-eye view of the THz-TDS system. The output from the laser enclosure (dashed box) is split into a pump and probe beam using a 90(R)/10(T) beamsplitter (BS). The delay line utilizes a moving retro-reflector (RR) to adjust the relative temporal delay between the pump and probe beams such that the THz waveform can be acquired in the time-domain.

system consists of a tightly focused, folded cavity as depicted in Figure 2.2.0.2. An excellent discussion on cavities of this design can be found in [21]. The

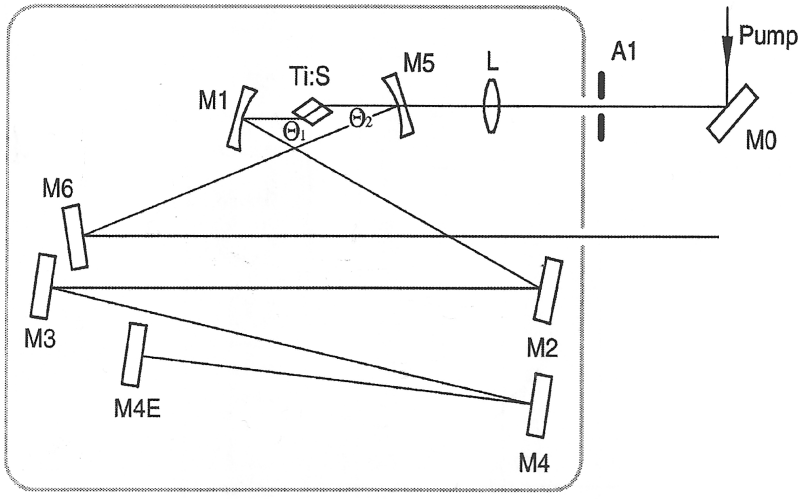

Figure 2.2.0.2: Schematic of the optical components located inside the oscillator. A1: aperture; L: lens, M1, M5: curved mirrors; M2, M3, M4, M4E, M6: dispersive mirrors; Θ_1, Θ_2: cavity folding angles; Ti:S: gain medium. This schematic is taken from the Femtolasers FEMTOSOURCE Scientific PRO user manual.

non-curved mirrors in both the short and long arm of the cavity contain special dielectric coatings [22] which provide compensation for the dispersion introduced by the elements of the cavity, particularly the gain medium. The actual installation of this system involves alignment of the pump laser beam (Coherent Verdi V6)[1] into the oscillator along with setup of the long arm of the cavity. The latter consists of aligning two mirrors such that the amplified spontaneous emission (ASE) exiting the oscillator hits each mirror twice before proceeding to the output coupler (OC). Following this, these three elements must be adjusted to reflect the ASE back upon itself through the gain medium, which results in continuous wave (CW) operation. At this stage it is necessary to adjust the key components of the system to achieve maximum CW output

[1]The pump laser outputs a 3.75 W, continuous wave laser beam at 532 nm.

power (i.e. optimal overlap between the beam waists of the pump beam and CW beam inside the gain medium), which should be in the range of 500 - 600 mW. These components are the position of the lens used to focus the pump beam into the gain medium, the position of the gain medium between the two curved mirrors and the separation distance of the two curved mirrors (i.e. the stability range). Once the maximum CW power is achieved, the stability range can be adjusted to make CW operation less favorable and mode-locked operation more favorable. At this stage it is possible to mode-lock the laser by introducing a perturbation to the cavity length. This consists of "bumping" the cavity end mirror, M4E, along the beam path. If the cavity is optimized then the laser should mode-lock resulting in $\sim$ 10 fs duration pulses exiting the cavity through the OC. The average output power of the laser is 485 mW for mode-locked operation and 530 mW for CW operation. Note that after the OC, the output laser beam is passed through an extra-cavity dispersion compensation (ECDC) module to precompensate for some of the dispersion introduced by the optics outside the laser enclosure, particularly the beam splitter. The amplitude spectrum of the mode-locked output from the laser enclosure is show in Figure 2.2.0.3.

As indicated by the schematic, the output from the laser enclosure is split into a pump and probe beam by a beamsplitter (BS). The pump beam is directed towards a temporal delay line consisting of a retro-reflector (RR) mounted on a moving stage. A stepper motor is used to achieve a temporal resolution of 42.0 ± 0.6 fs/step, corresponding to a change in distance of 12.6 ± 0.2 µm/step. From the delay line the pump beam is directed towards the THz system where it is used to generate THz radiation. On the other hand, the probe beam is directed towards a fixed retro-reflector from where it proceeds to the THz system to be used to detect THz radiation.

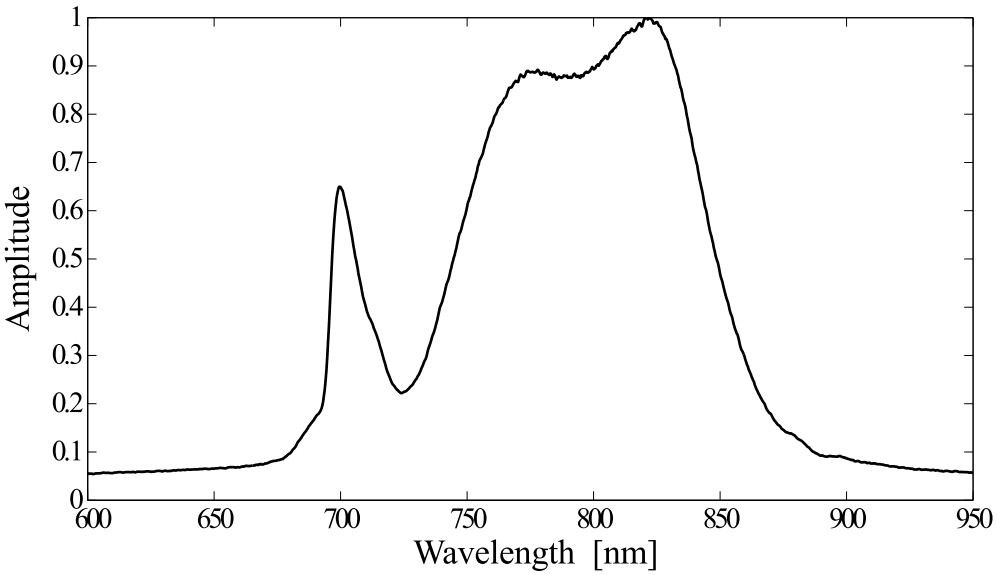

Figure 2.2.0.3: Amplitude spectrum of the mode-locked Ti:Sapphire oscillator output.

The THz generation and detection system is constructed between the coils of an electromagnet such that the sample under study lies at the center of the gap between the magnet's poles. A schematic representation of this part of the setup is shown in Figure 2.2.0.4. To generate THz radiation, the pump beam (355 mW) is focused by a 10x microscope objective onto the PC switch, which consists of a 20 $V_{p\text{-}p}$ biased[2] coplanar strip line fabricated on a semi-insulating GaAs substrate. The generated, dipole-like radiation is collected, collimated and focused by a pair of 2" diameter off-axis parabolic mirrors such that the focal point of the system lies at the center of the gap between the electromagnet's poles. A similar pair of parabolic reflectors is used to collimate and focus the THz beam onto the EO crystal. For detection, the THz beam is focused collinearly with the probe beam (20 mW) onto a 0.5 mm thick <111> ZnSe crystal. After propagating through the crystal, the probe beam is circularly polarized by a quarter-wave plate ($\lambda/4$) and split into its orthogo-

[2]The biasing voltage is a 54.321 kHz square waveform. An ac bias is applied such that a lock-in detection scheme can be used for acquiring the time-domain THz signal.

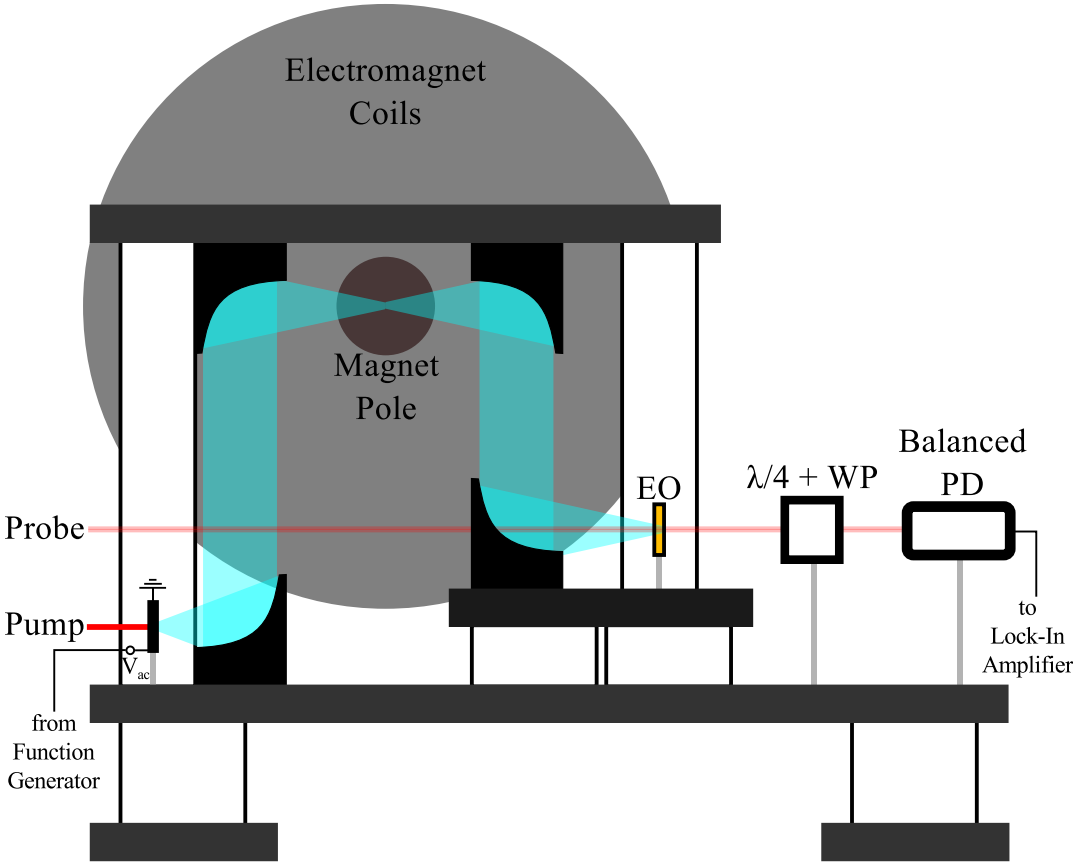

Figure 2.2.0.4: Profile view of the THz generation and detection system. The focal point of the THz beam is located at the center of the gap between the electromagnet poles; this is where the sample is situated during experiments.

nal components by a Wollaston prism (WP). A balanced photodiode detector (Newport Nirvana 2007) is then used to convert the power difference between the probe beam components into a voltage signal, which is comparable to the instantaneous THz electric field strength. This voltage signal is subsequently amplified using a low-noise preamplifier (Stanford Research Systems SR560) from where it is passed to a lock-in amplifier (Stanford Research Systems SR830). The lock-in is synchronized with the function generator used to bias the PC switch such that the detection scheme is inherently low noise. CAD representations of the electromagnet and stage holding the THz generation and detection components are depicted in Figure 2.2.0.5 and Figure 2.2.0.6,

respectively. Photographs of the completed system can be found in Appendix C.

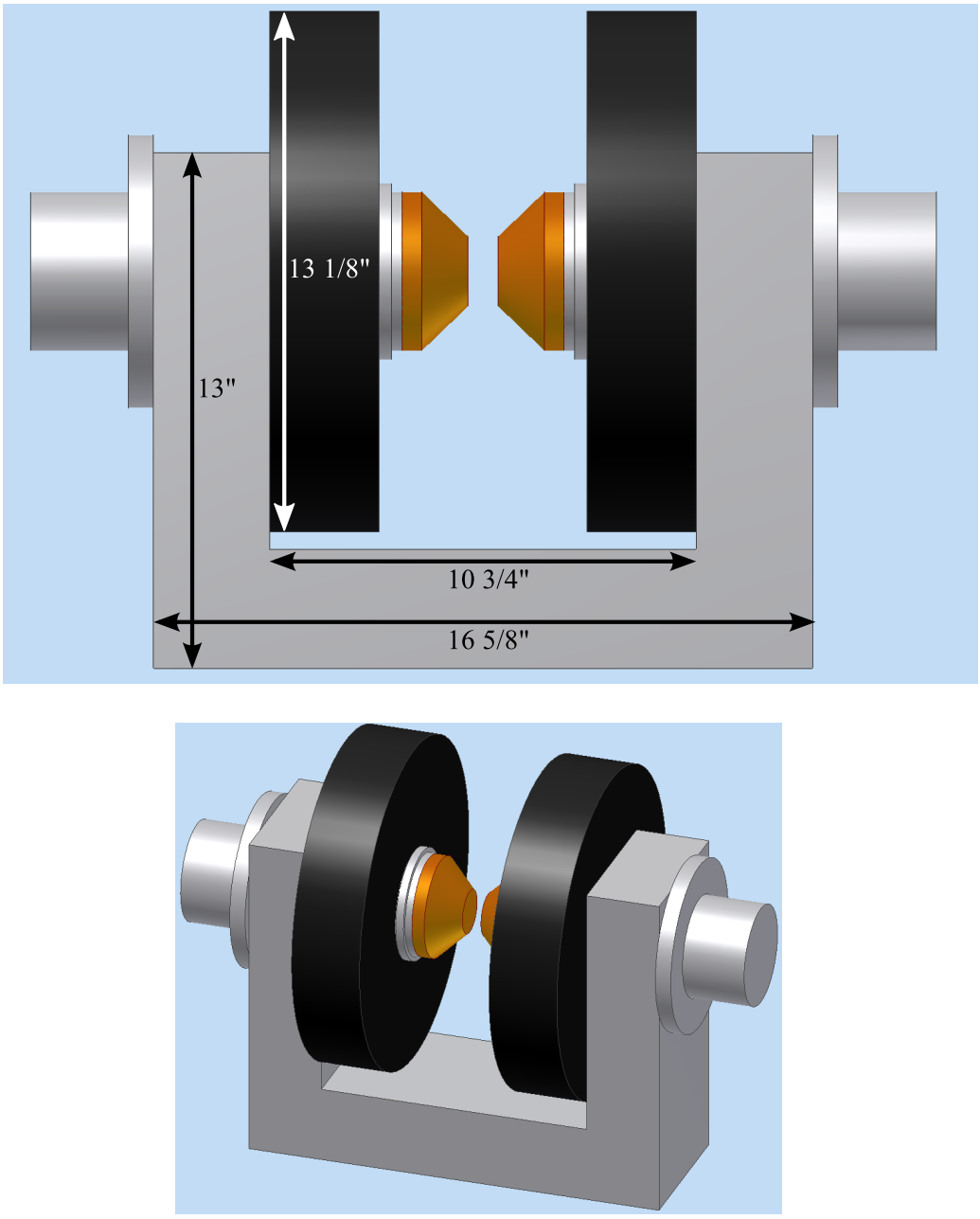

Figure 2.2.0.5: CAD drawing of the electromagnet used in the construction of the THz-TDS system.

To acquire the entire time-domain THz waveform the relative delay between the pump and probe beams is adjusted while recording the voltage signal from the lock-in. This results in a single-cycle, $\sim$ 1 ps pulse of THz radiation

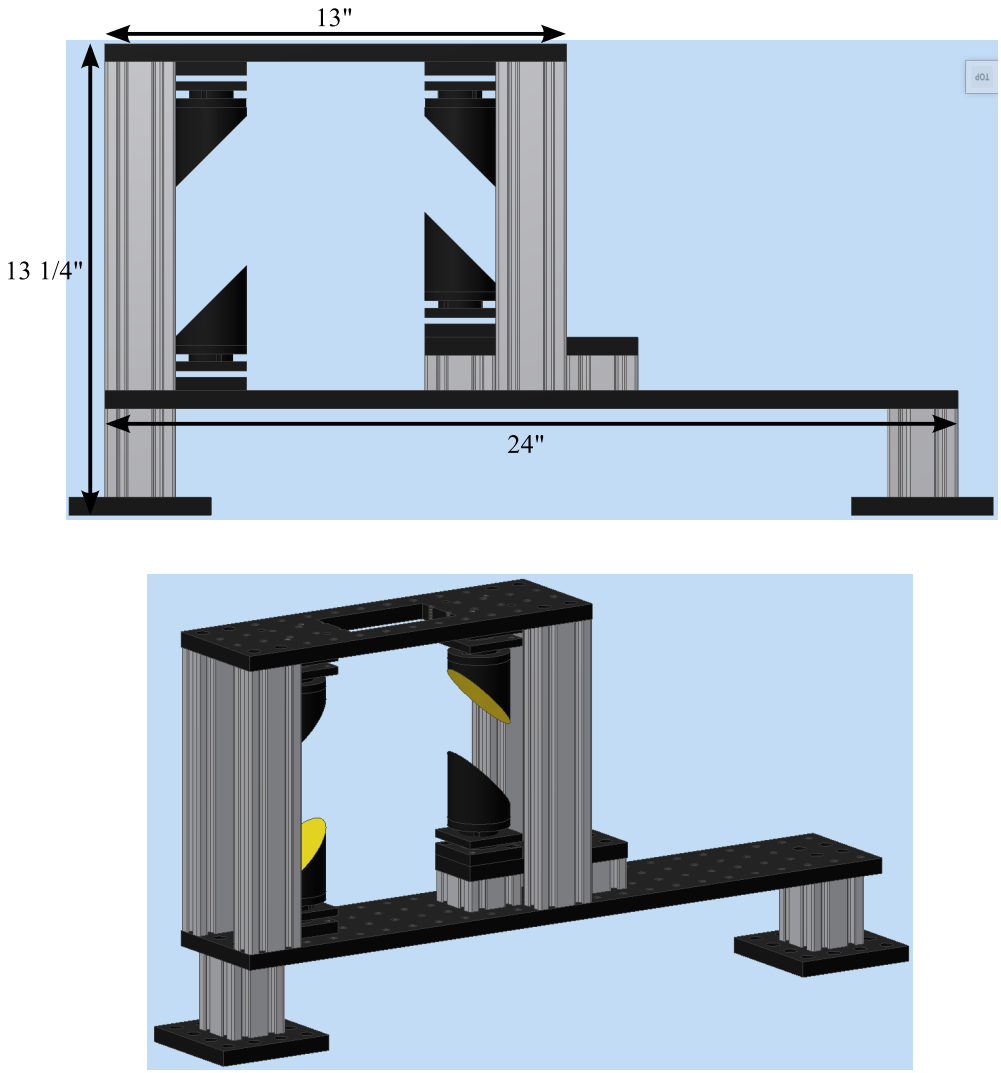

Figure 2.2.0.6: CAD drawing of the stage built to hold the THz generation and detection components inside the coils of the electromagnet.

having a center frequency of $\sim$ 0.7 THz and a bandwidth of $\sim$ 0.8 THz at full-width half-maximum (FWHM). A representative freespace THz waveform and its corresponding amplitude spectrum are plotted in Figure 2.2.0.7. Note that the oscillations following the main THz pulse are real and reproducible; they arise due to absorption caused by water vapor in the air [23, 24].

The accuracy of measurements taken with the THz system rely heavily upon the signal-to-noise ratio (SNR) and shot-to-shot stability of the acquired

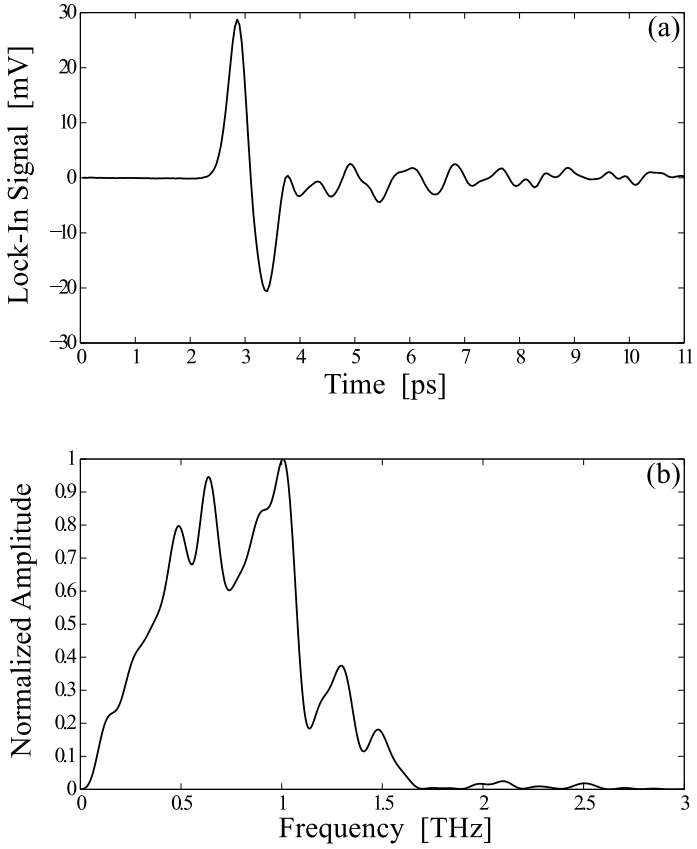

Figure 2.2.0.7: (a) Freespace THz pulse measured by scanning the relative delay between the pump and probe beams. (b) Normalized amplitude spectrum of the acquired pulse.

waveforms. Here, the SNR is defined as

$$\mathrm{SNR} = \frac{\mathrm{P}_s}{\mathrm{P}_n} \tag{2.2.0.1}$$

where P_s and P_n are the total power of the signal and noise, respectively. It should be noted that the lock-in amplifier used to acquire the THz waveforms includes a digital low-pass filter bank such that the SNR of the signal can be adjusted by changing the lock-in's time constant. However, increasing the duration of the time constant impacts the speed at which a THz waveform can be acquired since it takes longer for the lock-in output to stabilize after each step of the delay line. Table 2.1 gives the SNR and required acquisition time

Time Constant	SNR	Scan Time
10 ms	$>$ 4,000	1 min
30 ms	$>$ 11,000	2 min
100 ms	$>$ 25,000	4 min
300 ms	$>$ 74,000	7 min

Table 2.1: SNR and scan time of acquired freespace THz waveforms.

for an 11 ps scan (Figure 2.2.0.7(a)). Typically, a time constant of either 30 or 100 ms is used since a good tradeoff between SNR and acquisition speed is achieved. As mentioned above, the other important aspect of obtaining accurate measurements is based on the shot-to-shot stability of the system since most measurements require the comparison of consecutively acquired waveforms. By acquiring a series of 30 freespace waveforms and finding the average ratio of the amplitude spectrums of consecutive shots, a confidence band is identified. The shaded portion of Figure 2.2.0.8 represents this confidence interval. The vertical dashed lines enclose the useable bandwidth of the THz system, which ranges from 0.1 to 1.4 THz. Inside this range the maximum deviation is about $\pm 1.5\%$. Outside of this range the relative amplitudes of the spectral components become much less reliable. It should be noted that the observed noise arises due to the quantum nature of the THz generation

mechanism. The generation of free carriers in a semiconducting substrate is a statistical process based on the probability of exciting an electron in the valence band to the conduction band. This means that the generated free carrier density will not be identical for subsequent excitation pulses from the ultrafast pump pulse; therefore, the generated THz waveform will exhibit slight variations which are captured by Figure 2.2.0.8

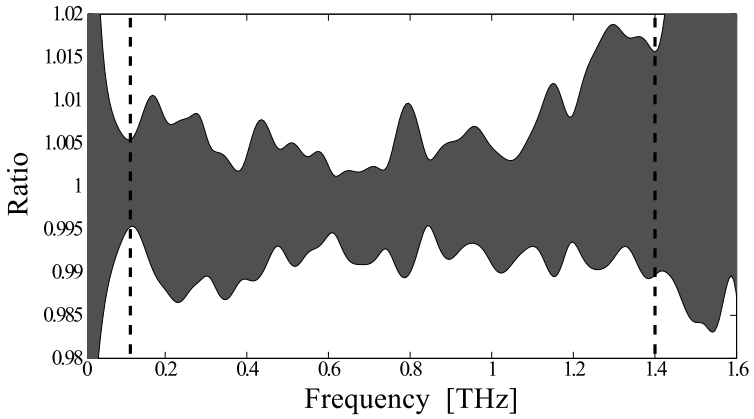

Figure 2.2.0.8: Confidence band for successive freespace THz waveforms acquired with the experimental setup. The usable bandwidth is found to be in the range of 0.1 to 1.4 THz.

One other important characteristic of the generated THz electromagnetic pulse is the polarization purity of the radiation. The PC switch is commonly approximated as an ideal dipole source, but it does not produce purely linearly polarized electromagnetic radiation. This means that a cross-polarized component lying perpendicular to the oscillation direction of the dipole will be present. As mentioned above, the polarization state of the THz radiation can be mapped out by rotating the EO crystal and monitoring the output from the balanced photodiodes. A polar plot of the THz polarization is depicted in Figure 2.2.0.9. As can be seen here, the THz pulse contains a noticeable cross-polarized component such that the electromagnetic radiation is indeed not perfectly linearly polarized. To quantify this, $\sim$ 85% of the radiated

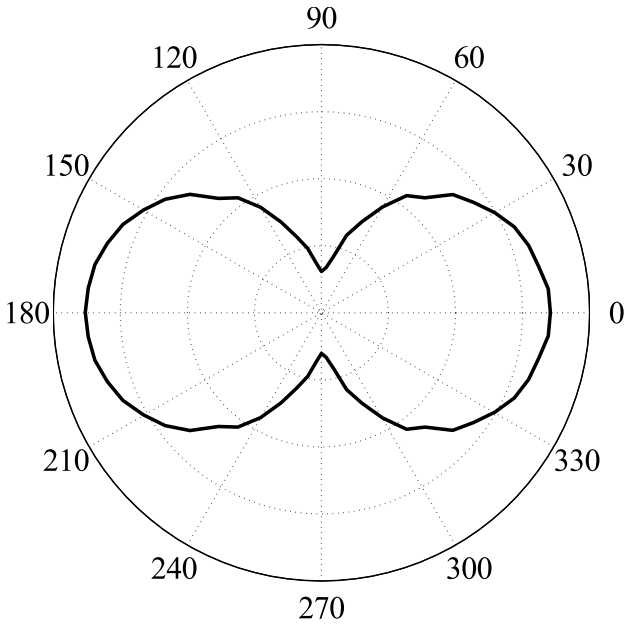

Figure 2.2.0.9: Polarization of the generated THz pulse. The horizontal axis between the 0 and 180 degree marks lies parallel to the dipole direction.

electric field is parallel to the oscillating dipole leaving $\sim$ 15% lying in the cross-polarized component.

As a final note to this section the characteristics of the electromagnet will be discussed. The electromagnet has an adjustable gap which is typically set to be 3 cm wide to accommodate the sample and THz beam. At this separation a uniform magnetic field is generated across the entire sample. Although the power supply can provide enough current to generate fields in excess of 1.0 T, the coils quickly heat up and and the field strength steadily decreases. The present cooling configuration for the coils is only capable of maintaining a constant field strength up to 0.5 T, above which performance begins to degrade. Because the acquisition of a single THz waveform takes 2 - 4 minutes, measurements involving the electromagnet are only done up to and including 0.5 T to avoid issues with the field strength changing over the course of a measurement.

2.3 MATLAB GUI for System Control

As was mentioned in the previous section, to acquire the full time-domain THz waveform the delay line must be scanned while recording the voltage signal from the lock-in amplifier. To accomplish this task a graphical user interface (GUI) was created using MATLAB. Its essential task is to step the stepper motor, wait for the output of the lock-in to stabilize, read the value of that output into an array, repeat for the desired number of steps and then move the delay stage back to its starting position. A screenshot of this GUI is shown in Figure 2.3.0.10 and a description of the available fields are as follows:

System Specifies which delay line to use. "Magnet" corresponds to the THz-TDS system outlined above while "Two Pulse/360 Deg." corresponds to

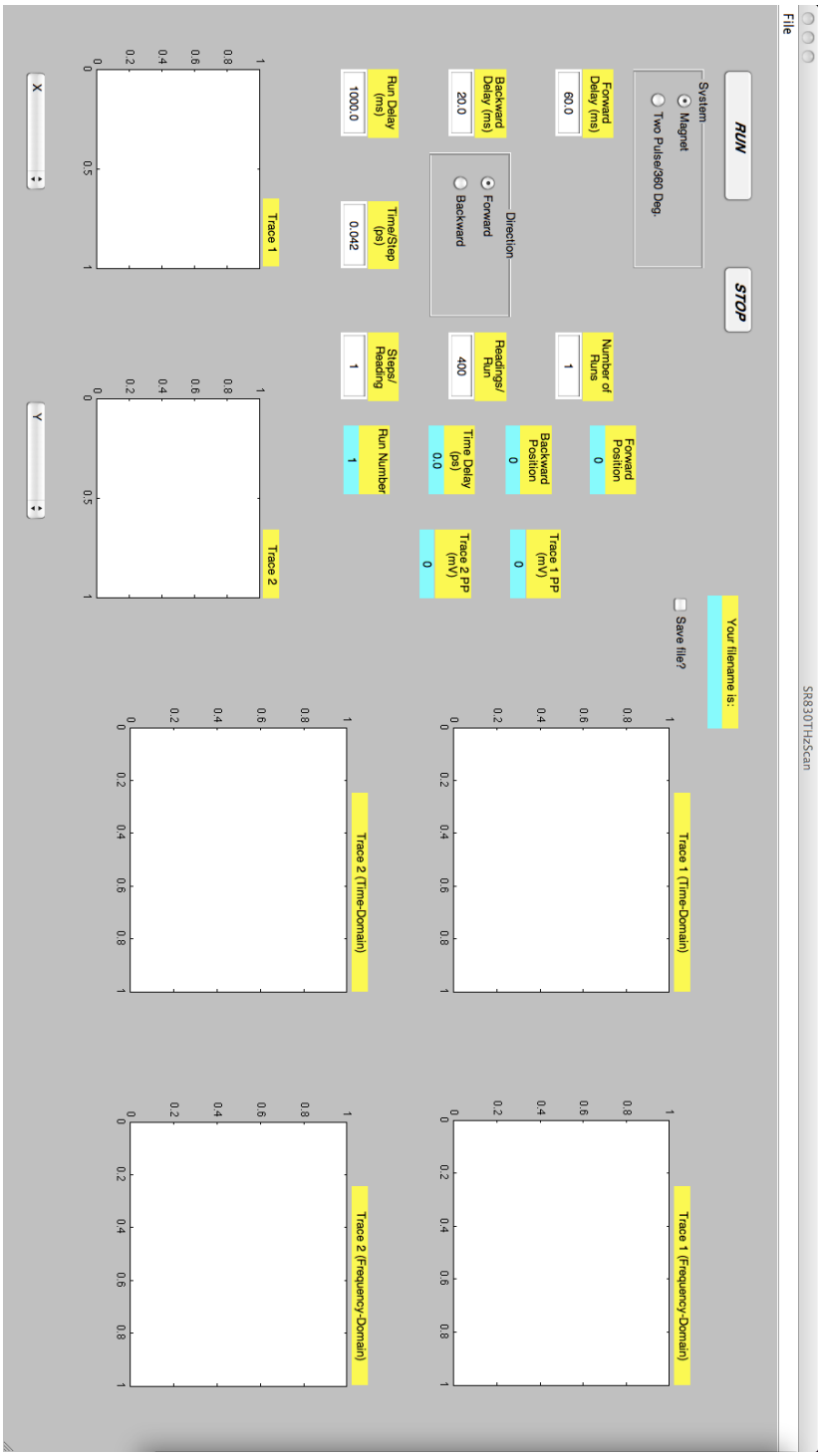

Figure 2.3.0.10: Screenshot of the MATLAB GUI used to control measurements with the THz-TDS system.

a different system.

Forward Delay (ms) Specifies how long the program should wait for the output of the lock-in amplifier to stabilize before stepping the stepper motor.

Backward Delay (ms) Specifies how long the program should wait between steps while moving the delay line back to its starting point.

Run Delay (ms) Specifies how long the program should wait between consecutive runs to begin data acquisition.

Direction Specifies the direction the delay stage should be scanned.

Time/Step (ps) Specifies the temporal resolution of each step of the stepper motor. This also corresponds to the sampling frequency of the system.

Number of Runs Specifies the number of consecutive runs the acquired data should be averaged over.

Readings/Run Specifies how many times the stepper motor should be stepped for a given run.

Steps/Reading Specifies how many steps the stepper motor should take before the output of the lock-in is read.

Forward Position Provides the real time relative forward position of the stepper motor.

Backward Position Provides the real time relative backward position of the stepper motor.

Time Delay (ps) Provides the real time relative time delay introduced to the beam path.

Run Number Provides the number of the current run out of the total "Number of Runs".

Trace 1 PP (mV) Provides the peak-to-peak voltage of the signal acquired from Channel 1 of the lock-in.

Trace 2 PP (mV) Provides the peak-to-peak voltage of the signal acquired from Channel 2 of the lock-in.

Your filename is: Provides the name of the file that the acquired data will be saved in.

Save file? If checked, the program will save the acquired data in a file with the specified filename.

Trace 1 Displays the data acquired from Channel 1 of the lock-in in real time. The drop-down menu beneath this plot specifies what Channel 1 should record.

Trace 2 Displays the data acquired from Channel 2 of the lock-in in real time. The drop-down menu beneath this plot specifies what Channel 2 should record.

Trace 1 (Time-Domain) Displays the data acquired from Channel 1 of the lock-in.

Trace 1 (Frequency-Domain) Displays the amplitude spectrum of the data acquired from Channel 1 of the lock-in.

Trace 2 (Time-Domain) Displays the data acquired from Channel 2 of the lock-in.

Trace 2 (Frequency-Domain) Displays the amplitude spectrum of the data acquired from Channel 2 of the lock-in.

2.4 Conclusion

In conclusion, THz-TDS is an excellent candidate for the study and characterization of materials, both naturally occurring and artificially engineered. This spectroscopy technique provides both high resolution temporal characterization and sensitivity to polarization dependent phenomena, as well as direct access to the electric field vector of the THz radiation. Furthermore, the incorporation of a high field strength electromagnet into a conventional THz-TDS system opens up new possibilities for the study of materials and physical phenomena. A system meeting these expectations has been presented here along with a characterization of its performance.

Chapter 2 References

[1] D. Mittleman, *Sensing with Terahertz Radiation.* Berlin: Springer-Verlag, 2003.

[2] S. L. Dexheimer, *Terahertz Spectroscopy: Principles and Applications.* Boca Raton, FL: Taylor & Francis Group (CRC Press), 2008.

[3] B. B. Hu and M. C. Nuss, "Imaging with terahertz waves," *Opt. Lett.*, vol. 20, no. 16, pp. 1716–18, 1995.

[4] S. Hunsche, M. Koch, I. Brener, and M. C. Nuss, "THz near-field imaging," *Opt. Comm.*, vol. 150, pp. 22–6, 1998.

[5] D. Grischkowsky, S. Keiding, M. van Exter, and C. Fattinger, "Far-infrared time-domain spectroscopy with terahertz beams of dielectrics and semiconductors," *J. Opt. Soc. Am. B*, vol. 7, no. 10, pp. 2006–15, 1990.

[6] D. M. Mittleman, J. Cunningham, M. C. Nuss, and M. Geva, "Noncontact semiconductor wafer characterization with the terahertz Hall effect," *Appl. Phys. Lett.*, vol. 71, no. 1, pp. 16–8, 1997.

[7] K. P. H. Lui and F. A. Hegmann, "Ultrafast carrier relaxation in radiation-damaged silicon on sapphire studied by optical-pump-terahertz-probe experiments," *Appl. Phys. Lett.*, vol. 78, no. 22, pp. 3478–80, 2001.

[8] T.-I. Jeon and D. Grischkowsky, "Nature of Conduction in Doped Silicon," *Phys. Rev. Lett.*, vol. 78, no. 6, pp. 1106–9, 1997.

[9] K. Wang and D. M. Mittleman, "Metal wires for terahertz wave guiding," *Nature*, vol. 432, pp. 376–9, 2004.

[10] H.-T. Chen, W. J. Padilla, J. M. O. Zide, A. C. Gossard, A. J. Taylor, and R. D. Averitt, "Active terahertz metamaterial devices," *Nature*, vol. 444, pp. 597–600, 2006.

[11] M. Hangyo, M. Tani, and T. Nagashima, "Terahertz Time-Domain Spectroscopy of Solids: A Review," *Int. J. Infrared Milli.*, vol. 26, no. 12, pp. 1661–90, 2005.

[12] P. U. Jepsen, D. G. Cooke, and M. Koch, "Terahertz spectroscopy and imaging - Modern techniques and applications," *Laser Photonics Rev.*, vol. 5, no. 1, pp. 124–66, 2011.

[13] D. H. Auston, "Picosecond optoelectronic switching and gating in silicon," *Appl. Phys. Lett.*, vol. 26, no. 3, pp. 101–3, 1975.

[14] D. H. Auston, K. P. Cheung, and P. R. Smith, "Picosecond photoconducting hertzian dipoles," *Appl. Phys. Lett.*, vol. 45, no. 3, pp. 284–6, 1984.

[15] J. A. Valdmanis and G. Mourou, "Subpicosecond Electrooptic Sampling: Principles and Applications," *IEEE J. Quantum Electron.*, vol. 22, no. 1, pp. 69–78, 1986.

[16] B. H. Kolner and D. M. Bloom, "Electrooptic Sampling in GaAs Integrated Circuits," *IEEE J. Quantum Electron.*, vol. 22, no. 1, pp. 79–93, 1986.

[17] P. U. Jepsen, R. H. Jacobsen, and S. R. Keiding, "Generation and de-

tection of terahertz pulses from biased semiconductor antennas," *J. Opt. Soc. Am. B*, vol. 13, no. 11, pp. 2424–36, 1996.

[18] A. Yariv, *Quantum Electronics*. New York, NY: John Wiley & Sons, 1989.

[19] J. F. Holzman, "Ultrafast Photonic Applications for Terahertz Waveform Generation," Ph.D. dissertation, University of Alberta, 2003.

[20] P. C. M. Planken, H.-K. Nienhuys, H. J. Bakker, and T. Wenckebach, "Measurement and calculation of the orientation dependence of terahertz pulse detection in ZnTe," *J. Opt. Soc. Am. B*, vol. 18, no. 3, pp. 313–7, 2001.

[21] C. Spielmann, P. F. Curley, T. Brabec, and F. Krausz, "Ultrabroadband Femtosecond Lasers," *IEEE J. Quantum Electron.*, vol. 30, no. 4, pp. 1100–14, 1994.

[22] R. Szipöcs, K. Ferencz, C. Spielmann, and F. Krausz, "Chirped multilayer coatings for broadband dispersion control in femtosecond lasers," *Opt. Lett.*, vol. 19, no. 3, pp. 201–3, 1994.

[23] M. van Exter, C. Fattinger, and D. Grischkowsky, "Terahertz time-domain spectroscopy of water vapor," *Opt. Lett.*, vol. 14, no. 20, pp. 1128–30, 1989.

[24] R. T. Hall, D. Vrabec, and J. M. Dowling, "A High-Resolution, Far Infrared Double-Beam Lamellar Grating Interferometer," *Appl. Opt.*, vol. 5, no. 7, pp. 1147–58, 1966.

Chapter 3

Affects of Particle Size on Near-Field Particle Plasmon Coupling[1]

3.1 Background

The interaction of electromagnetic radiation with metallic media has received a significant amount of attention in the past century. From Drude's complex conductivity model [2] and the scattering theory developed by Mie [3] to more recent discoveries such as metamaterials [4], the electromagnetic response of metals offers a rich array of phenomena. Of particular interest is the interaction of light with subwavelength metallic structures, which is encompassed by the field of plasmonics. In the bulk regime, the intrinsic permittivity and permeability dictate the response of a medium, but as the subwavelength regime is approached the geometry and surface properties of the structure play a key role in defining the electromagnetic response. If momentum is conserved dur-

[1] A version of this chapter has been published in *Journal of Infrared, Millimeter, and Terahertz Waves* [1].

ing the interaction, surface plasmon modes can be excited, which can greatly affect the response of a subwavelength structure to incident electromagnetic radiation.

In 2005, Chau et al. [5] demonstrated an interesting phenomenon where THz radiation was coherently transported through dense ensembles of subwavelength metallic microparticles. It was found that the mechanism responsible for the apparent transparency of the particle ensemble was near-field mediated coupling of non-resonant localized plasmon modes excited by the incident THz electric field. Extraordinarily, this mechanism coherently transports a significant portion of the incident electromagnetic energy over sample thicknesses which exceed the absorption skin depth of the constituent metal by up to *five* orders of magnitude. In a follow-up study, Chau and Elezzabi [6] further determined the effects of particle shape and conductivity on the transparency of the ensemble. Interestingly, from this study it was shown that the near-field coupling mechanism was very sensitive to both of these parameters.

A simplified representation of the near-field coupling of particle plasmon modes is given in Figure 3.1.0.1. At THz frequencies between 0.1 and 1.4 THz, the conductivity of metals is very large, lying in the range of $10^6 - 10^7\ \Omega^{-1}$ such that the absorption skin depth is on the order of ~ 100 nm (see Appendix B). This means that the current density induced by a THz electromagnetic wave impinging on a subwavelength metallic sphere is dictated by Ohm's law and exists very close to the surface of the sphere. Therefore, this current density will be very sensitive to both the surface structure and conductivity of a subwavelength particle. Moreover, the current density is the result of an oscillating dipolar charge distribution, or dipole moment, such that depolarization field of the particle resembles that of a radiating dipole. When an ensemble of particles is present, it is this depolarization field that couples to adjacent

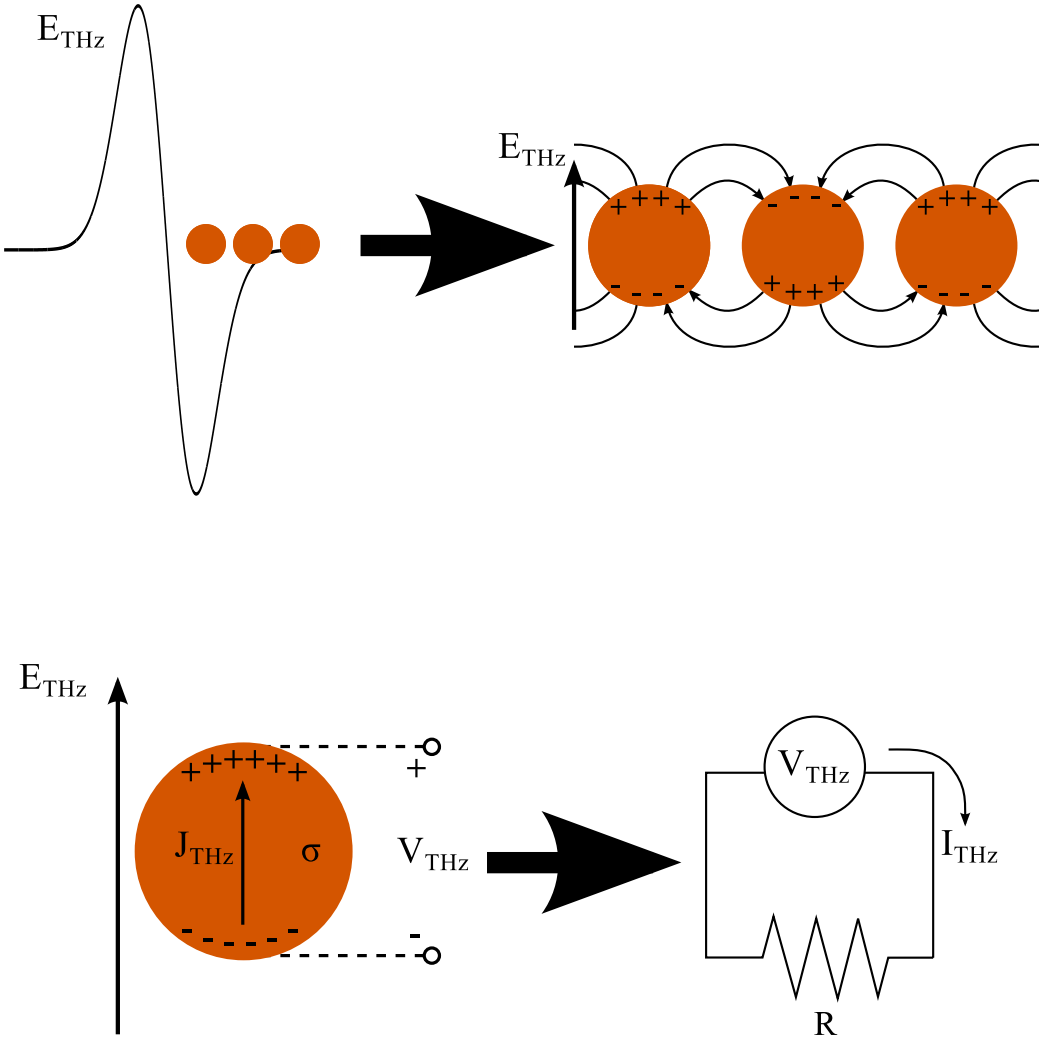

Figure 3.1.0.1: Top: Cartoon illustration of near-field particle plasmon coupling. The incident THz electric field induces a localized surface plasmon mode which subsequently radiates like a dipole. The radiated electric field then couples to an adjacent particle in the near-field and the process repeats. Bottom: Circuit analogy of the interaction between the THz electric field and a subwavelength metallic particle. The particle is represented by a resistor, R, and the current-voltage relationship is dictated by Ohm's law.

particles in the near-field, effectively transporting the THz electromagnetic radiation through the ensemble.

It is important to note that Bruggeman's effective medium theory (EMT) [7, 8] is typically utilized when describing the permittivity and permeability of a homogenized random medium. This theory describes the electromagnetic response of the medium by defining an effective permittivity and permeability as the weighted average of the individual particle's permittivity and permeability. However, this theory is valid only for the situation where the polarization within the particles is uniform, which is the case for nanoscale particles since the mean dimension is less than the absorption skin depth of the incident radiation. This condition is not satisfied in the THz regime, and EMT does not capture the essence of the electromagnetic interactions between adjacent particles. Here, near-field coupling of the particles' dipolar responses must be considered.

This chapter discusses the effects of particle size on the transparency of a metallic particle ensemble to incident THz electromagnetic radiation. In particular, the near-field coupling mechanism responsible for the apparent transparency of such an ensemble is discussed in terms of the depolarization electric field pattern and the peak wavelength transmitted through the ensemble. THz-TDS is used to study the transparency of a series of metallic particle ensembles having mean particle diameters ranging from 68 ± 2 µm to 654 ± 10 µm. In addition, two-dimensional (2D) finite-difference time-domain (FDTD) simulations are performed on single particles of varying diameter to determine the depolarization electric field pattern.

3.2 Experimental Methods

The eight particle ensembles used in this experiment consist of close-packed, randomly distributed Cu microparticles having different mean diameters, δ. Figure 3.2.0.2 gives scanning electron microscope (SEM) images of the eight samples under study. Note that the mean particle diameter and its standard

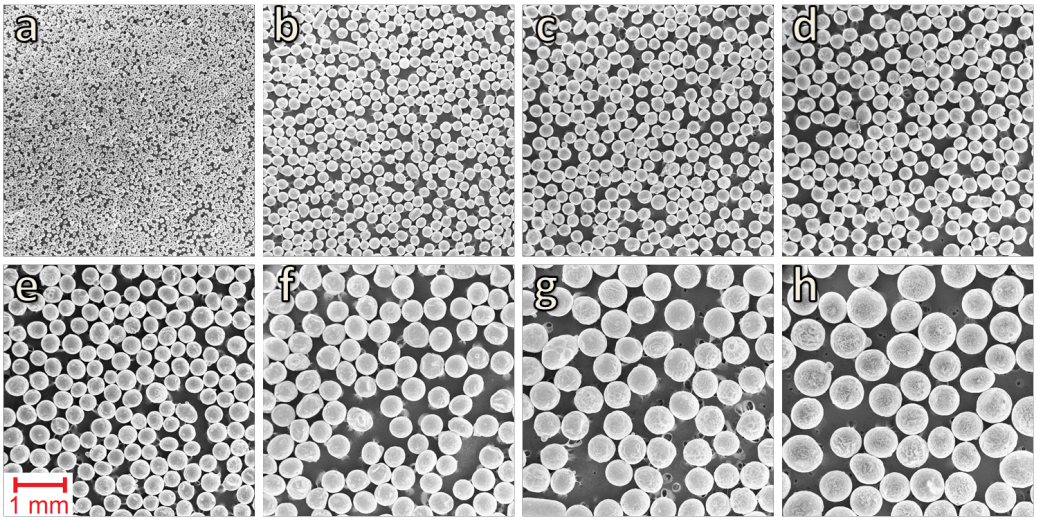

Figure 3.2.0.2: Scanning electron microscope images of Cu particles samples. Note that the particles are spatially dispersed for imaging purposes only. (a) $\delta = 68 \pm 2$ µm, (b) $\delta = 182 \pm 3$ µm, (c) $\delta = 243 \pm 3$ µm, (d) $\delta = 273 \pm 3$ µm, (e) $\delta = 335 \pm 7$ µm, (f) $\delta = 435 \pm 5$ µm, (g) $\delta = 526 \pm 4$ µm and (h) $\delta = 654 \pm 10$ µm

error for each sample are calculated by measuring the diameters of a random sampling of 30 particles. To prepare each sample for study, a polystyrene sample holder 4 mm thick and 12 mm wide was filled with Cu particles in such a way as to keep the packing fraction practically constant between samples, which fell within the range of 0.52 ± 0.06 to 0.54 ± 0.06.

THz radiation was generated via PC switching by 800 nm, $\sim$ 10 fs pulses from a Ti:Sapphire laser oscillator incident on a biased coplanar strip line fabricated on a semi-insulating GaAs substrate. This resulted in single-cycle, $\sim$ 1 ps THz pulses having a center frequency of 0.6 THz and a bandwidth of 0.5 THz. The generated radiation was collected and focused onto the sample

via a pair of 5 cm focal length off-axis, gold-coated parabolic mirrors. An identical pair of parabolic mirrors were then used to pass the transmitted THz radiation to the detection setup, which employed a 0.5 mm thick <111> ZnSe EO crystal to detect the time-domain waveforms. The system is identical to that used in [9].

The transparency of each sample was studied in an identical fashion. The transmitted THz waveform was detected for two different points of incidence on the sample to ensure constancy of the packing fraction throughout. The sample holder was then emptied and refilled to promote true randomness of the particles. Again, the transmitted THz waveform was detected for two different points of incidence on the sample; and, therefore, a total of four time-domain waveforms were averaged for each sample to obtain the results.

3.3 Results and Discussion

The time-domain waveforms and corresponding power spectra of the THz radiation transmitted through each sample are depicted in Figure 3.3.0.3. As δ increases the transmitted THz waveform becomes strongly attenuated and dispersed due to a loss of the higher frequency components to scattering and absorption. The total transmitted power of the THz pulse decreases by 96% for $\delta = 68$ µm and 99% for $\delta = 654$ µm when compared to the freespace waveform. As the particle diameter increases only those wavelengths for which the particle is still considered subwavelength induce a sufficient dipolar response such that the incident radiation can be effectively transported through the ensemble. This fact is corroborated by the loss of shorter wavelengths in the transmitted power spectra. Figure 3.3.0.4 shows the normalized total power and peak wavelength of the THz radiation transmitted through each ensemble.

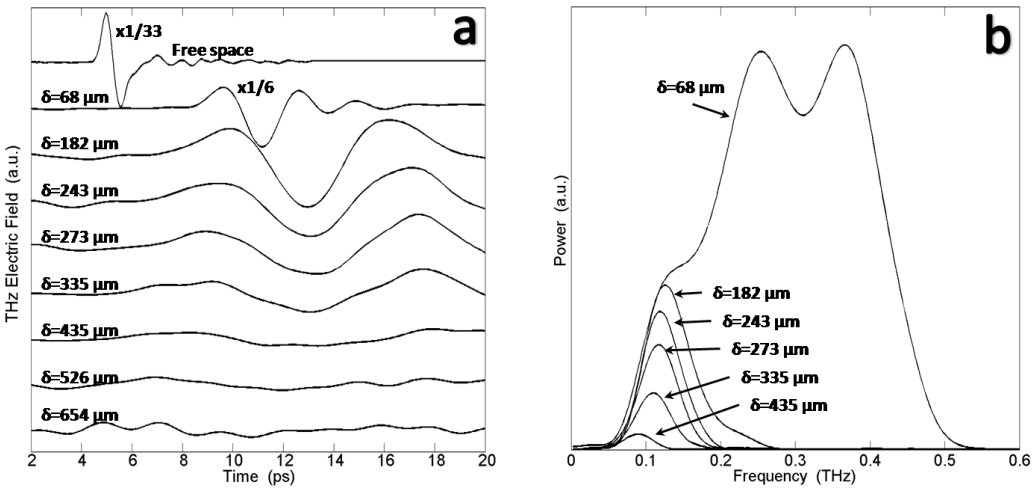

Figure 3.3.0.3: (a) Time-domain waveforms of the THz radiation transmitted through each sample and (b) their corresponding power spectra. The broad spectral peaks for the $\delta = 68$ μm sample at 0.25 and 0.37 THz arise due to the interparticle geometry.

The total power transmitted through each sample shows a decaying exponential relationship, decreasing as δ increases. This decrease can be attributed to the inability of higher frequency components (shorter wavelengths) of the incident THz pulse to excite localized surface plasmon modes on the particles. Thus, the incident field cannot couple to the ensemble such that it is not transmitted; instead, it is reflected upon incidence. As expected, the peak wavelength of the transmitted THz radiation shifts to longer wavelengths as δ increases due to the loss of the higher frequency components.

To further corroborate the above discussion 2D FDTD[2] simulations are performed on particles of different mean diameters. Here, a single particle is excited by a broadband THz pulse similar to that produced by the experimental THz-TDS system, and the electric field pattern in the particle's vicinity is monitored. Figure 3.3.0.5 depicts the results of these simulations for a series of particles. For $\delta = 50$ μm and $\delta = 100$ μm, the electric field shows a clear dipole-like distribution in the vicinity of the particle as a result of an induced

[2]The 2D FDTD code used here was written by Kenneth Chau.

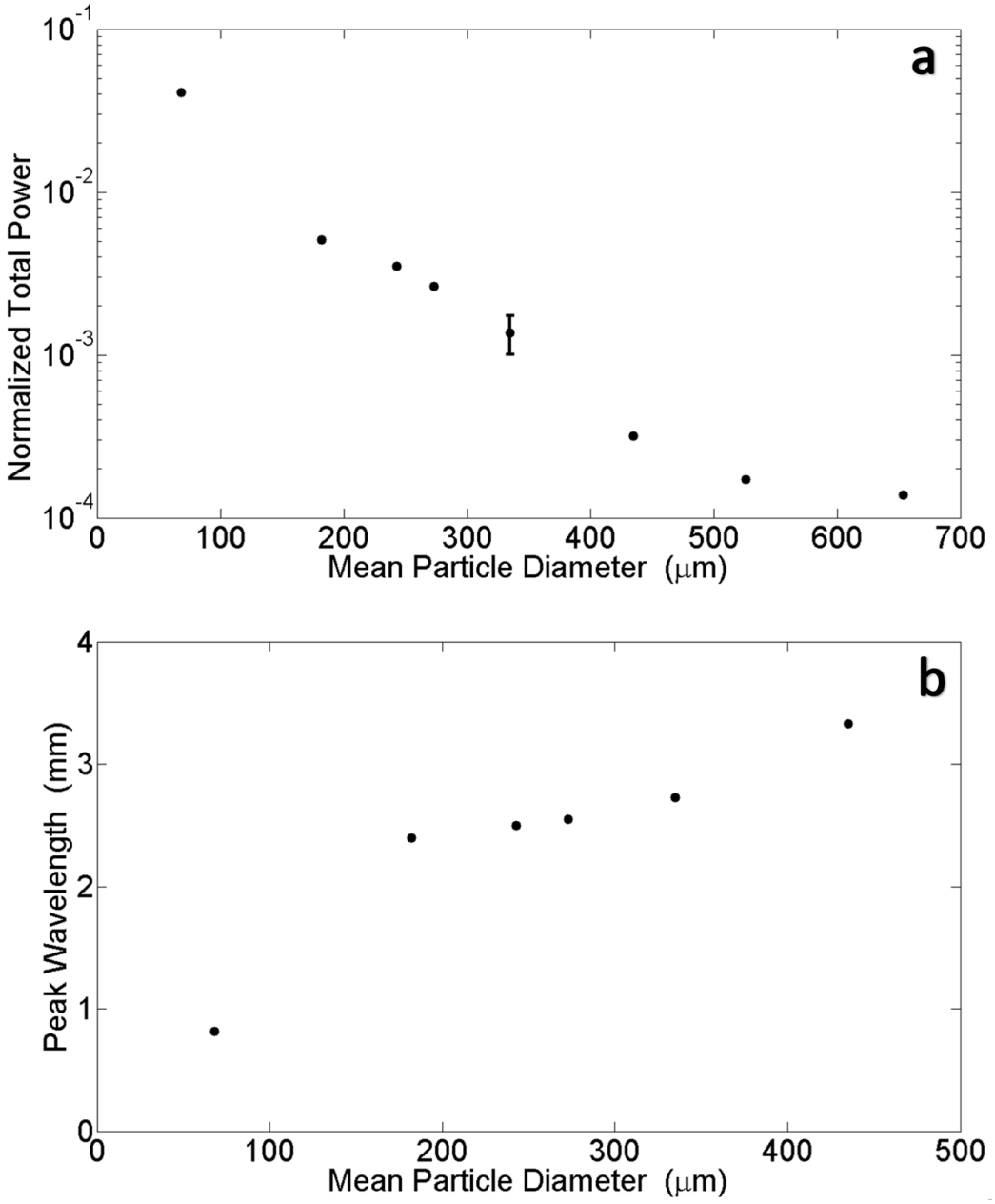

Figure 3.3.0.4: (a) Total power of the transmitted THz radiation for each sample normalized to the freespace waveform. The respresentative error bar applies to all data points. (b) Peak wavelength of the transmitted THz radiation for each sample.

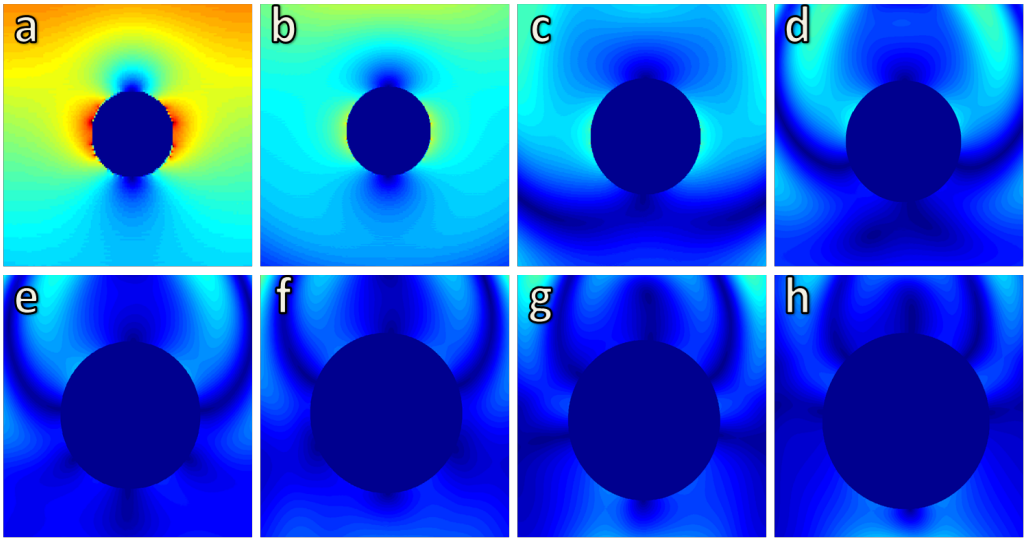

Figure 3.3.0.5: FDTD simulations of single particles showing electric field patterns in the vicinity of the particle. The polarization of the incident wave is from left to right. Dark red represents the greatest field magnitude while dark blue represents the lowest field magnitude. (a) $\delta = 50$ µm, (b) $\delta = 100$ µm, (c) $\delta = 200$ µm, (d) $\delta = 300$ µm, (e) $\delta = 400$ µm, (f) $\delta = 500$ µm, (g) $\delta = 600$ µm and (h) $\delta = 700$ µm.

localized surface plasmon mode. However, as δ increases beyond 100 µm the electric field distribution begins to resemble that of a multipole as a result of degradation of the particle's polarizability. This results in an increase in the amount of incident radiation reflected by the particle. Thus, the transparency of an ensemble of large particles ($\delta > 100$ µm) is reduced due to the poor coupling between adjacent particles (a result of multipolar field distributions) as well as an increase in radiation reflected upon incidence. Essentially, the electromagnetic response of an ensemble of large particles approaches that of a bulk metal.

3.4 Conclusion

In conclusion, the transparency of a metallic particle ensemble to incident THz electromagnetic radiation was studied as a function of the mean diameter of the constituent particles. This was accomplished through the excitation of localized surface plasmon modes on the particles, which lead to coherent transmission of the incident THz radiation through the ensemble. It was found that the ensemble transparency decreased as the mean particle diameter increased. This was attributed to the degradation of the particle's polarizability leading to an increase in scattering and a decrease in energy transport through the ensemble. From this study an upper bound of $\delta \sim 100$ µm was established for efficient transport of THz radiation through a dense ensemble of such particles.

Chapter 3 References

[1] C. J. E. Straatsma, M. A. Startsev, and A. Y. Elezzabi, "An Investigation of Terahertz Particle Plasmons: Affect of Particle Size on the Transparency of a Metallic Particle Ensemble," *J. Infrared Millim. Te.*, vol. 31, pp. 659–666, 2010.

[2] N. W. Ashcroft and N. D. Mermin, *Solid State Physics*. Orlando, FL: Harcourt, 1976.

[3] H. C. van de Hulst, *Light Scattering by Small Particles*. Mineola, NY: Dover Publications, 1981.

[4] N. Engheta and R. W. Ziolkowski, *Metamaterials: Physics and Engineering Explorations*. New York, NY: John Wiley & Sons, 2006.

[5] K. J. Chau, G. D. Dice, and A. Y. Elezzabi, "Coherent Plasmonic Enhanced Terahertz Transmission through Random Metallic Media," *Phys. Rev. Lett.*, vol. 94, no. 17, pp. 173 904/1–4, 2005.

[6] K. J. Chau and A. Y. Elezzabi, "Terahertz transmission through ensembles of subwavelength-size metallic particles," *Phys. Rev. B*, vol. 72, no. 7, pp. 075 110/1–9, 2005.

[7] T. C. Choy, *Effective Medium Theory: Principles and Applications*. Oxford, NY: Oxford University Press, 1999.

[8] G. W. Milton, *The Theory of Composites*. Cambridge: Cambridge University Press, 2002.

[9] A. Y. Elezzabi and S. Sederberg, "Optical activity in an artificial chiral media: a terahertz time-domain investigation of Karl F. Lindsman's 1920 pioneering experiment," *Opt. Exp.*, vol. 17, no. 8, pp. 6600–12, 2009.

Chapter 4

Investigation of Terahertz Photonic Giant Magnetoresistance

4.1 Background

In 2006, Chau and Elezzabi successfully demonstrated a photonic analogous AMR effect at THz frequencies [1]. Here, the transparency of a ferromagnetic metallic particle ensemble to incident THz radiation was studied under the influence of an applied magnetic field. It was found that the resistivity modulation caused by the applied field corresponded to a decrease in transparency of the ensemble, and also that this reduction was dependent on the orientation of the applied field. Following this work, Chau et al. [2] also demonstrated THz induced spin injection and accumulation at a ferromagnetic/non-magnetic metallic junction. Once again, the transparency of a metallic particle ensemble was studied under the influence of an applied magnetic field. In this study, however, ferromagnetic particles were coated with a non-magnetic thin film

using sputter deposition and magnetic field dependent attenuation was observed. Furthermore, the authors were able to experimentally determine a lower bound to the spin diffusion length in Au.

The real significance of the preliminary work done by Chau et al. lies in the fact that it provides evidence that traditional spin-dependent transport mechanisms can be utilized for the development of active THz components. It is important to note the pioneering work on these transport mechanisms that revolutionized the electronics industry. It began with the work of Julliere [3], giving rise to the magnetic tunnel junction and prompting a surge of research interest in this field. Further understanding of the mechanisms behind electron-spin-dependent transport came with Johnson and Silsbee's detailed study of spin injection and accumulation across a ferromagnetic/paramagnetic interface [4–7]. This work provided fundamental knowledge regarding the coherence length of spin polarized electrons travelling inside a non-ferromagnetic medium. Shortly after this work, Fert [8] and Grünberg [9] demonstrated the GMR effect, which would later win the Nobel Prize in Physics due to its technological applications. The introduction of electron-spin sensitive devices eventually gave rise to modern day high density computer hard drive technology since it allowed for an increase in available storage while miniaturizing the footprint of the components. It has also lead to the postulation and implementation of other technologies such as magnetoresistive random-access memory [10].

Observing the progression of electrical based spin transport mechanisms, the logical step following the work of Chau et al. is the investigation of a photonic analogous GMR effect. Due to the nature of the interaction of THz radiation with subwavelength metallic microparticles, ensembles of these particles can be used a platform for studying the effects of material junctions

on localized particle plasmons at THz frequencies. Thus far, the effect of a spin-based junction between ferromagnetic and non-magnetic materials [2] as well as a semiconductor-metal junction [11] have been studied in this manner. Therefore, it is, in principle, possible to study the effect of a GMR multilayer on the transparency of a metallic particle ensemble in this same way. Based on this fact the following section outlines experiments designed to accomplish this task.

4.2 Sample Preparation

As was discussed in Chapter 1, the interaction of a time-harmonic electric field with a subwavelength metallic particle induces an oscillating dipole moment resultant from the motion of free charge within the particle skin depth. At THz frequencies, the skin depth is much less than the diameter of a subwavelength particle such that the induced current exists only at the surface of the particle. Furthermore, due to the large imaginary electric permittivity (large conductivity) of metals in this frequency range, the current is dictated by Ohm's law. From these facts two conclusions can be drawn: the current will be sensitive to both the (1) conductivity and (2) surface structure of the particle. Therefore, deposition of a GMR multilayer onto the particle surface should provide a means to actively control its interaction with THz radiation.

In the original design of this experiment, Baron provided some key points regarding the specific GMR configuration to be used for the multilayer [12]. The spin-valve configuration, which utilizes an antiferromagnetically pinned layer having a magnetization direction determined at the time of fabrication, is a poor choice due to the random orientation of the particles during the experiment. In other words, unless the orientation of the pinned layer mag-

netization is along that of the applied field a minimal effect will be observed. This means that only a portion of the ensemble will contribute to the overall resistivity modulation experienced by the THz radiation, which is undesirable. The pseudo-spin-valve configuration, however, does not suffer from these drawbacks since the magnetization direction of the layers is not predetermined. It is because of this that Baron chose the pseudo-spin-valve configuration for his study. Finally, the exchange coupled configuration is a possibility if care is taken in the design of the multilayer structure such that the required magnetic field strength to switch the magnetization of the layers is kept to a reasonable value (< 0.5 T).

To study this phenomenon, samples consisting of an ensemble of Cu microparticles having a mean diameter of 90 ± 15 µm are partially coated with different GMR multilayer configurations. The coating was done via off-axis, radio frequency sputter deposition, which was performed by Mohamed El Sayed who is a member of Prof. Jan A. Jung and Prof. Kim H. Chow's research group in the Department of Physics at the University of Alberta. A cartoon representation of the end result of this process is depicted in Figure 4.2.0.1. The samples under study here are listed in Table 4.1, where the values in brackets adjacent to the material name are the corresponding layer thickness in nm. The three samples described here are similar to the those studied by

Sample Number	Configuration
1	Cu(200)/Py(3)/Co(3)/Cu(2)/Co(3)
2	Cu(200)/Py(3)/Co(3)/Cu(2)/Co(2)/Cu(2)/Co(3)
3	Cu(200)/Py(3)/Co(3)/Cu(2)/Co(2)/Cu(2)/Co(3)/Py(3)

Table 4.1: Composition of the GMR multilayers deposited on Cu microparticles. Py corresponds to permalloy, which is a $Ni_{0.8}Fe_{0.2}$ alloy. The order of the materials corresponds to the order of deposition when read from left to right. The values listed in brackets adjacent to the element name is the film thickness in nm.

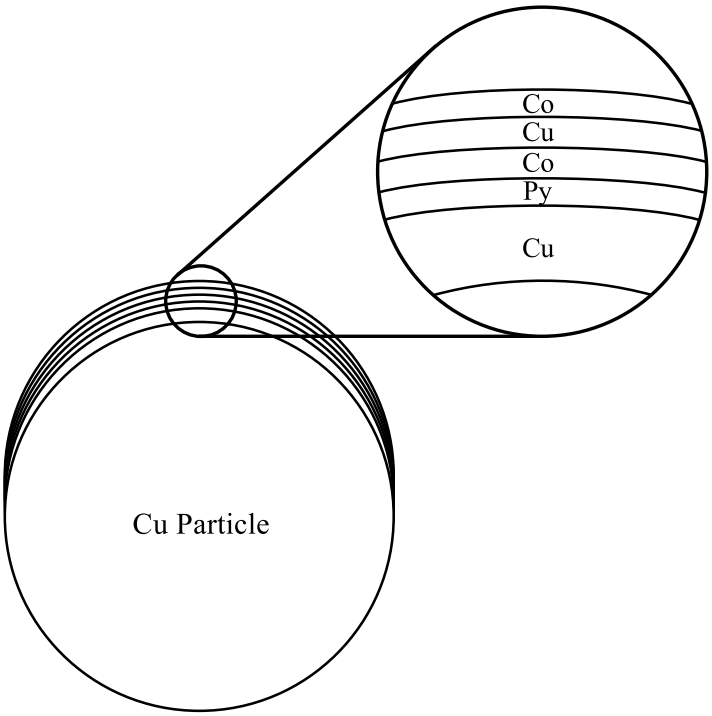

Figure 4.2.0.1: Cartoon representation of a Cu particle with a GMR multilayer deposited on its surface. The layer thicknesses are exaggerated for clarity. Note that only a portion of the particle gets covered during the deposition process.

Baron [12] in their utilization of Py and Co as the ferromagnetic layers, but are based upon the extensive work done by Hütten et al. [13]. The initial 200 nm layer of Cu is first deposited to isolate the effects of the native oxide layer present on the surface of the Cu particles [11]. A Py buffer layer is then deposited to aid the formation of smooth interfaces between the subsequent layers. The combination of Py and Co in the first ferromagnetic layer make it magnetically soft in comparison to a pure Co layer. Therefore, the structures under study are expected to exhibit aspects from both the pseudo-spin-valve and exchange coupled GMR configurations, particularly in the shape of their resistance change curves. This fact is shown well in [13] for planar GMR multilayers.

4.3 Results and Discussion

The experimental THz-TDS system used for this section is documented in [14]. Its functionality is identical to the one described in Chapter 2 except that it does not include an electromagnet. Instead, a compact, variable magnetic field strength system based on permanent magnets was designed and constructed (see Appendix A) for this portion of the thesis work. To detect resistivity changes in the particles caused by GMR, the transmission of THz radiation through 3 mm thick ensembles of the samples described in Table 4.1 is analyzed under the influence of an applied magnetic field. The magnetic field is applied perpendicular to the polarization of the incident THz electric field and is cycled between its maximum and minimum value a few times prior to data collection. Because the samples are prepared in the exchange coupled configuration, it is expected that initially the GMR multilayer will be in a high resistance state as a result of antiferromagnetic coupling between the two

ferromagnetic layers. This correlates with a reduced transparency of the sample leading to less transmission of the incident THz radiation. As a magnetic field is applied the magnetization of the ferromagnetic layers should align and the multilayer will enter into a low resistance state resulting in higher transmission of the THz radiation. Therefore, the transmission will be inversely proportional to the resistance change of the sample.

In all cases, the THz transmission through the sample is recorded for magnetic field strengths between 50 and 450 mT. The field is first increased from minimum to maximum strength and then subsequently decreased back to minimum strength. In this way any hysteresis associated with the resistance change can be observed. Figure 4.3.0.2 shows the transmitted THz waveform through samples 1 and 2 for applied fields of 0 and 450 mT. From these waveforms it is readily apparent that there is no observable change above the noise floor in the transparency of either sample caused by an applied magnetic field. This is the case for all applied field strengths between 50 and 450 mT. Based on the results presented in [13], the expected resistance change for a planar version of the GMR multilayer used for samples 1 and 2 is $\sim 10\%$. It is possible that the lack of change in transparency observed for these samples is a result of either the resistance change being too small or that the random orientation of the multilayers with respect to the applied magnetic field and incident THz electric field reduces the net effect. For this reason sample 3 was fabricated. A planar version of this sample has an expected resistance change of $\sim 18\%$ according to [13]. Figure 4.3.0.3 shows the total power contained in the THz waveform transmitted through sample 3 as a function of the applied magnetic field strength. A change of $\sim 15\%$ in transparency of the sample is clearly noticeable from the increase in transmitted power as the magnetic field strength is increased. As discussed before, the sample is assumed to transi-

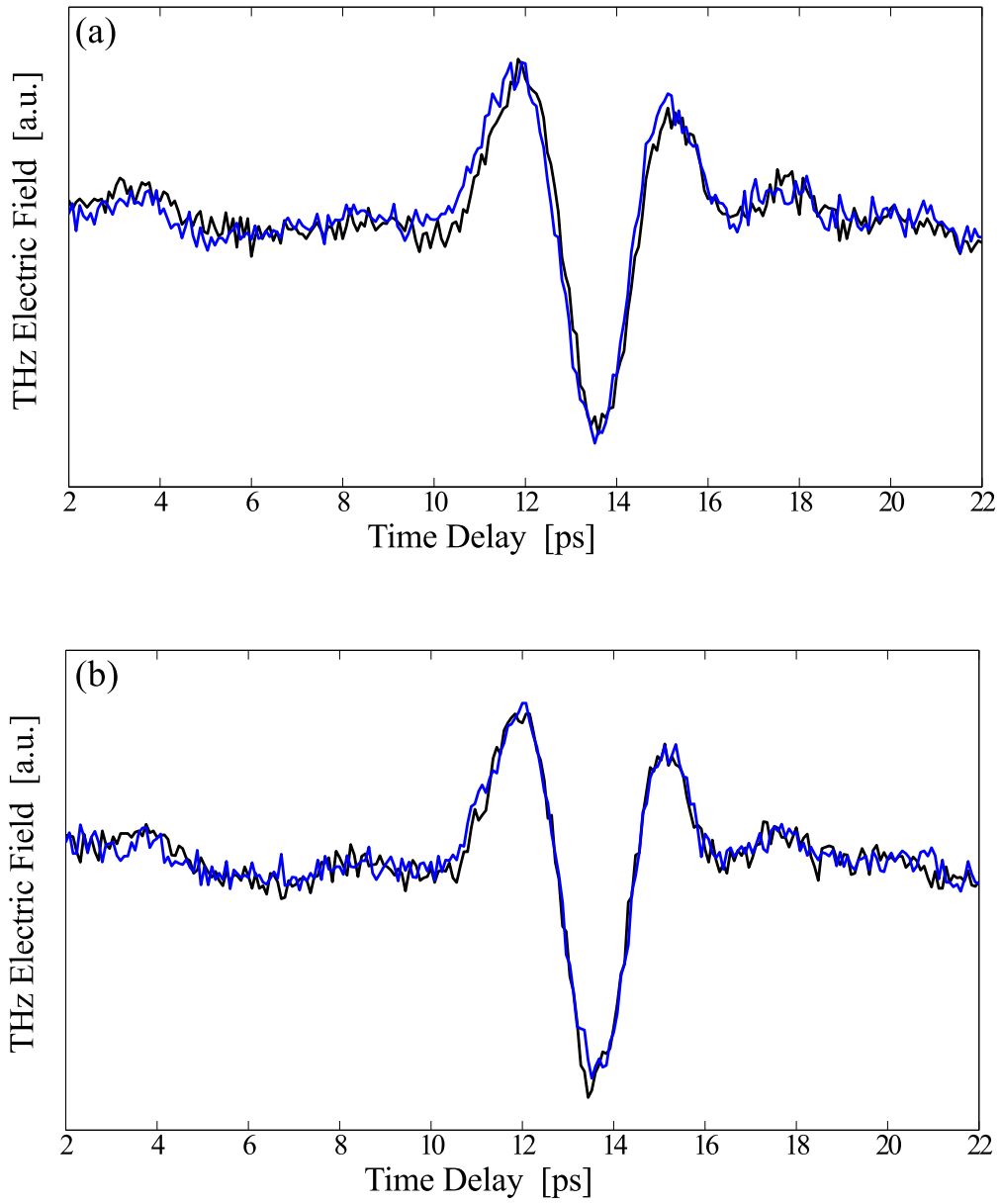

Figure 4.3.0.2: THz time-domain waveforms of the transmitted radiation through samples (a) 1 and (b) 2. The black curves correspond to an applied field of 50 mT while the blue curves correspond to a field of 450 mT.

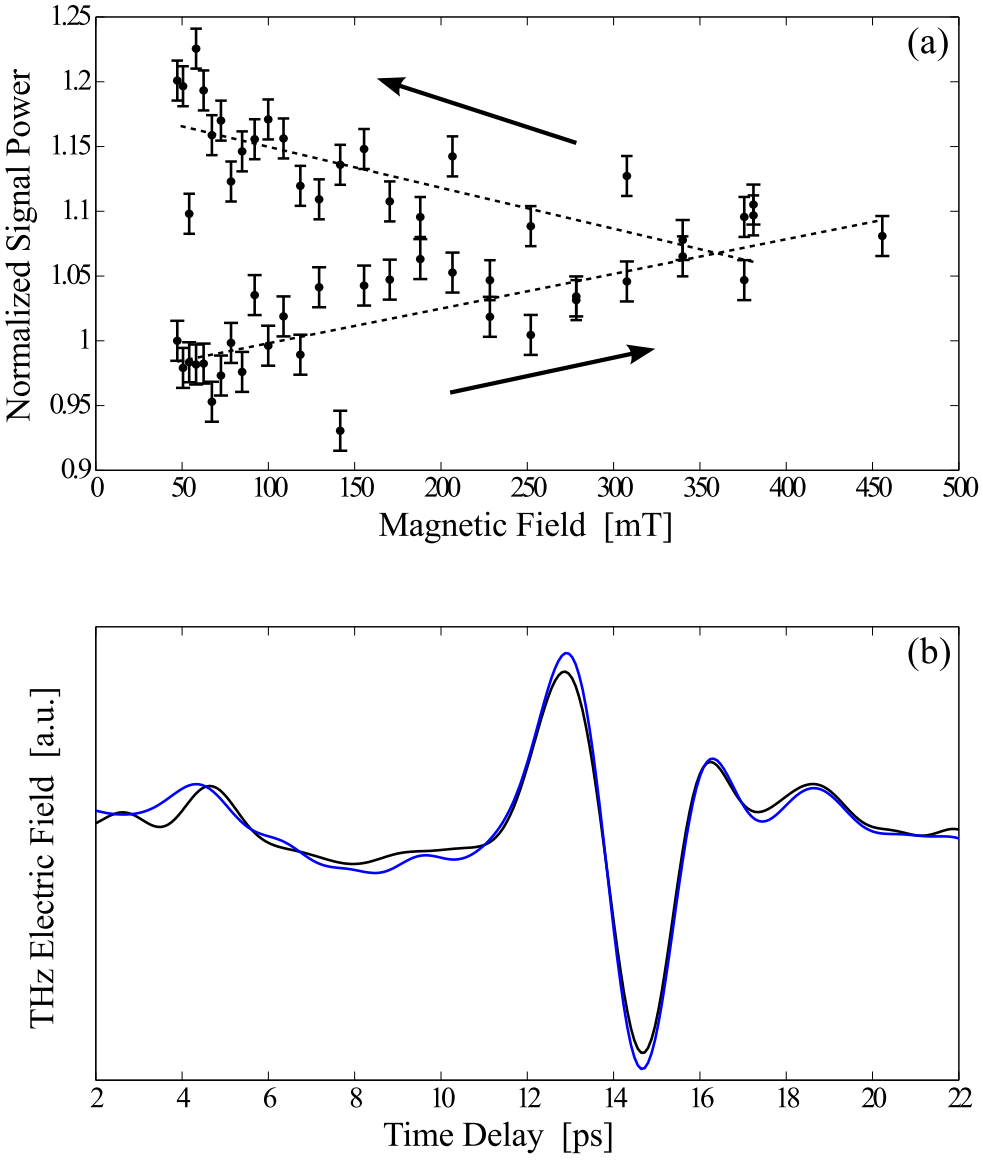

Figure 4.3.0.3: (a) Total THz signal power transmitted through sample 3 versus applied magnetic field strength. The arrows indicate the direction of the magnetic field sweep, and the dashed lines are provided to guide the eye. Note that the data points are normalized to that initially acquired at a field strength of 50 mT. (b) THz time-domain waveforms for the initial and final data points at a magnetic field of 50 mT. The black curve corresponds to the initial data point while the blue curve corresponds to the final data point. A low-pass filter has been applied to these waveforms to better show the difference in amplitude.

tion from a state of high resistance to one of low resistance as the magnetic field strength is increased. This correlates with an increase in the radiation transmitted through the sample, which is corroborated by the results shown in Figure 4.3.0.3. The continued increase of the transmitted radiation upon reducing the magnetic field strength back to its minimum value is indicative of not reaching a state of saturation. This implies cycling within a minor loop of the system, which is supported qualitatively by the results depicted in [13].

Before concluding it is pertinent to discuss the nature of the "substrate" used here for deposition of the GMR multilayers. Typically, these multilayer structures are deposited on polished silicon or glass such that film interfaces and thicknesses are very uniform. This is crucial to their performance considering how sensitive the GMR effect is to both the substrate quality and growth parameters (see [15] or [16] for example). Here, however, polished silicon or glass is replaced by comparatively rough Cu microparticles exhibiting a surface roughness on the order of ~ 1 µm. It is expected that this will degrade the performance of the GMR multilayers, which results in the need for a structure which exhibits a large change in resistance to influence the transparency of the particle ensemble. This helps explain why only sample 3 exhibited any change in transparency with the application of a magnetic field.

4.4 Conclusion

This portion of the thesis work focused on studying the GMR effect as a candidate for active control of THz radiation confined to subwavelength metallic particles. It was shown that an ensemble of Cu microparticles partially coated with a GMR multilayer shows a magnetic field dependent transparency to an incident THz electromagnetic wave. As such, it appears promising that the

GMR effect could open up a realm of possibilities for active THz components. However, the results shown here are preliminary and must be improved upon, particularly in terms of the experimental setup. It was for this reason, among others, that the system outlined in Chapter 2 was constructed. Thus far, only a couple of these GMR experiments have been performed on the new system, but no further results are available at this time.

Chapter 4 References

[1] K. J. Chau and A. Y. Elezzabi, "Photonic Anisotropic Magnetoresistance in Dense Co Particle Ensembles," *Phys. Rev. Lett.*, vol. 96, no. 3, pp. 033 903/1–4, 2006.

[2] K. J. Chau, M. Johnson, and A. Y. Elezzabi, "Electron-Spin-Dependent Terahertz Light Transport in Spintronic-Plasmonic Media," *Phys. Rev. Lett.*, vol. 98, no. 13, pp. 133 901/1–4, 2007.

[3] M. Julliere, "Tunneling Between Ferromagnetic Films," *Phys. Lett.*, vol. 54A, no. 3, pp. 225–6, 1975.

[4] M. Johnson and R. H. Silsbee, "Interfacial Charge-Spin Coupling: Injection and Detection of Spin Magnetization in Metals," *Phys. Rev. Lett.*, vol. 55, no. 17, pp. 1790–3, 1985.

[5] ——, "Thermodynamic analysis of interfacial transport and of the thermomagnetoelectric system," *Phys. Rev. B*, vol. 35, no. 10, pp. 4959–72, 1987.

[6] ——, "Coupling of electronic charge and spin at a ferromagnetic-paramagnetic metal interface," *Phys. Rev. B*, vol. 37, no. 10, pp. 5312–25, 1988.

[7] ——, "Spin-injection experiment," *Phys. Rev. B*, vol. 37, no. 10, pp. 5326–35, 1988.

[8] M. N. Baibich, J. M. Broto, A. Fert, F. N. V. Dau, F. Petroff, P. Eitenne, G. Creuzet, A. Friederich, and J. Chazelas, "Giant Magnetoresistance

of (001)Fe/(001)Cr Magnetic Superlattices," *Phys. Rev. Lett.*, vol. 61, no. 21, pp. 2472–5, 1988.

[9] G. Binasch, P. Grünberg, F. Saurenbach, and W. Zinn, "Enhanced magnetoresistance in layered magnetic structures with antiferromagnetic interlayer exchange," *Phys. Rev. B*, vol. 39, no. 7, pp. 4828–30, 1989.

[10] J. M. Daughton, "Magnetoresistive memory technology," *Thin Solid Films*, vol. 216, pp. 162–8, 1992.

[11] C. A. Baron, M. Egilmez, C. J. E. Straatsma, K. H. Chow, J. Jung, and A. Y. Elezzabi, "The effect of a semiconductor-metal interface on localized terahertz plasmons," *Appl. Phys. Lett.*, vol. 98, no. 11, pp. 111 106/1–3, 2011.

[12] C. A. Baron, "Terahertz Spinplasmonic Devices," Master's thesis, University of Alberta, 2009.

[13] A. Hütten, T. Hempel, S. Heitmann, and G. Reiss, "The Limit of the Giant Magnetoresistance Effect in Only Three Layers," *Phys. Status Solidi*, vol. 189, no. 2, pp. 327–38, 2002.

[14] C. A. Baron and A. Y. Elezzabi, "A 360° angularly ranging time-domain terahertz spectroscopy system," *Meas. Sci. Technol.*, vol. 19, no. 6, pp. 065 602/1–7, 2008.

[15] E. Hirota, H. Sakakima, and K. Inomata, *Giant Magneto-Resistance Devices*. Berlin: Springer-Verlag, 2002.

[16] W. Zou, H. N. G. Wadley, X. W. Zhou, S. Ghosal, R. Kosut, and D. Brownell, "Growth of giant magnetoresistance multilayers: Effects of

processing conditions during radio-frequency diode deposition," *J. Vac. Sci. Technol. A*, vol. 19, no. 5, pp. 2414–24, 2001.

Chapter 5

Investigation of Magnetically Tunable Terahertz Resonators[1]

5.1 Background

Planar plasmonic metamaterials have found a number of uses at THz frequencies due to their simple fabrication process and highly configurable properties. In particular, they have found applications as both thin-film sensors [1, 2] and filter elements [3–5]. Unfortunately, the devices in the works cited are inherently passive, and in order to extend their functionality the ability to dynamically control their electromagnetic response is a necessity. To date, a number of active device schemes have been proposed based on electrostatic tunability [6, 7], magnetostatic tunability [8, 9], thermal tunability [9, 10], optical pumping of semiconductors [11, 12], the incorporation of superconducting materials [13] and the incorporation of metal-insulator transition materials [14]. The main issue with these proposed schemes is that they either increase the complexity of fabrication through the inclusion of exotic materials or require

[1] A portion of this chapter has been submitted for publication in *Journal of Infrared, Millimeter, and Terahertz Waves.*

the implementation of an optical pumping scheme. To make these devices truly functional, an active control scheme that does not introduce these complexities is desirable.

Previous experiments with random plasmonic metamaterials [15–17], including those of Chapter 4, have shown strong evidence that the magnetoresistivity of ferromagnetic materials is a promising candidate for developing active THz devices. The random structures investigated thus far exhibit a significant magnetic field dependent transparency, where a $\sim 60\%$ decrease in the radiation transmitted through such a structure has been observed for magnetic field strengths of 120 mT [16]. However, the electromagnetic interaction responsible for transporting the incident radiation through these random structures is based upon the coupling of *non-resonant* localized surface plasmon modes. Therefore, a structure which is *resonant* with the incident electromagnetic field should experience a stronger dependence on the resistivity of the underlying material, which will result in an increased response to an applied magnetic field. Due to their resonant response, planar metallic resonators are an excellent structure for testing this hypothesis.

This section explores the potential for using the magnetoresistivity of ferromagnetic metals to actively tune the resonances of a series of planar THz metamaterials. Specifically, periodic arrays of subwavelength holes, particles and double split-ring resonators (SRRs) are studied under the influence of an applied magnetic field. Also, a passive device of a new design exhibiting two modes of operation is presented. First, three-dimensional (3D) FDTD simulations are utilized to design the structures such that their resonances lie within the useable bandwidth of the experimental THz-TDS system described in Chapter 2 (0.1 - 1.4 THz). The structures are then patterned on high-resistivity silicon using conventional photolithography, metallization and

lift-off processes, and their passive operation is verified. Finally, the structures' responses are monitored as a function of an applied magnetic field.

5.2 Design and Fabrication

The first resonator structure studied is a periodic array of subwavelength holes in a conducting film. Periodic arrays of subwavelength holes in conducting media exhibit an extraordinary transparency to incident electromagnetic radiation due to the resonant excitation of SPP modes on the metal surface [18–20]. In this way, an enhanced transmission is realized whenever momentum is conserved at either interface of the metal film, giving rise to SPP modes. Essentially, the SPP modes at the incident interface couple with diffracted radiation and subsequently tunnel through the apertures to the opposite interface from where they radiate into freespace. The result is an enhanced transmission of the incident radiation when compared to that predicted by diffraction theory. The actual frequencies at which these resonances occur can be estimated by combining the dispersion relation for SPPs at a metal/dielectric interface, equation (1.2.3.8), with the momentum matching condition for a two-dimensional grating, equation (1.2.3.11), which results in

$$f_{SPP} = c\sqrt{\left(\frac{m}{a}\right)^2 + \left(\frac{n}{b}\right)^2}\sqrt{\frac{\tilde{\epsilon}_m + \tilde{\epsilon}_d}{\tilde{\epsilon}_m \tilde{\epsilon}_d}} \tag{5.2.0.1}$$

where normal incidence and permeable media ($\tilde{\mu} = \mu_0$) have been assumed, and the subscripts define the metal (m) and the dielectric (d). At THz frequencies $|\tilde{\epsilon}_m| >> |\tilde{\epsilon}_d|$ such that equation (5.2.0.1) can be approximated by

$$f_{SPP} \approx c\sqrt{\left(\frac{m}{a}\right)^2 + \left(\frac{n}{b}\right)^2}\sqrt{\frac{\epsilon_0}{\tilde{\epsilon}_d}} \tag{5.2.0.2}$$

As mentioned above, the structures under investigation consist of a metal thin-film patterned onto a high-resistivity silicon wafer. This gives rise to two interfaces capable of supporting SPP modes: the metal/dielectric interface, where the dielectric is silicon in this case, and the metal/air interface. At THz frequencies high-resistivity silicon exhibits very low absorptivity and dispersion [21] such that it can be well approximated as a lossless dielectric with a permittivity of $\tilde{\epsilon}_d = 11.7\epsilon_0$. This results in a simple relation for the resonance frequency of the SPP modes of such a structure, the first two of which are 0.58 THz ($[1, 0]$ or $[0, 1]$ mode) and 0.83 THz ($[1, 1]$ mode) for the metal/dielectric interface.

A schematic representation of the unit cell of the hole array under investigation here is given in Figure 5.2.0.1. The actual holes are square apertures with a side length of 75 µm and a periodicity of 150 µm along both dimensions. For the simulations, a 3D FDTD code incorporating periodic boundary conditions is developed and utilized (see Appendix D). To properly emulate the hole array, the unit cell of Figure 5.2.0.1 is surrounded by these periodic boundary conditions on four sides. As discussed above, the substrate is modelled as a lossless dielectric with parameters for silicon. The metal film is set to be 500 nm thick and is represented as a dispersive medium using a Drude model for the permittivity with parameters taken from [22]. The structure is excited from the substrate side such that the entire silicon wafer does not have to be simulated to find the radiation transmitted through the structure into freespace. Only a portion of the silicon ($\sim$ 100 µm) needs to be simulated to determine the proper resonance frequencies, as can be determined by convergence testing [4, 23]. Finally, the transmitted radiation is collected such that the transmission coefficient can be calculated as a function of frequency. The result of such a simulation for the hole array is shown in Figure 5.2.0.2 where

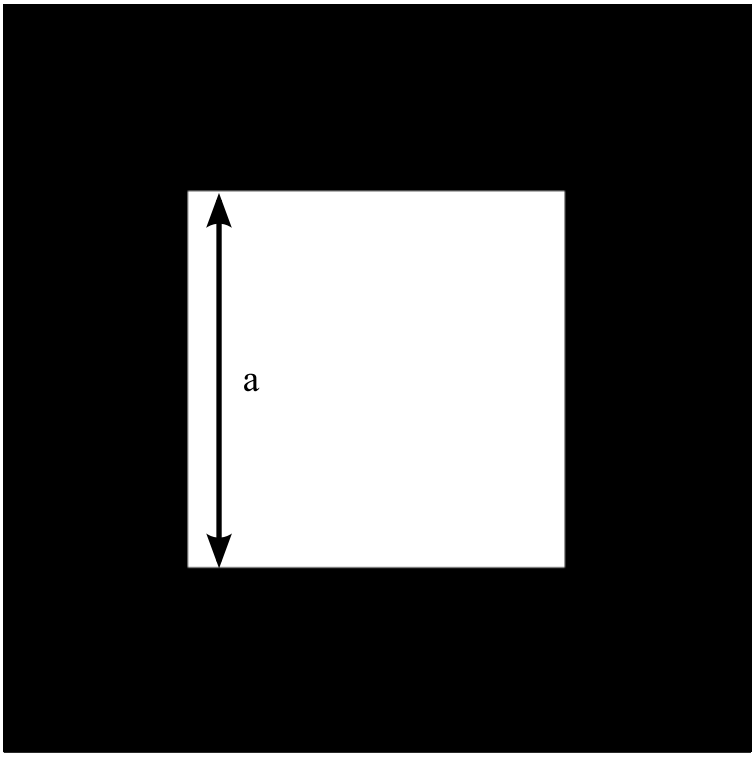

Figure 5.2.0.1: Unit cell of the hole array. The dimension $a = 75$ µm.

the transmission coefficient and relative phase are shown for a metal film of Au, Ni and Ti. Note that the magnitude of the conductivity for these metals at THz frequencies between 0.1 and 1.4 THz is $1.6 \times 10^7\ \Omega^{-1}$, $6.8 \times 10^6\ \Omega^{-1}$ and $1.3 \times 10^6\ \Omega^{-1}$ for Au, Ni and Ti, respectively, as calculated from the Drude model (see Appendix B). The vertical dashed lines represent the resonance modes predicted by equation (5.2.0.2) for a metal/silicon interface. The simulated resonances occur at 0.55 and 0.77 THz while the resonances predicted by equation (5.2.0.2) lie at 0.58 and 0.83 THz. The predicted modes occur at slightly higher frequencies because the calculation assumes that resonant SPP excitation is the only mechanism responsible for the extraordinary transmission. It has been found that localized waveguide resonances also contribute significantly to the extraordinary transmission and are the cause of the observed red-shifted resonances [24]. Interestingly, the response of the hole array

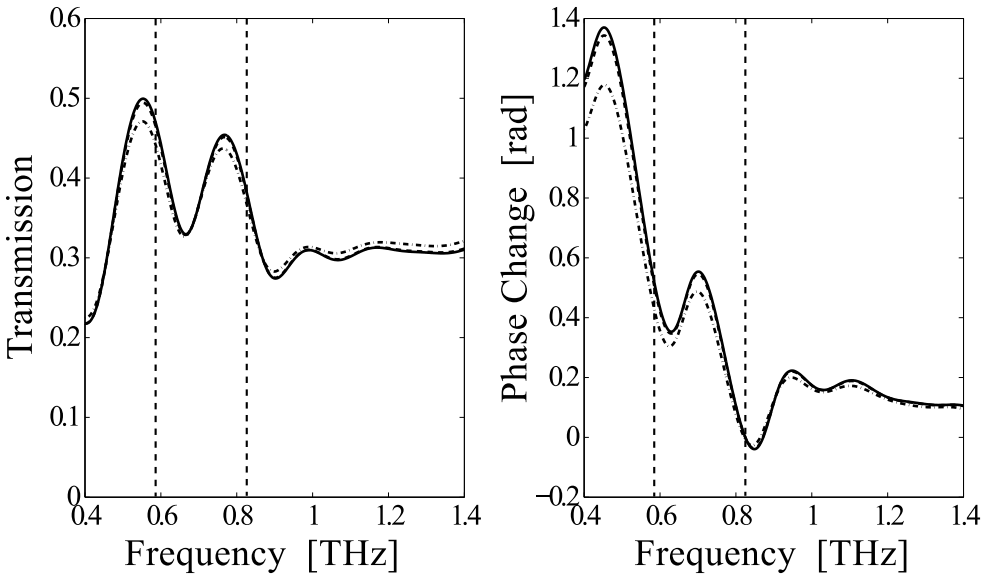

Figure 5.2.0.2: Simulated transmission and phase change for the square hole array structure. Three different metals are simulated: Au (solid), Ni (dashed) and Ti (dash-dot). The vertical dashed lines indicate the predicted $[1, 0]$ (or $[0, 1]$) and $[1, 1]$ SPP resonance modes

structure is not overly sensitive to the properties of the metal film. This has been investigated by Azad et al. [25] and can be attributed to the similar propagation lengths of the SPP modes on different metal films at THz frequencies.

The second resonator structure studied is the inverse of the last one, namely a periodic array of square particles. It was shown in Chapter 1 that subwavelength metallic spheres can support localized surface plasmon modes when excited by an electromagnetic wave. Moreover, these plasmon modes give rise to an oscillating charge distribution which radiates electromagnetic radiation like a dipole. Therefore, a periodic array of square particles should act in a similar fashion. The individual components of the array will support an oscillating dipole mode when excited by an electromagnetic wave. In turn, this mode will radiate electromagnetic radiation back to the incident wave. Thus, each particle will effectively act as a subwavelength antenna. At the resonance frequency of these antennae, a peak in the reflection spectrum will

arise due to strong radiation by the elements of the array, which corresponds to back-scattering of the incident wave. Furthermore, this will correspond to a minimum in the transmission spectrum. The frequency at which this occurs can be estimated using the half-wavelength approximation for a resonant antenna [26]

$$f_{HW} = \frac{c}{2L}\sqrt{\frac{\epsilon_0}{\tilde{\epsilon}_d}} \tag{5.2.0.3}$$

where L is the antenna length and $\tilde{\epsilon}_d$ is the electric permittivity of the substrate. A schematic representation of the unit cell of the particle array is given in Figure 5.2.0.3. The particles are squares with a side length of 75 µm and a periodicity of 150 µm along both dimensions. The simulations performed are

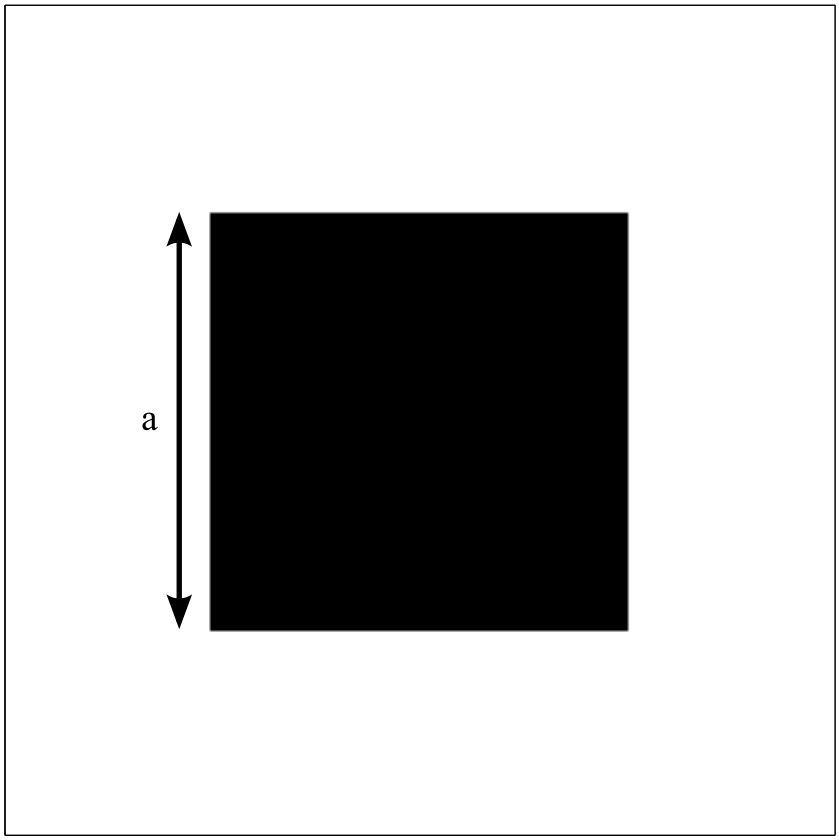

Figure 5.2.0.3: Unit cell of the particle array. The dimension $a = 75$ µm.

identical to the case of the hole array, the results of which are shown in Figure 5.2.0.4 where the transmission coefficient and relative phase are shown for a

metal film of Au, Ni and Ti. The vertical dashed line represents the resonance

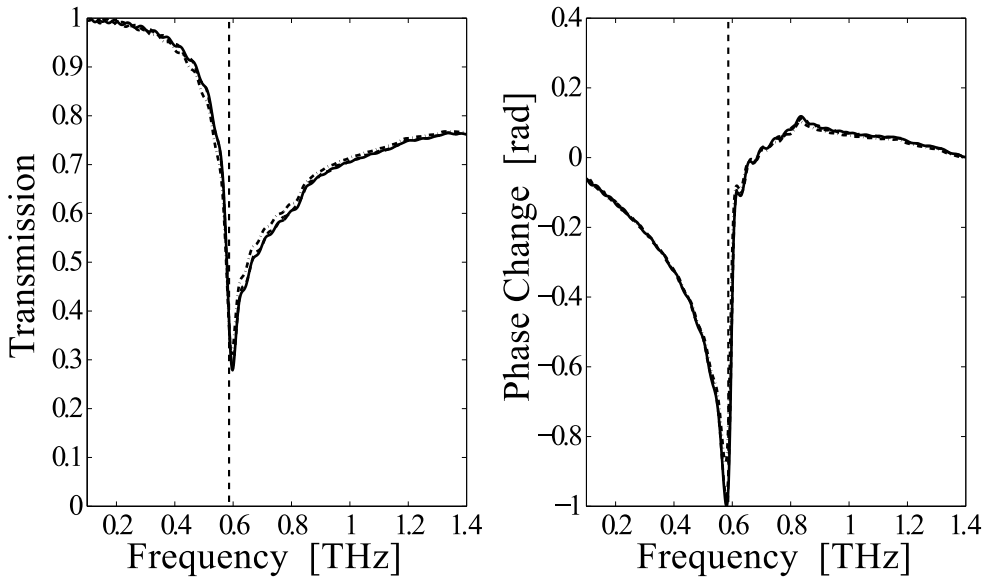

Figure 5.2.0.4: Simulated transmission and phase change for the square particle array structure. Three different metals are simulated: Au (solid), Ni (dashed) and Ti (dash-dot). The vertical dashed line indicates the predicted half-wavelength resonance.

mode predicted by equation (5.2.0.3). The simulated resonance occurs at 0.60 THz with a quality factor (Q-factor) of 2.2, while the resonance predicted by equation (5.2.0.3) is 0.58 THz. The slight blue-shift in the observed resonance in this case can be attributed to mutual interactions between adjacent particles in the array, which is not taken into consideration by the half-wavelength approximation. This structure is practically insensitive to the properties of the metal film, which is evidenced by the barely observable change in the transmission coefficient and phase when comparing the results for Au, Ni and Ti.

The third resonator structure studied is a periodic array of double SRRs. The SRR structure exhibits a magnetic response under normal incidence resulting from the resonant excitation of currents travelling in the ring, which give rise to magnetic dipole moments. Because this response is resultant from the electric field of an incident electromagnetic wave it is known as the elec-

trically excited magnetic resonance (EEMR) [27]. Due to its geometry, the resonance feature of the SRR can be modelled by an equivalent RLC circuit with the components in series, as depicted in Figure 5.2.0.5. Here, the resis-

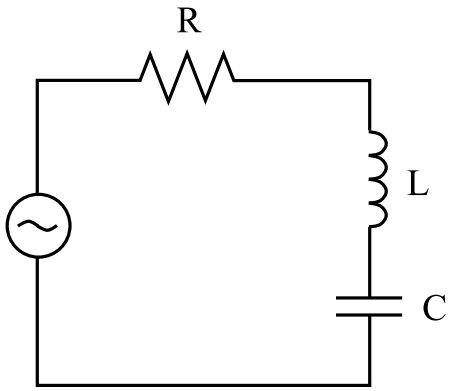

Figure 5.2.0.5: A circuit representation for the SRR structure. R: resistance, L: inductance and C: capacitance.

tance (R) arises from the finite conductivity of the metal film, the inductance (L) arises from the induced currents in the ring and the capacitance (C) arises from charge accumulation at the gap in the ring. Therefore, the resonant frequency can be estimated by $f_{SRR} = \frac{1}{2\pi\sqrt{LC}}$, which is the result for a series RLC circuit. The double SRR structure works to enhance the resonance of a single SRR since it supports a higher current density. Also, it should be noted that the SRR structure supports another higher frequency resonance akin to the one described above for the case of a square particle, but it is not of interest here. A schematic representation of the unit cell of the double SRR array is given in Figure 5.2.0.6. The dimensions of the structure are given in the figure caption. The periodicity is 100 µm along both dimensions. Once again, the simulations are performed in the same manner noted above. These results are shown in Figure 5.2.0.7 where the transmission function and relative phase is shown for a metal film of Au, Ni and Ti. The LC resonance depicted here occurs at 0.22 THz with quality factors (Q-factors) of 2.8, 2.5 and 2.0 for Au, Ni and Ti, respectively. It is sensitive to the properties of

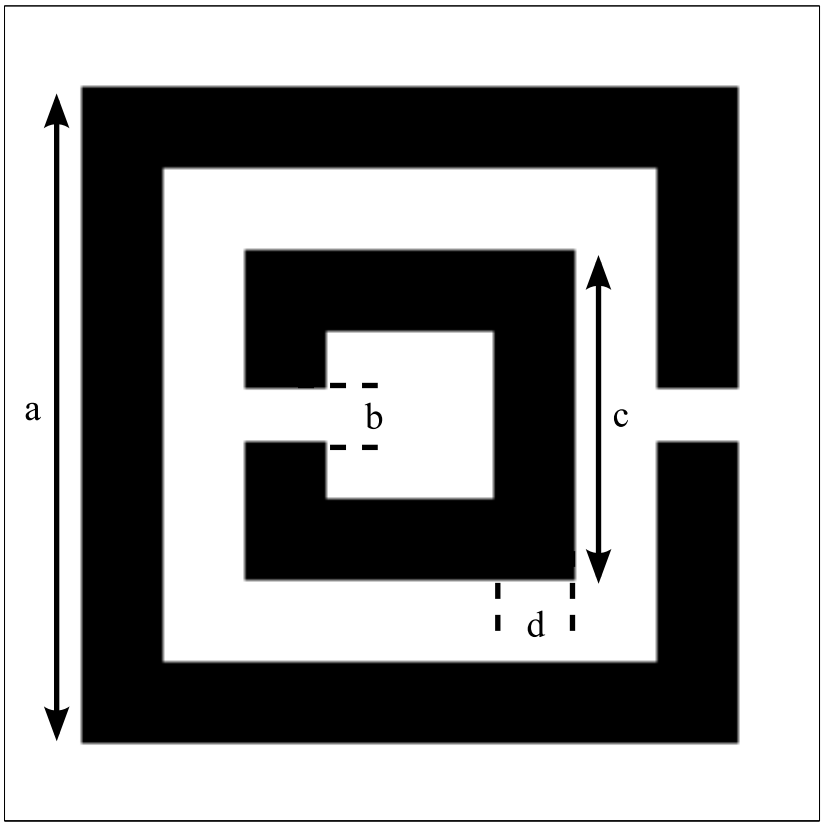

Figure 5.2.0.6: The unit cell of the double SRR array. The dimensions are as follows: $a = 80$ µm, $b = 6$ µm, $c = 40$ µm and $d = 10$ µm.

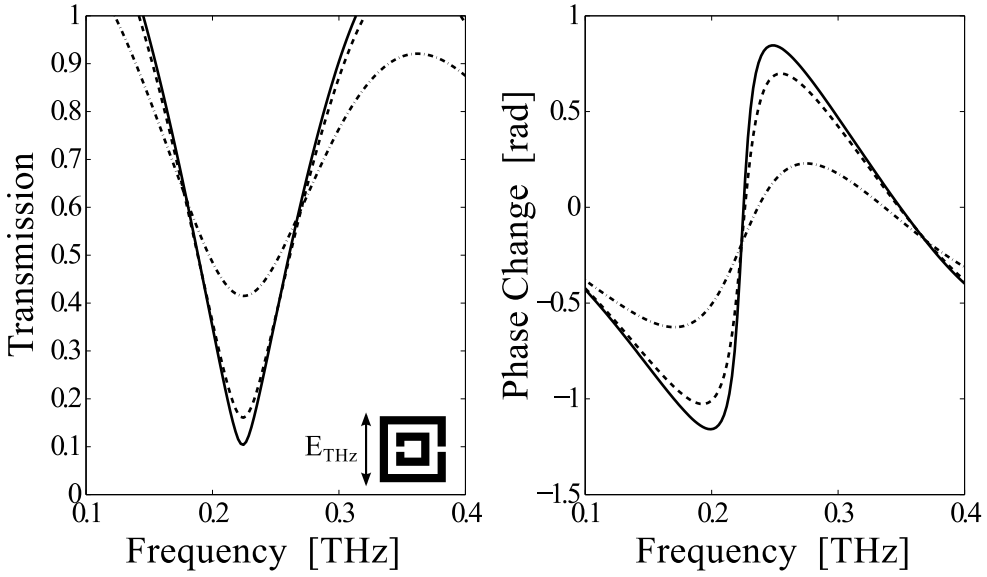

Figure 5.2.0.7: The LC resonance is depicted for the simulated double SRR structure. Three different metals are simulated: Au (solid), Ni (dashed) and Ti (dash-dot). The inset shows the electric field polarization with respect to the structure.

the metal film as evidenced by the significant change in the transmission and phase when comparing Au, Ni and Ti films. This fact has been reported on by Singh et al. [28] and can be attributed to the difference in conductivity between the materials. Essentially, the better conducting the material is at THz frequencies the more pronounced the resonance feature becomes. This is intuitive since the LC resonance arises from an induced current density in the rings, and a higher conductivity material will support a larger current density.

The final resonator structure studied is a passive device of a new design based on the symmetric dual-band resonator structure of Ma et al. [4]. The dual-band structure operates as a double notch filter due to the simultaneous excitation of two resonant modes. The new design introduces an asymmetry to Ma et al.'s structure resulting in multiple modes of operation depending on the polarization direction of the incident electromagnetic wave. As such, this structure has been named the asymmetric dual-band resonator. One mode of operation exhibits a notch plus stop band filter response, while the other mode of operation realizes a notch filter response. A schematic representation of the unit cell for this structure is given in Figure 5.2.0.8. The dimensions of the structure are given in the figure caption. The periodicity is 100 µm along the long-arm dimension and 60 µm along the short-arm dimension. The simulations are performed in the manner noted above, but two are run for this particular structure to show both modes of its operation. These results are shown in Figure 5.2.0.9 where the transmission function and relative phase is shown for a metal film of Au. When the THz electric field is polarized along the long arm of the structure, two resonance features arise: one at 0.69 THz with a Q-factor of 3.9 and the other at 0.89 THz. However, when the field is polarized along the short arm a single resonance arises at 0.63 THz with a Q-factor of 7.9. Therefore, this structure can realize two modes of operation

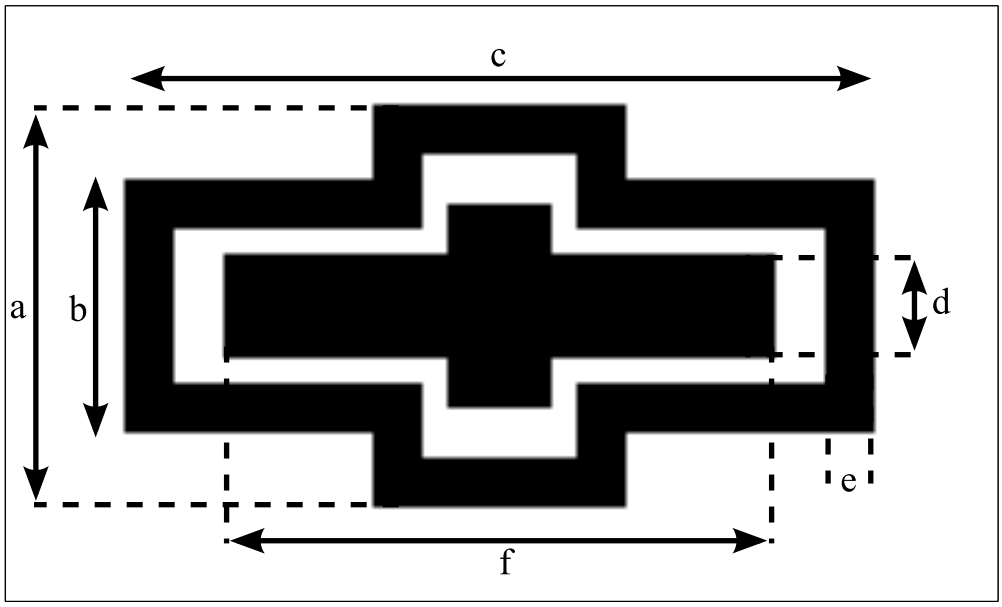

Figure 5.2.0.8: The unit cell of the asymmetric dual-band resonator array. The dimensions are as follows: $a = 40$ µm, $b = 25$ µm, $c = 80$ µm, $d = 10$ µm, $e = 5$ µm and $f = 55$ µm.

dependent on the polarization of the incident electric field. In one case it acts as a notch plus stop band filter, while in the other it acts as only a notch filter. By destroying the symmetry in the original design, a new device with higher functionality is realized.

To fabricate these structures a photolithography process is used to pattern the structures onto a silicon wafer. First, a high-resistivity silicon wafer is spin-coated with HPR-504 photoresist[2], which is then exposed to ultraviolet light for 2.2 s through a photomask containing the desired patterns. After developing the resist in 354 developer for 25 s, a dc magnetron sputtering system[3] is used to deposit the metal film of choice. Following the metallization step the wafer is immersed in a bath of acetone for 45 min to lift-off the remaining photoresist. If required, an ultrasonic bath can be used to provide agitation to

[2]A 10 s spread cycle at 500 rpm is followed by a 40 s spin cycle at 4000 rpm. The resist is then soft-baked for 90 s at 115° C.

[3]The system used here is the "Bob" sputtering system located at the University of Alberta NanoFab facility.

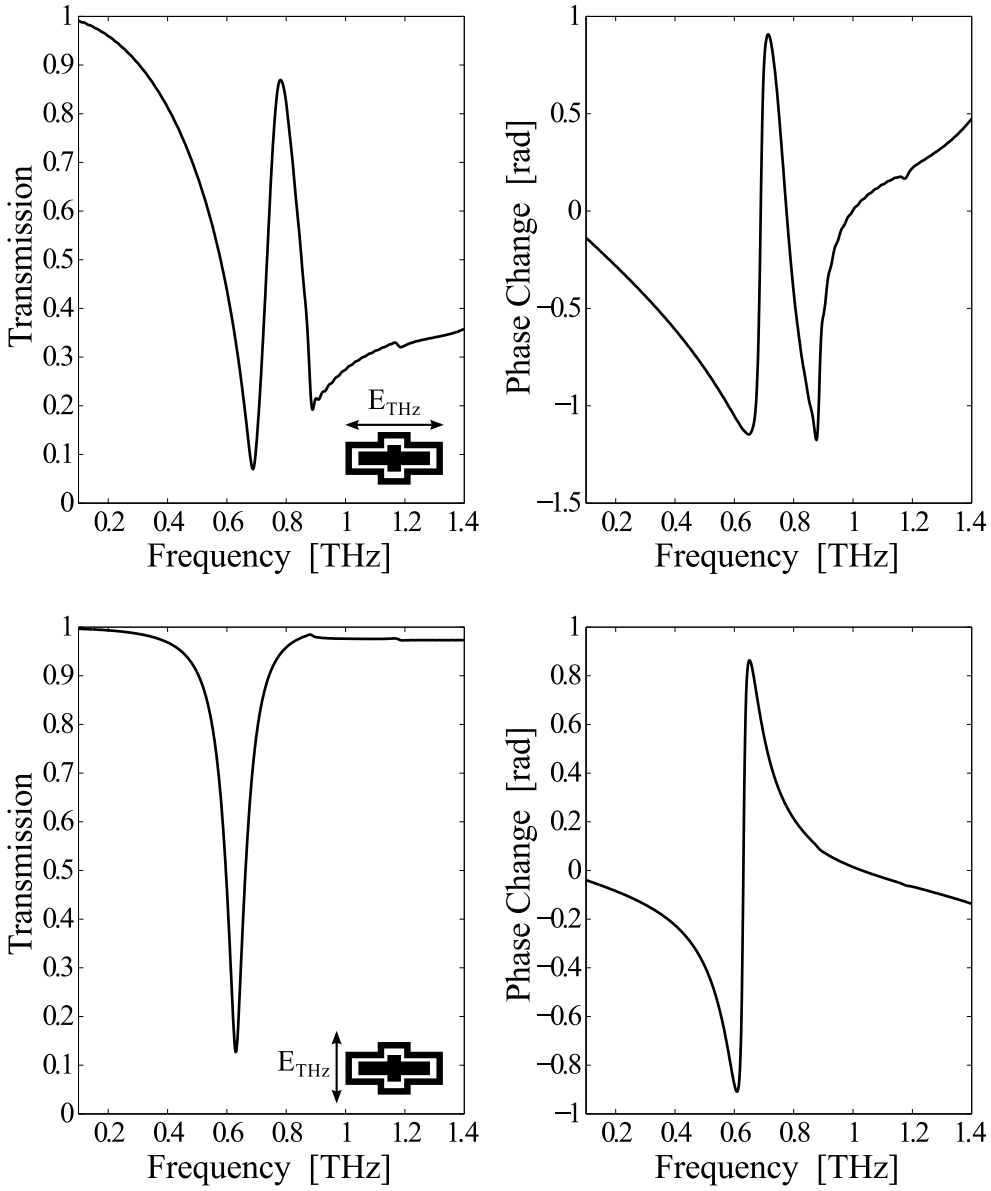

Figure 5.2.0.9: The simulated transmission and phase change for the asymmetric dual-band resonator structure is shown. The top panels show the situation when the electric field is polarized along the long arm of the structure (see inset). The bottom panels show the opposite polarization as indicated by the inset.

assist the lift-off process. Figure 5.2.0.10 shows an optical microscope image of a portion of the fabricated arrays for each of the four structures mentioned.

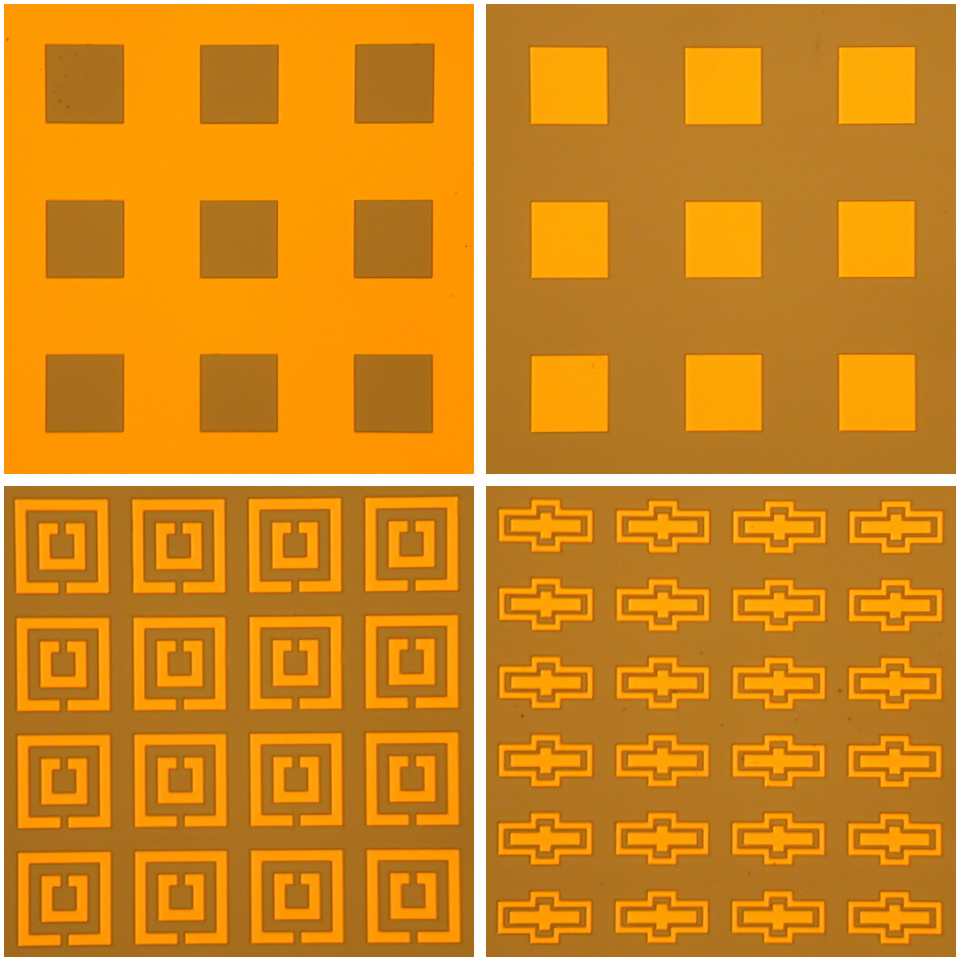

Figure 5.2.0.10: Optical microscope images of the fabricated arrays. Top left: hole array, top right: particle array, bottom left: double SRR array and bottom right: asymmetric dual-band resonator array.

5.3 Passive Operation

This section focuses on the passive operation of the four resonator structures described above. The fabricated structures here consist of a 15 nm/185 nm Ti/Au film, where the Ti is used as an adhesion layer for the Au. To test the

transmission properties of the resonators, the setup described in Chapter 2 is utilized. The samples are placed approximately 1" away from the focal point of the system to maximize the interaction between the THz radiation and the array. The beam spot size here is $\sim$ 2 mm as measured by the knife-edge technique. To calculate the transmission function a reference signal, $E_{ref}(t)$, through the bare substrate is acquired first followed by a shot through the structure, $E_{str}(t)$. The THz pulse is incident on the structure from the substrate side, and the transmission function is calculated using the amplitude spectra of the reference and structure signals

$$t(\omega) = \frac{E_{str}(\omega)}{E_{ref}(\omega)}$$
$$T(\omega) = t(\omega)\, t^*(\omega)$$

The experimental results for the fabricated structures will be presented here in the same order as above. For the hole array, the transmission and phase change are depicted in Figure 5.3.0.11. Two resonance features arise

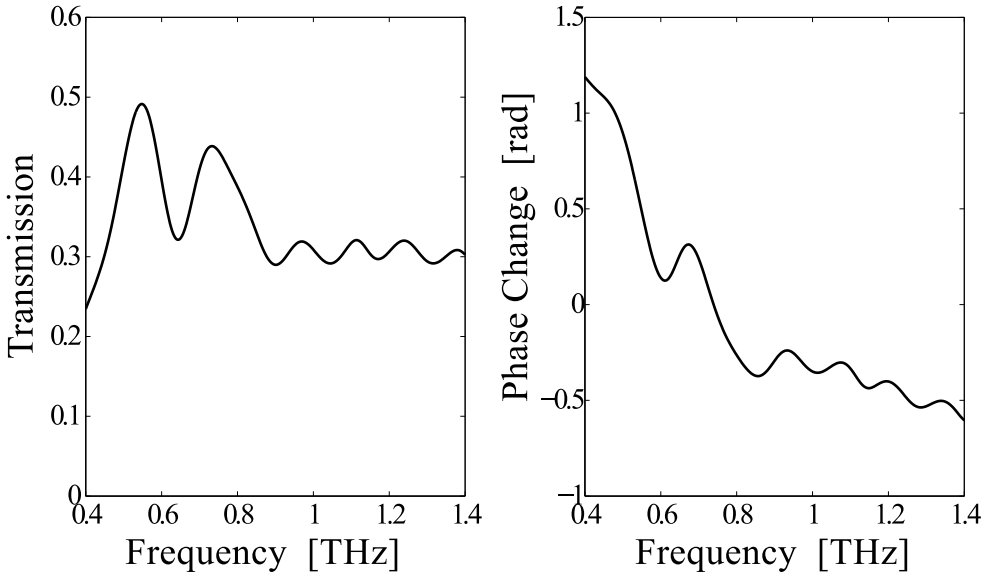

Figure 5.3.0.11: Experimentally determined transmission and phase change for the fabricated square hole array.

at 0.55 THz and 0.73 THz, which agree well with the resonances of the simulated Au structure occurring at 0.55 THz and 0.77 THz. The transmission and phase change for the particle array are shown in Figure 5.3.0.12. A single

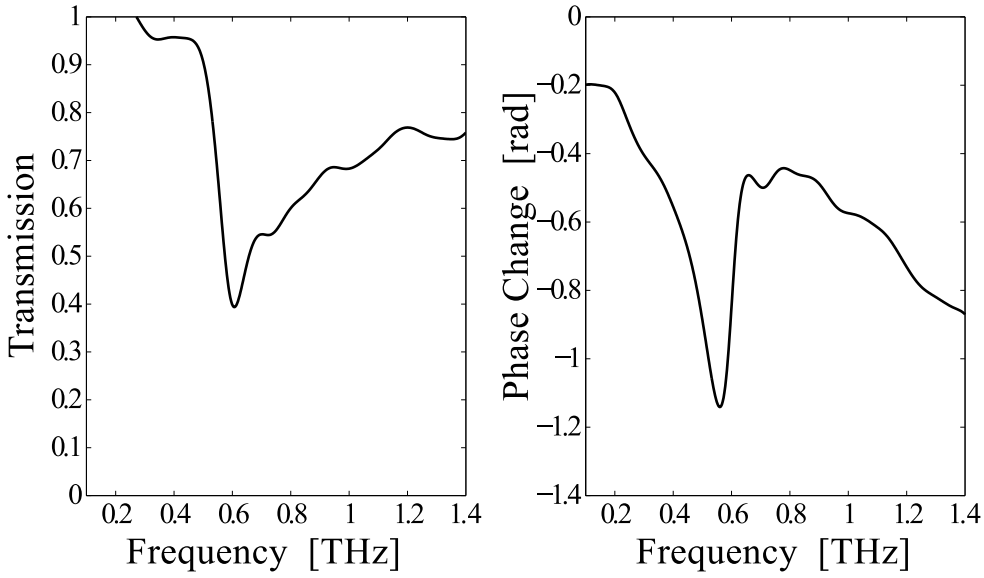

Figure 5.3.0.12: Experimentally determined transmission and phase change for the fabricated square particle array.

resonance arises at 0.61 THz with a Q-factor of 1.2, which also agrees well with the resonance of the simulated Au structure occurring at 0.60 THz with a Q-factor of 2.2. For the double SRR structure, the transmission and phase change are shown in Figure 5.3.0.13. The LC resonance for the fabricated structure is located at 0.21 THz with a Q-factor of 3.0, which also agrees well with the resonance of the simulated Au structure occurring at 0.22 THz with a Q-factor of 2.8. Finally, the transmission and phase change for the asymmetric dual-band resonator structure are shown in Figure 5.3.0.14. When the electric field is polarized along the long arm, one resonant feature arises at 0.69 THz with a Q-factor of 3.7 while the other arises at 0.91 THz, which agrees well with the resonances of the simulated structure occurring at 0.69 THz with a Q-factor of 3.9 and 0.89 THz. For the other polarization scheme, a single resonance arises at 0.63 THz with a Q-factor of 5.7, which also agrees

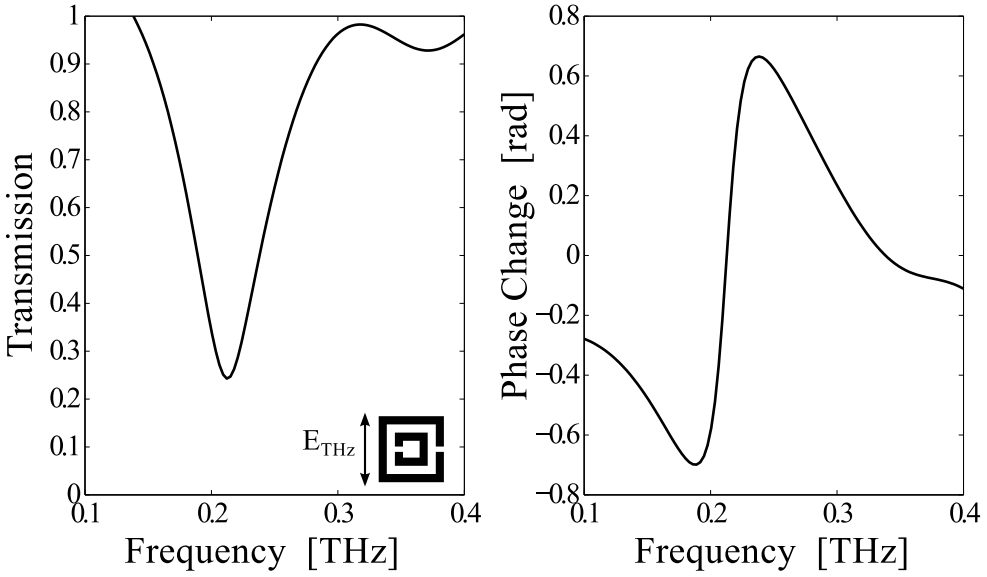

Figure 5.3.0.13: Experimentally determined transmission and phase change for the fabricated double SRR array.

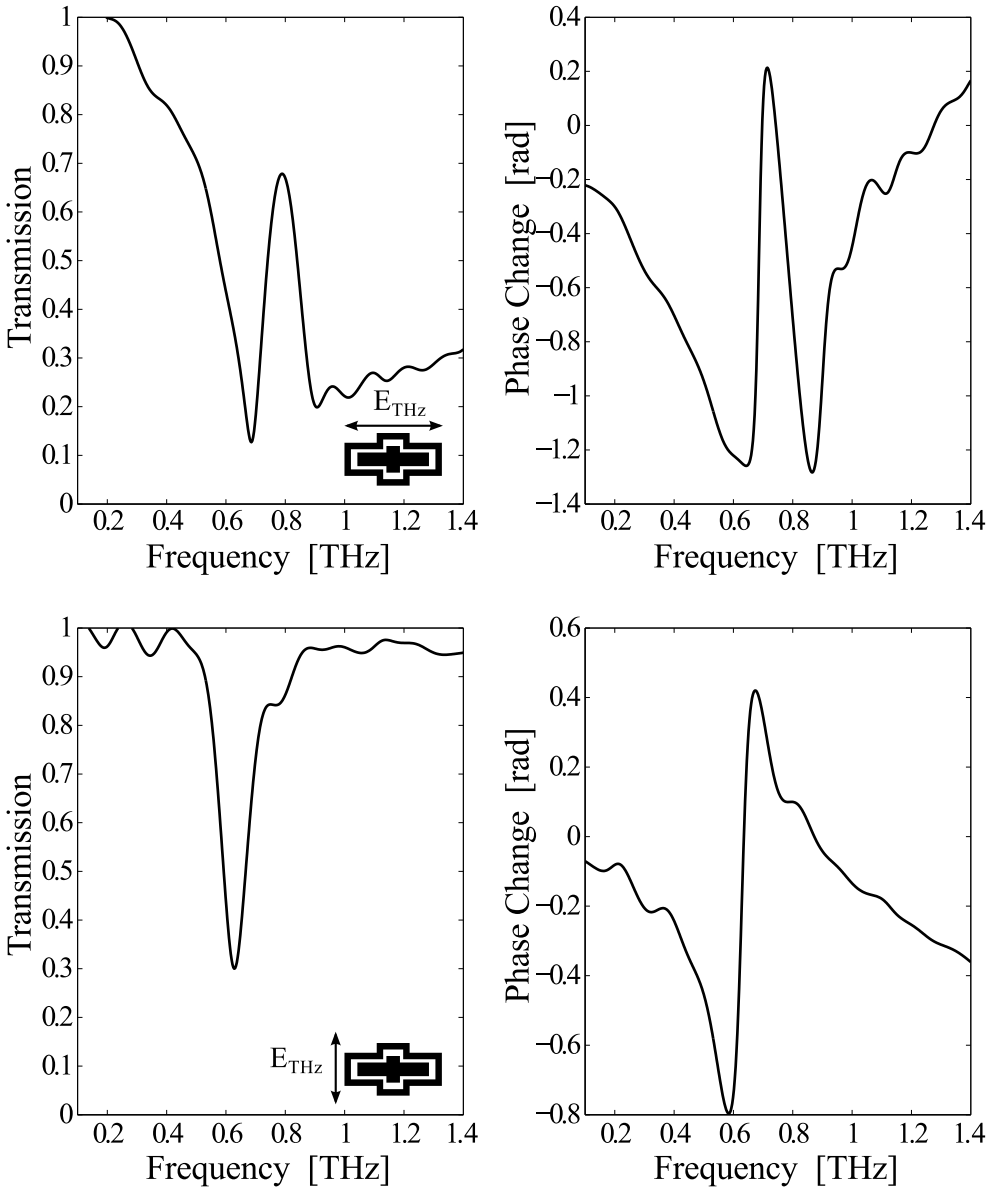

Figure 5.3.0.14: Experimentally determined transmission and phase change for the fabricated asymmetric dual-band resonator. The top panels indicate when the polarization is parallel to the long arm of the structure while the bottom panels indicate the case when the polarization is parallel to the short arm. This is shown by the insets.

well the the resonance of the simulated structure occurring at 0.63 THz with a Q-factor of 7.9.

The small discrepancies between the simulated and experimentally determined resonance features can be attributed to shortcomings of the material models used for the simulations, as well as noise from the experimental THz-TDS system. Specifically, the fabricated structures make use of a thin Ti adhesion layer, which is not taken into consideration by the simulations; the simulated structures are assumed to made of Au only. Also, minor losses associated with the high-resistivity silicon wafer used for fabrication are neglected in the simulations. Finally, noise associated with acquiring the time-domain THz waveforms and subsequent processing of this data (see Figure 2.2.0.8) will also cause discrepancy between the simulated and experimentally determined resonance features.

5.4 Active Operation

This section focuses on the active operation of the resonator structures described above. The fabricated structures here consist of a 200 nm Ni film. The experimental process is identical to that described above, but this time the transmission function of the structure in the presence of a 0.5 T magnetic field is compared to the zero-field case. To begin with, the double SRR structure is chosen since its resonant response shows the most dependence on the conductivity of the metallic film used in its fabrication, as evidenced by the simulations. This is due to the fact that the LC resonance is dependent on the current density generated in the rings, which implies that this structure should be the most sensitive to a change in the resistivity of the metal caused by a magnetoresistance effect.

Figure 5.4.0.15 shows the transmission function and phase change of the double SRR array at zero-field and 0.5 T for a magnetic field applied parallel and perpendicular to the polarization of the THz electric field. It is clear that

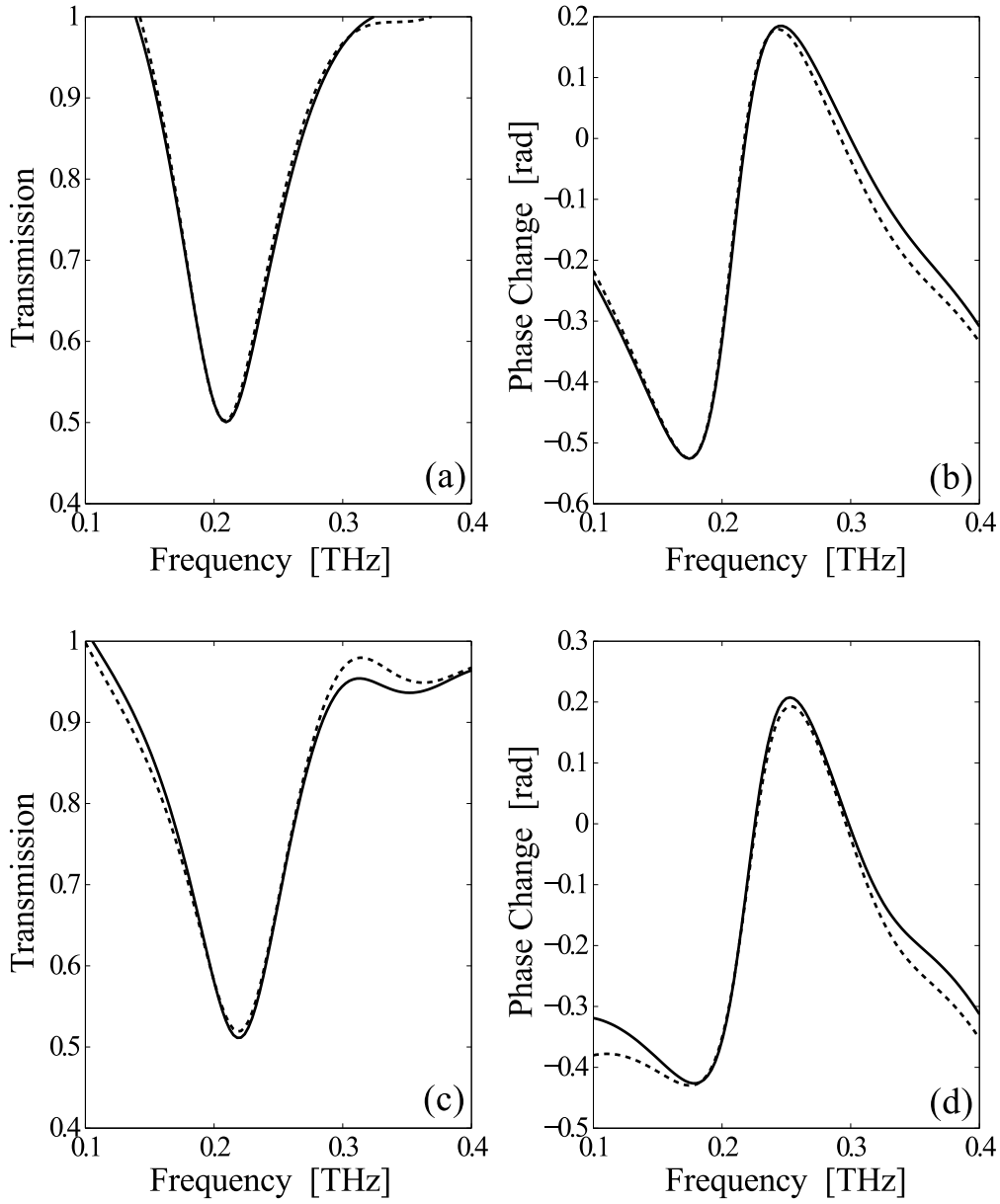

Figure 5.4.0.15: Experimentally determined (a) transmission and (b) phase change for a magnetic field applied parallel to the THz electric field. The perpendicular case is shown in (c) and (d). The solid line corresponds to a field of 0 mT and the dashed line corresponds to 500 mT.

no significant change occurs from the application of a magnetic field. This

is surprising considering the significant AMR effect demonstrated by Chau et al. [16] in dense ensembles of Ni particles. In this work, the authors show an approximately 60% decrease in the total power of the THz pulse transmitted through a 1.9 mm thick sample of $\sim$ 150 µm diameter Ni microparticles. The maximum applied magnetic field in this case is 120 mT. A possible reason for the discrepancy could be that in Chau et al.'s experiment there is significantly more interaction between the THz radiation and the Ni structures. In this case the spot size of the THz beam interacting with the sample can be approximated as 1 mm (corresponding to the focal point of the system) in diameter. Within this beam spot there are about 45 particles present. Multiplying this by the estimated 13 particles that lie along the thickness of the sample cell gives a total of 585 particles. Taking an approximate packing fraction of 0.6 into account results in about 350 particles interacting with the THz radiation. For the experiment done here with periodic arrays, the THz beam spot is about 2 mm and the periodicity of the structures is 100 µm. This gives about 315 structures interacting with the THz beam, which is comparable to the experiment of Chau et al. However, in the case of the particles the transmission of radiation through the ensemble is mediated by a near-field interaction between electric fields confined to the surface of the particles. Therefore, the electric field amplitudes in this situation will be significantly higher than those interacting with the double SRR structure. This means that the induced current densities will be larger in the particles resulting in the transmitted THz radiation being much more sensitive to small changes in the resistivity. This sensitivity to resistivity is corroborated by Chau and Elezzabi's results for THz transmission through ensembles of Cu and $Cu_{95}Sn_5$ particles [29], where it was found that the higher resistivity $Cu_{95}Sn_5$ particles exhibit an approximate 30% decrease in transparency to incident THz radiation when compared

to the transparency of a Cu particle ensemble.

Based on the simulations run for the double SRR structure, it is possible to estimate the change in resistivity required to produce an observable change in the resonance. A distinction between the resonance feature of the double SRR structure is evident when comparing the transmission function for a Au and Ni film (Figure 5.2.0.7), where a 35% decrease in amplitude at 0.22 THz is observed. This shows that the higher resistivity Ni film results in a weaker resonance than the lower resistivity Au film. Based on the Drude model for the electric permittivity used in these simulations, the magnitude of the resistivity at THz frequencies can be estimated for these two metals as 6.4×10^{-8} Ω for Au and 1.5×10^{-7} Ω for Ni (see Appendix B). This corresponds to a total resistance change of about 57%, which is quite large considering the effect this has on the resonance of the structure.

As a final note, the other structures discussed above (square hole and particle arrays) were also fabricated with a 200 nm Ni film and tested in the same fashion as the double SRR array; however, no change in the transmission due to an applied magnetic field was observed. In light of the results for the double SRR structure, this is expected since these structures demonstrate a much weaker dependence on the properties of the metal film used when compared to the double SRR structure. Finally, it is possible that a SRR structure with a significantly higher Q-factor (higher induced current density) at its LC resonance, such as that demonstrated by Jansen et al. [5], would exhibit a change in its resonance due to a magnetoresistance effect. As such, this type of structure represents an excellent starting point for future work in this area.

5.5 Conclusion

In conclusion, a series of THz planar metamaterials were designed and fabricated for experimental verification. The FDTD simulation technique was utilized for the design stage such that the resonant feature of the structures were located within the useable bandwidth of the experimental system. Following this, passive operation of the fabricated structures was verified using the THz-TDS technique. The magnetoresistance effect in Ni was then investigated as a candidate for active control over the THz response of the structures through the application of an external magnetic field. It was found that this had no effect on the electromagnetic response of the structures due to insufficient interaction with the device and small resistivity change in the Ni film.

Chapter 5 References

[1] J. F. O'Hara, R. Singh, I. Brener, E. Smirnova, J. Han, A. J. Taylor, and W. Zhang, "Thin-film sensing with planar terahertz metamaterials: sensitivity and limitations," *Opt. Exp.*, vol. 16, no. 3, pp. 1786–95, 2008.

[2] I. A. I. Al-Naib, C. Jansen, and M. Koch, "Thin-film sensing with planar asymmetric metamaterial resonators," *Appl. Phys. Lett.*, vol. 93, no. 8, pp. 083 507/1–3, 2008.

[3] D. Qu, D. Grischkowsky, and W. Zhang, "Terahertz transmission properties of thin, subwavelength metallic hole arrays," *Opt. Lett.*, vol. 29, no. 8, pp. 896–8, 2004.

[4] Y. Ma, Q. Chen, A. Khalid, S. C. Saha, and D. R. S. Cumming, "Terahertz dual-band resonator on silicon," *Opt. Lett.*, vol. 35, no. 4, pp. 469–71, 2010.

[5] C. Jansen, I. A. I. Al-Naib, N. Born, and M. Koch, "Terahertz metasurfaces with high Q-factors," *Appl. Phys. Lett.*, vol. 98, no. 5, pp. 051 109/1–3, 2011.

[6] H.-T. Chen, W. J. Padilla, J. M. O. Zide, A. C. Gossard, A. J. Taylor, and R. D. Averitt, "Active terahertz metamaterial devices," *Nature*, vol. 444, pp. 597–600, 2006.

[7] H.-T. Chen, W. J. Padilla, M. J. Cich, A. K. Azad, R. D. Averitt, and A. J. Taylor, "A metamaterial solid-state terahertz phase modulator," *Nat. Photon.*, vol. 3, pp. 148–51, 2009.

[8] J. Han, A. Lakhtakia, and C.-W. Qiu, "Terahertz metamaterials with semiconductor split-ring resonators for magnetostatic tunability," *Opt. Exp.*, vol. 16, no. 19, pp. 14 390–6, 2008.

[9] J. Han, A. Lakhtakia, Z. Tian, X. Lu, and W. Zhang, "Magnetic and magnetothermal tunabilities of subwavelength-hole arrays in a semiconductor sheet," *Opt. Lett.*, vol. 34, no. 9, pp. 1465–7, 2009.

[10] R. Singh, A. K. Azad, Q. X. Jia, A. J. Taylor, and H.-T. Chen, "Thermal tunability in terahertz metamaterials fabricated on strontium titanate single-crystal substrates," *Opt. Lett.*, vol. 36, no. 7, pp. 1230–2, 2011.

[11] N.-H. Shen, M. Kafesaki, T. Koschny, L. Zhang, E. N. Economou, and C. M. Soukoulis, "Broadband blueshift tunable metamaterials and dual-band switches," *Phys. Rev. B*, vol. 79, no. 16, pp. 161 102/1–4, 2009.

[12] A. K. Azad, H.-T. Chen, S. R. Kasarla, A. J. Taylor, Z. Tian, X. Lu, W. Zhang, H. Lu, A. C. Gossard, and J. F. O'Hara, "Ultrafast optical control of terahertz surface plasmons in subwavelength hole arrays at room temperature," *Appl. Phys. Lett.*, vol. 95, no. 1, pp. 011 105/1–3, 2009.

[13] B. Jin, C. Zhang, S. Engelbrecht, A. Pimenov, J. Wu, Q. Xu, C. Cao, J. Chen, W. Xu, L. Kang, and P. Wu, "Low loss and magnetic field-tunable superconducting terahertz metamaterial," *Opt. Exp.*, vol. 18, no. 16, pp. 17 504–9, 2010.

[14] T. Driscoll, S. Palit, M. M. Qazilbash, M. Brehm, F. Keilmann, B.-G. Chae, S.-J. Yun, H.-T. Kim, S. Y. Cho, N. M. Jokerst, D. R. Smith, and D. N. Basov, "Dynamic tuning of an infrared hybrid-metamaterial

resonance using vanadium dioxide," *Appl. Phys. Lett.*, vol. 93, no. 2, pp. 024 101/1–3, 2008.

[15] K. J. Chau and A. Y. Elezzabi, "Photonic Anisotropic Magnetoresistance in Dense Co Particle Ensembles," *Phys. Rev. Lett.*, vol. 96, no. 3, pp. 033 903/1–4, 2006.

[16] K. J. Chau, C. A. Baron, and A. Y. Elezzabi, "Isotropic photonic magnetoresistance," *Appl. Phys. Lett.*, vol. 90, no. 12, pp. 121 122/1–3, 2007.

[17] K. J. Chau, M. Johnson, and A. Y. Elezzabi, "Electron-Spin-Dependent Terahertz Light Transport in Spintronic-Plasmonic Media," *Phys. Rev. Lett.*, vol. 98, no. 13, pp. 133 901/1–4, 2007.

[18] T. W. Ebbesen, H. J. Lezec, H. F. Ghaemi, T. Thio, and P. A. Wolff, "Extraordinary optical transmission through sub-wavelength hole arrays," *Nature*, vol. 391, pp. 667–9, 1998.

[19] E. Popov, M. Nevière, S. Enoch, and R. Reinisch, "Theory of light transmission through subwavelength periodic hole arrays," *Phys. Rev. B*, vol. 62, no. 23, pp. 16 100–8, 200.

[20] W. L. Barnes, W. A. Murray, J. Dintinger, E. Devaux, and T. W. Ebbesen, "Surface Plasmon Polaritons and Their Role in the Enhanced Transmission of Light through Periodic Arrays of Subwavelength Holes in a Metal Film," *Phys. Rev. Lett.*, vol. 92, no. 10, pp. 107 401/1–4, 2004.

[21] J. Dai, J. Zhang, W. Zhang, and D. Grischkowsky, "Terahertz time-domain spectroscopy characterization of the far-infrared absorption and index of refraction of high-resistivity, float-zone silicon," *J. Opt. Soc. Am. B*, vol. 21, no. 7, pp. 1379–86, 2004.

[22] A. D. Rakić, A. B. Djurišić, J. M. Elazar, and M. L. Majewski, "Optical properties of metallic films for vertical-cavity optoelectronic devices," *Appl. Opt.*, vol. 37, no. 22, pp. 5271–83, 1998.

[23] Y. Yuan, C. Bingham, T. Tyler, S. Palit, T. H. Hand, W. J. Padilla, D. R. Smith, N. M. Jokerst, and S. A. Cummer, "Dual-band planar electric metamaterial in the terahertz regime," *Opt. Exp.*, vol. 16, no. 13, pp. 9746–52, 2008.

[24] W. Zhang, "Resonant terahertz transmission in plasmonic arrays of subwavelength holes," *Eur. Phys. J. Appl. Phys.*, vol. 43, pp. 1–18, 2008.

[25] A. K. Azad, Y. Zhao, W. Zhang, and M. He, "Effect of dielectric properties of metals on terahertz transmission in subwavelength hole arrays," *Opt. Lett.*, vol. 31, no. 17, pp. 2637–9, 2006.

[26] K. B. Crozier, A. Sundaramurthy, G. S. Kino, and C. F. Quate, "Optical antennas: Resonators for local field enhancement," *J. Appl. Phys.*, vol. 94, no. 7, pp. 4632–42, 2003.

[27] P. Gay-Balmaz and O. J. F. Martin, "Electromagnetic resonances in individual and coupled split-ring resonators," *J. Appl. Phys.*, vol. 92, no. 5, pp. 2929–36, 2002.

[28] R. Singh, A. K. Azad, J. F. O'Hara, A. J. Taylor, and W. Zhang, "Effect of metal permittivity on resonant properties of terahertz metamaterials," *Opt. Lett.*, vol. 33, no. 13, pp. 1506–8, 2008.

[29] K. J. Chau and A. Y. Elezzabi, "Terahertz transmission through ensembles of subwavelength-size metallic particles," *Phys. Rev. B*, vol. 72, no. 7, pp. 075 110/1–9, 2005.

Chapter 6

A Study of Photonic Anisotropic Magnetoresistance

In light of the previous chapter's results, it is pertinent to revisit the AMR experiments done with subwavelength ferromagnetic microparticles back in 2006 [1] and 2007 [2]. Specifically, the transparency of a dense ensemble of spherical Ni microparticles will be studied under the influence of an applied magnetic field using THz-TDS. It is expected that this ensemble will show a magnetic field orientation dependent anisotropy in the amplitude and arrival time of the transmitted THz waveform. Conducting this experiment will provide verification for the operation of the new THz-TDS system described in Chapter 2 as well as the experimental technique utilized. Finally, the effect of increasing the index of refraction of the particle ensemble host medium on the observed AMR effect will be studied. The purpose of this experiment is to investigate the relation between the magnitude of the induced current densities on the particles and the observed AMR effect.

6.1 Results and Discussion

To begin with, the transparency of a 1 mm thick ensemble of Ni particles is studied under the influence of an applied magnetic field. Figure 6.1.0.1 shows a SEM image of the Ni particles under investigation. The magnetic field is

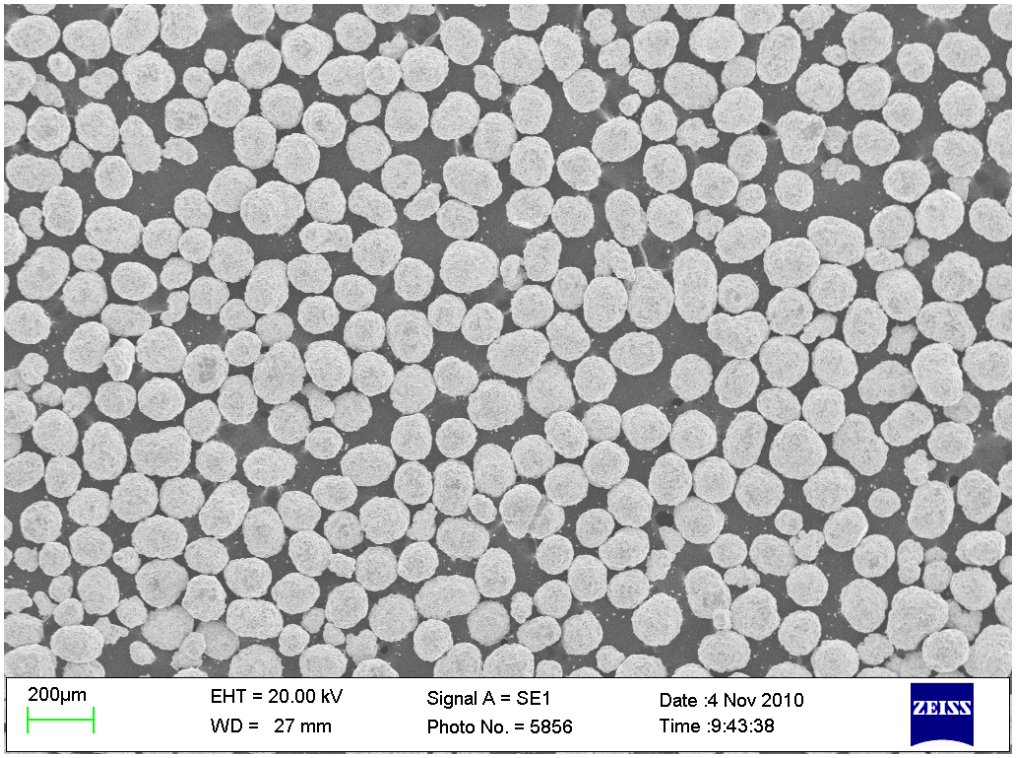

Figure 6.1.0.1: SEM image of the Ni particles. Their mean diameter is 146 ± 9 µm

applied both parallel and perpendicular to the electric field polarization while the field strength is adjusted between 0 and 500 mT. Figure 6.1.0.2 depicts the peak value of the electric field amplitude and the relative delay of the THz waveform transmitted through the sample for both orientations of the applied magnetic field. The magnetic field is first applied perpendicular to the THz electric field polarization. Following this, the polarization of the THz electric field is rotated by 90° such that it is parallel to the applied magnetic field, and the experiment is repeated. As is evidenced by Figure 6.1.0.2, the transmitted

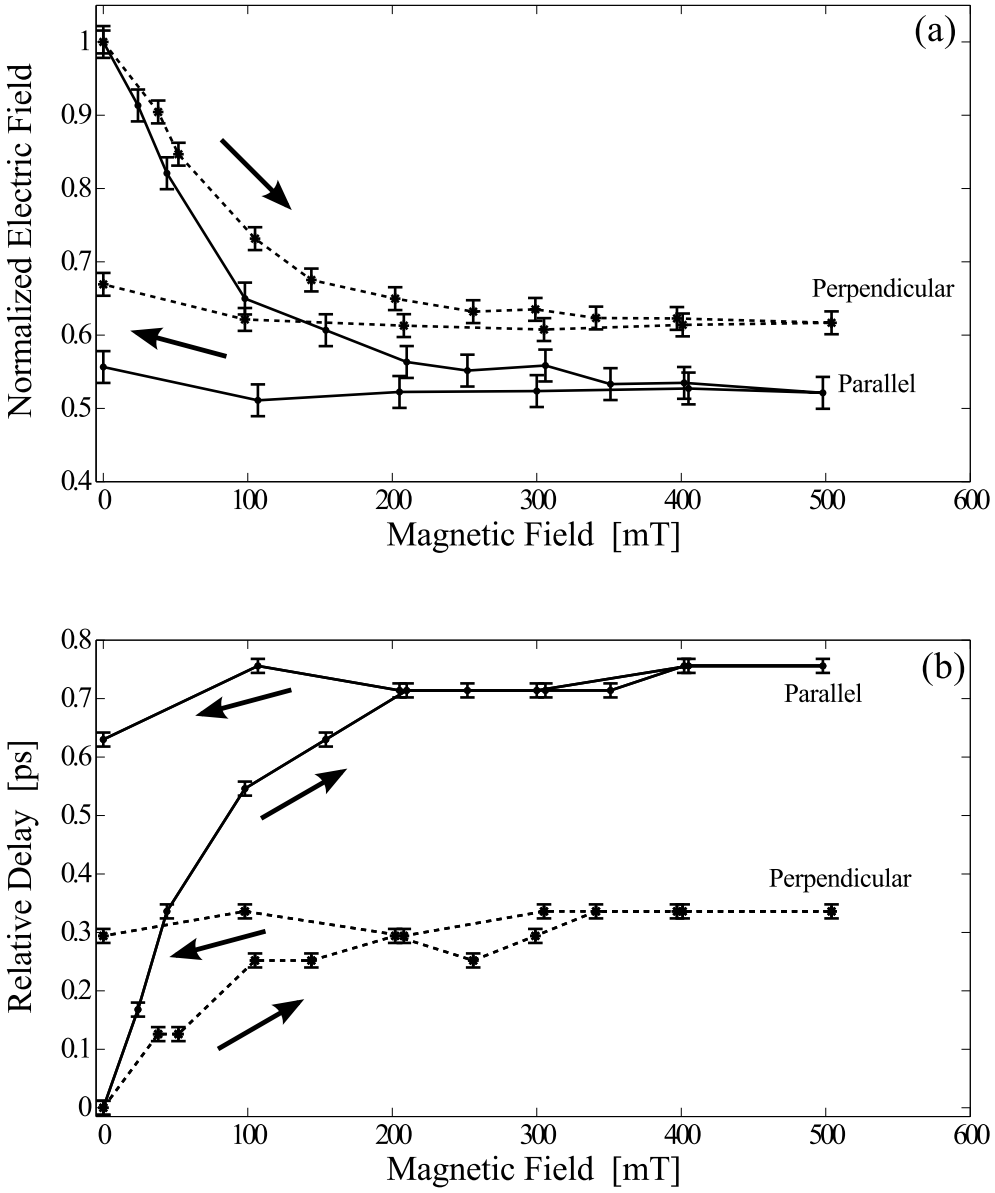

Figure 6.1.0.2: Peak electric field (a) and relative delay (b) of the THz waveform transmitted through the ensemble of Ni particles. The asterisks represent the case where the electric field is polarized perpendicular to the applied magnetic field and the dots represent the case when the fields are parallel to one another.

THz waveform experiences significant amplitude attenuation and arrival delay up to an applied field of about 200 mT regardless of the relative orientation between the THz electric field and applied magnetic field. For applied fields in excess of 200 mT the effect saturates. Note that the data points are normalized to the zero-field case. In this scenario there are two contributions to the change in transparency caused by a change of resistivity in the constituent particles: the ordinary magnetoresistance and AMR effects. As discussed in Chapter 1, the resistance change caused by ordinary magnetoresistance is an order of magnitude smaller than that caused by AMR, so it is expected that AMR is the dominant contributor to the resistance change in this situation. This explains why the attenuation of the transmitted THz waveform is greater when a magnetic field is applied parallel to the THz electric field polarization, since the AMR effect is at a maximum in this configuration. However, when the magnetic field is applied perpendicular to the THz electric field the AMR effect is at a minimum, but significant attenuation and arrival delay of the transmitted THz waveform is still observed. It is important to note that this analysis assumes that the THz electric field is purely linearly polarized and that the currents generated on the surface of the particles are parallel to this polarization. As was shown in Chapter 2, the THz radiation generated by the experimental THz-TDS system is not perfectly linearly polarized; it contains a cross-polarized component of $\sim 15\%$. Therefore, even when the magnetic field is applied perpendicular to the dominant component of the THz electric field, there will still be significant components of the induced surface currents along the applied magnetic field. These components will experience an increased resistivity due to the AMR effect resulting in attenuation and delay of the transmitted THz waveform.

To quantify the observed anisotropy the attenuation and temporal delay

of the transmitted THz waveform for both configurations of the fields can be compared. These quantities are defined here as

$$\Delta\tau = \left(\frac{\tau_{\parallel} - \tau_{\perp}}{\tau_{\parallel}}\right) \times 100 \tag{6.1.0.1a}$$

$$\Delta E_{THz} = \left(\frac{E_{THz,\perp} - E_{THz,\parallel}}{E_{THz,\perp}}\right) \times 100 \tag{6.1.0.1b}$$

where the subscripts $\parallel$ and $\perp$ correspond to the relative orientation of the dominant component of the THz electric field and the applied magnetic field. Equation (6.1.0.1a) uses the relative delay to calculate the anisotropy quantity while equation (6.1.0.1b) uses the peak electric field of the transmitted waveform. Here, the values of τ and E_{THz} for an applied field of 500 mT are used, resulting in $\Delta\tau = 55.6\%$ and $\Delta E_{THz} = 15.5\%$.

In the previous chapter an explanation was given for why the transparency of the particle ensembles exhibit a magnetic field dependence but the planar metallic resonators do not. It was hypothesized that because the interaction of the electric fields confined between adjacent particles occurs in the near-field significantly higher current densities will be generated compared to the case of the planar resonators. This results in a much higher sensitivity to changes in the resistivity of the constituent particles, hence why the effect of magnetoresistance substantially alters the transparency of these ensembles. One way to test this experimentally is to place an ensemble of particles in a higher index medium such that the near-field interaction is quenched, significantly reducing the current density generated on the particles. Essentially, the wavelength of the confined electric fields will be reduced by a factor of $\tilde{n}$ such that the apparent spacing between adjacent particles increases. Since the electric field amplitude falls off as $1/r^3$ in the near-field [3], where r is the distance from the source, this apparent increase in spacing will greatly reduce the coupling between adjacent particles in the ensemble. This in turn results in a reduction of

the current densities generated on the particles meaning that the transparency of the ensemble will be less sensitive to small changes in the resistivity of the particles. To confirm this, a dense ensemble of Ni particles $\sim$ 1 mm thick was placed in optical adhesive (Norland Optical Adhesive 68, $\tilde{n} = 1.54$) and cured, and the transparency under the influence of a magnetic field was tested with the THz-TDS system of Chapter 2. Figure 6.1.0.3 depicts the THz time-domain waveforms transmitted through the sample for both orientations of the magnetic field with respect to the THz electric field. As expected, the

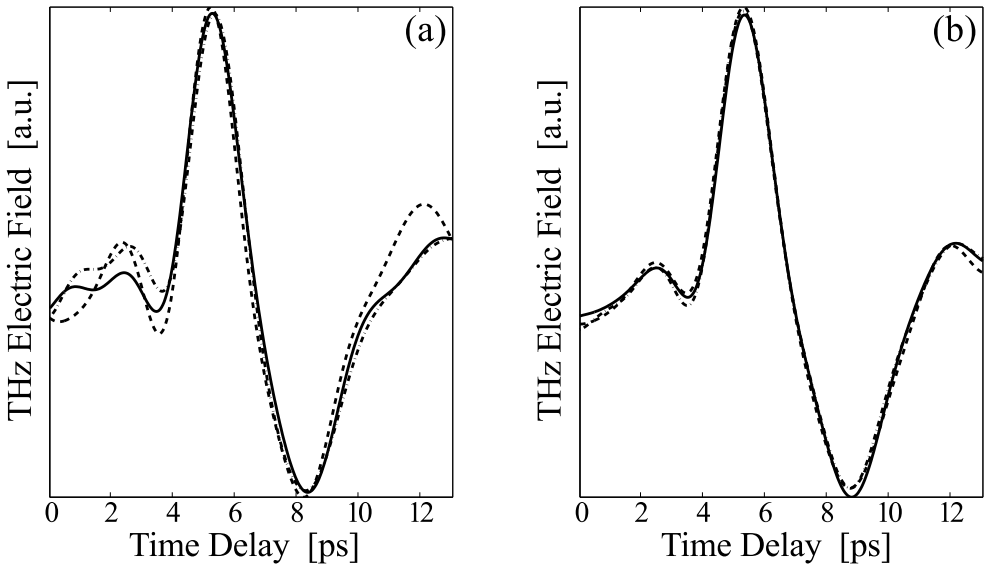

Figure 6.1.0.3: Transmitted THz waveforms for a Ni particle ensemble in optical adhesive at 0 mT (solid), 250 mT (dashed) and 500 mT (dash-dot). The magnetic field is applied perpendicular (a) and parallel (b) to the THz electric field.

transparency of the ensemble shows practically no dependence on the applied magnetic field as evidenced by the lack of change in the arrival time and peak electric field of the transmitted waveforms. This means that the ensemble has been rendered insensitive to small changes in the resistivity. Furthermore, this fact can be directly attributed to the presence of the higher index optical adhesive, which effectively reduces the current density generated on the surface of the particles.

6.2 Conclusion

In conclusion, photonic AMR in a dense ensemble of Ni microparticles was studied. It was found that the transparency of the ensemble was sensitive to both the magnitude and relative orientation of an applied magnetic field with respect to the incident THz electric field. A significant increase in both the attenuation and relative delay of the transmitted THz waveform was observed regardless of the orientation of the applied magnetic field. However, when it was parallel to the THz electric field both the attenuation and delay were larger than in the perpendicular case, which is indicative of an AMR effect. These results were expected based on the original experiments involving the photonic AMR effect. To gain a further understanding of this photonic AMR effect, a dense ensemble of Ni particles was placed in optical adhesive and cured. Interestingly, this ensemble did not show any change in transparency with the application of a magnetic field. This was attributed to a decrease in the current densities generated on the particles, which was caused by higher confinement of the electric fields to the surfaces of the particles effectively reducing the near-field coupling of adjacent localized plasmon modes.

Chapter 6 References

[1] K. J. Chau and A. Y. Elezzabi, "Photonic Anisotropic Magnetoresistance in Dense Co Particle Ensembles," *Phys. Rev. Lett.*, vol. 96, no. 3, pp. 033 903/1–4, 2006.

[2] K. J. Chau, C. A. Baron, and A. Y. Elezzabi, "Isotropic photonic magnetoresistance," *Appl. Phys. Lett.*, vol. 90, no. 12, pp. 121 122/1–3, 2007.

[3] J. D. Jackson, *Classical Electrodynamics*, 3rd ed. New York, NY: John Wiley & Sons, 1999.

Chapter 7

Summary

In Chapter 2, a THz-TDS system incorporating a high field strength electromagnet was designed and constructed. Firstly, an ultrafast laser system based on a Ti:sapphire oscillator was installed and optimized. This system produced ~ 10 fs pulses centered at a wavelength of 794 nm, which were used to both generate and detect THz radiation. Following this, the actual system responsible for generating and detecting ultrafast THz pulses was designed and constructed. A significant challenge for this task was fitting the entire generation and detection scheme within the coils of the electromagnet while keeping everything accessible during an experiment. On top of this, every component of the system had to be made from non-magnetic materials such as aluminum, brass and stainless steel. The final piece of the THz-TDS system implemented was a control GUI created using MATLAB. This program ran the mechanical delay line and acquired the THz time-domain waveform from a lock-in detection scheme.

In Chapter 3, the effect of particle size on the transparency of an ensemble of metallic mircoparticles to incident THz electromagnetic radiation was studied using THz-TDS. The transmission of a THz waveform through a series of

ensembles having constituent particles of a varying, single mean diameter was studied such that the optimum particle size could be determined. An upper limit for the optimum particle size such that the induced localized plasmon modes remain dipolar and energy transport through the ensemble remains efficient was determined from this study.

In Chapter 4, the GMR effect was investigated as a potential candidate for actively modulating the transparency of an ensemble of subwavelength metallic microparticles. Due to the plasmonic nature of the interaction between an incident THz electromagnetic wave and a metallic particle ensemble, it was expected that the induced current densities would interact with a GMR multilayer deposited onto the surface of the particles. A well-studied GMR multilayer based on the pseudo-spin-valve and interlayer exchange coupled configuration was chosen. Three different multilayer structures were deposited onto ensembles of Cu microparticles and their transparency versus an applied magnetic field was monitored. Of the three samples, one exhibited promising preliminary results where the transparency of the ensemble increased with the application of a magnetic field. Further study of this structure is required to map out its full range of functionality in terms of the applied magnetic field. In particular, a new set of samples should be prepared and tested with the setup described in Chapter 2.

In Chapter 5, a series of planar THz plasmonic metamaterials were designed, fabricated and experimentally verified. Furthermore, the magnetoresistance effect was investigated as a potential candidate for actively controlling the electromagnetic response of these structures. Firstly, a 3D FDTD code was implemented to design the structures such that their resonant responses fell within the useable bandwidth of the experimental THz-TDS system. The devices were then fabricated and their passive operation was verified using

the system described in Chapter 2. Active control of the response of these structures was investigated by utilizing the magnetoresistance effect in ferromagnetic Ni; however, no appreciable change from the application of an external magnetic field was observed. This was attributed to an insufficient sensitivity to small changes in resistance of the metal film, which was a result of the current density induced in the structures being too weak. It is possible that a resonator structure exhibiting a higher induced current density (higher Q-factor) in combination with a more significant change in resistivity (i.e. use of a GMR multilayer) would exhibit an observable change in the electromagnetic response. This is a recommended starting point for future work in this area.

In Chapter 6, a previous experiment based on modulating the transparency of an ensemble of ferromagnetic metallic microparticles to incident THz radiation was re-visited. Using THz-TDS it was shown that an applied magnetic field could modulate the transparency of the ensemble as a result of the AMR effect in the ferromagnetic particles. The results were found to agree with previous experiments. Also, it was shown that the effect of AMR on the ensemble could be suppressed by increasing the refractive index of the host medium in which the particles are held. This result was attributed to a reduction in the induced current densities on the particles causing the ensemble to become insensitive to small changes in the resistivity of the constituent particles.

Appendices

Appendix A: Variable Field Strength Permanent Magnet System

The differential stage implemented for the permanent magnet setup used during the study of the GMR structures in Chaper 4 is depicted in Figure A.1. Rotating the knob on the right-hand side separates the two stages located at the center of the device in the figure. In this way, a permanent magnet can be mounted on each stage and their separation can be adjusted to change the magnetic field strength between them. The drawbacks to such a configuration are threefold: (1) the magnetic field is non-uniform, (2) zero field cannot be achieved and (3) only a single polarity of the field is accessible during an experiment. Figure A.2 depicts the performance of this setup. As the field is increased from its minimum value of $\sim$ 50 mT to its maximum value of $\sim$ 500 mT it becomes increasingly non-uniform across the sample. At the minimum achievable separation, represented by 27 full turns of the adjustment knob, the magnetic field strength varies by $>$ 70 mT from the edge of the sample to its center.

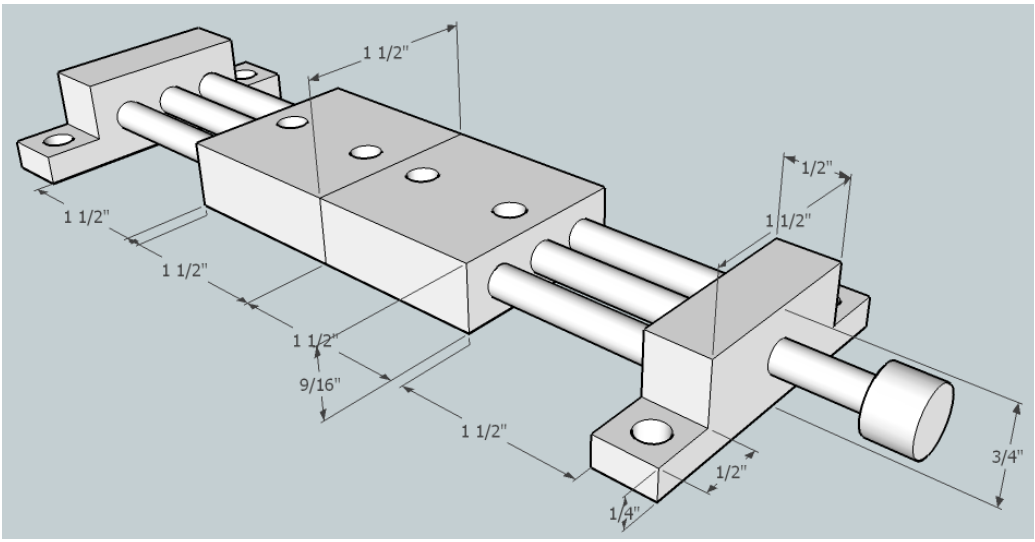

Figure A.1: Differential stage used to create a variable field strength permanent magnet system.

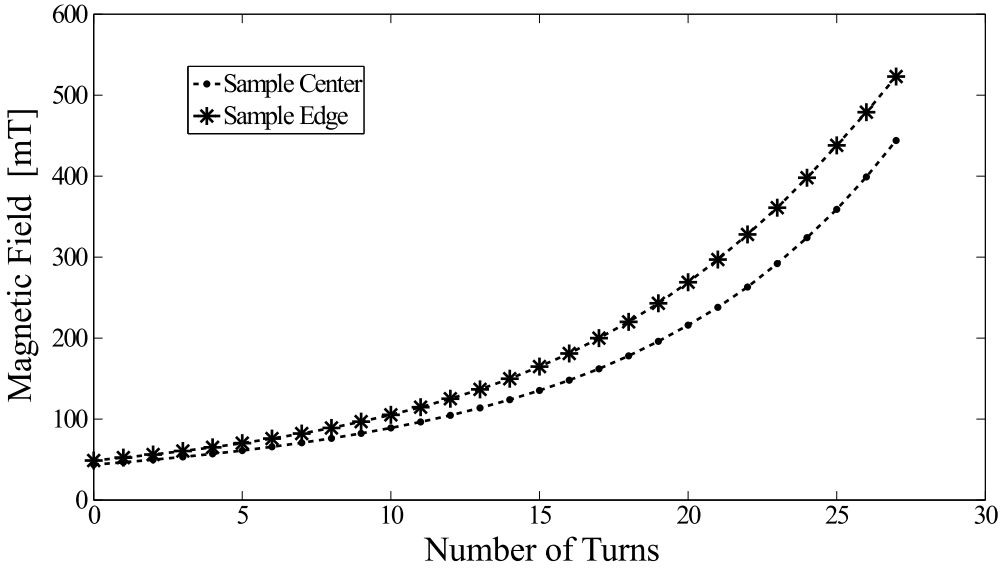

Figure A.2: The magnetic field strength versus the number of full turns to move the permanent magnets closer together. The field is shown at the center of the sample cell as well as its edge.

Appendix B: THz Conductivity of Some Metals

The Drude model for the electric permittivity can be used to find the conductivity of a medium using the following relations first given in Chapter 1

$$\begin{aligned}\tilde{\epsilon}(\omega) &= \epsilon_0\left(1 - \frac{f_0\omega_p^2}{\omega^2 + i\gamma_0\omega}\right) \\ &= \epsilon_0 + i\frac{\tilde{\sigma}(\omega)}{\omega} \\ \tilde{\sigma}(\omega) &= i\epsilon_0\omega\left(\frac{f_0\omega_p^2}{\omega^2 + i\gamma_0\omega}\right)\end{aligned} \tag{B.1}$$

Parameters for f_0, ω_p and γ_0 can be found in [1], but are summarized for the metals discussed in this thesis work in Table B.1. Figure B.1 plots the real

Metal	f_0	ω_p	γ
Au	0.760	9.03 eV	0.053 eV
Cu	0.575	10.83 eV	0.030 eV
Ni	0.096	15.92 eV	0.048 eV
Ti	0.148	7.29 eV	0.082 eV

Table B.1: Parameters for the Drude model for Au, Cu, Ni and Ti.

and imaginary parts of the complex conductivity for these metals over the bandwidth of the experimental system described in Chapter 2 (0.1 - 1.4 THz).

An important quantity related to the conductivity of a material is the absorption skin depth. This quantity determines how far the electric field of an electromagnetic wave penetrates into a given material. Its governing relation is given by

$$\delta_{skin} = \sqrt{\frac{2}{\mu_0\omega\mathrm{Re}\left[\tilde{\sigma}\right]}} \tag{B.2}$$

This relation is plotted in Figure B.2 in the range of 0.1 - 1.4 THz for the metals mentioned above.

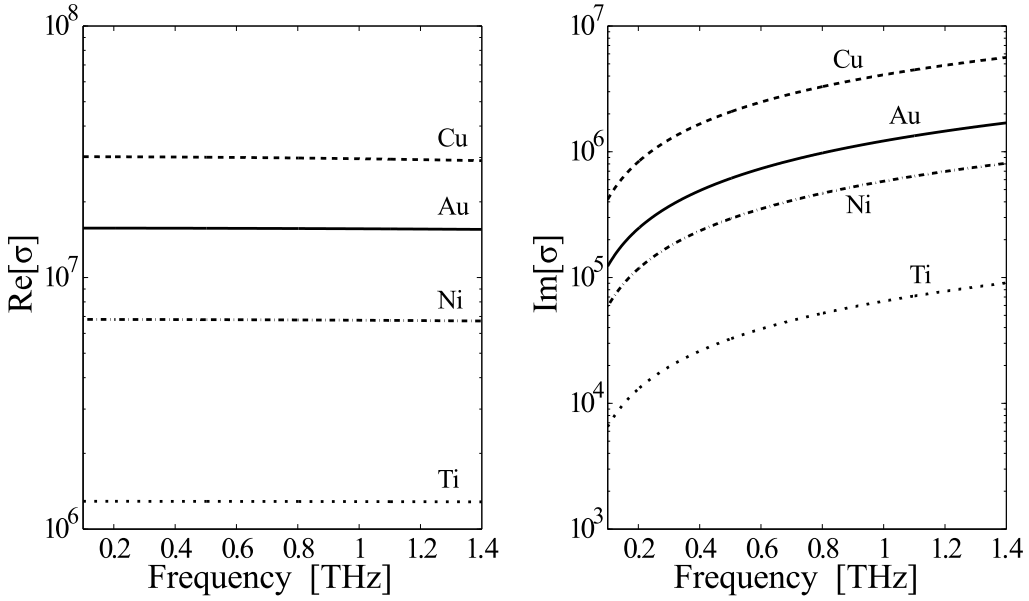

Figure B.1: Real and imaginary parts of the complex conductivity at THz frequencies for Au (solid), Cu (dashed), Ni (dash-dot) and Ti (dotted).

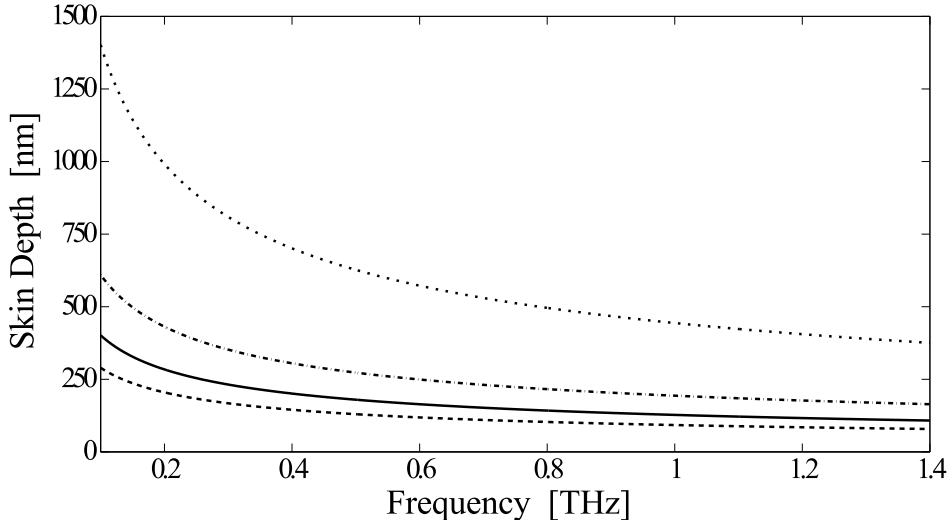

Figure B.2: Absorption skin depth of Au (solid), Cu (dashed), Ni (dash-dot) and Ti (dotted) at THz frequencies.

Appendix C: Photographs of the THz-TDS System

This brief appendix contains a series of photographs of the constructed THz-TDS system described in Chapter 2.

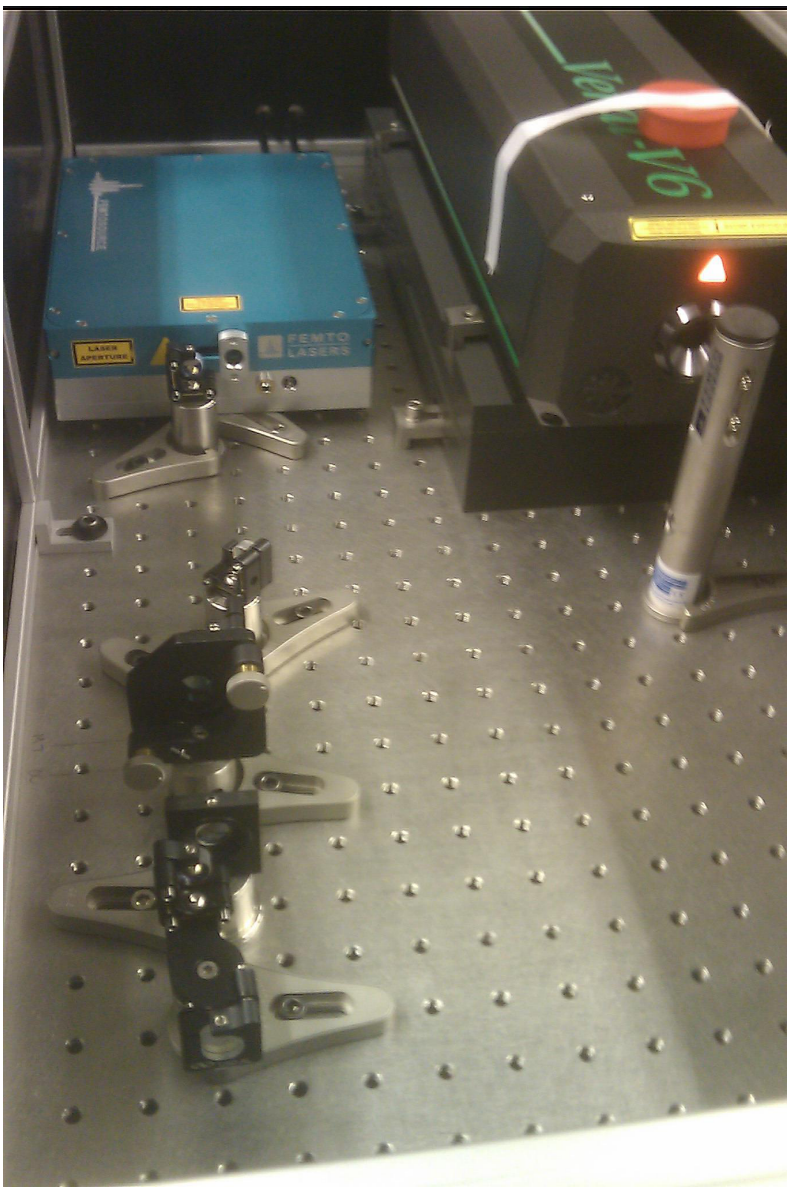

Figure C.1: Femtosecond laser system with the Verdi V6 pump laser on the right and the Femtolasers Ti:Sapphire oscillator on the left (blue box).

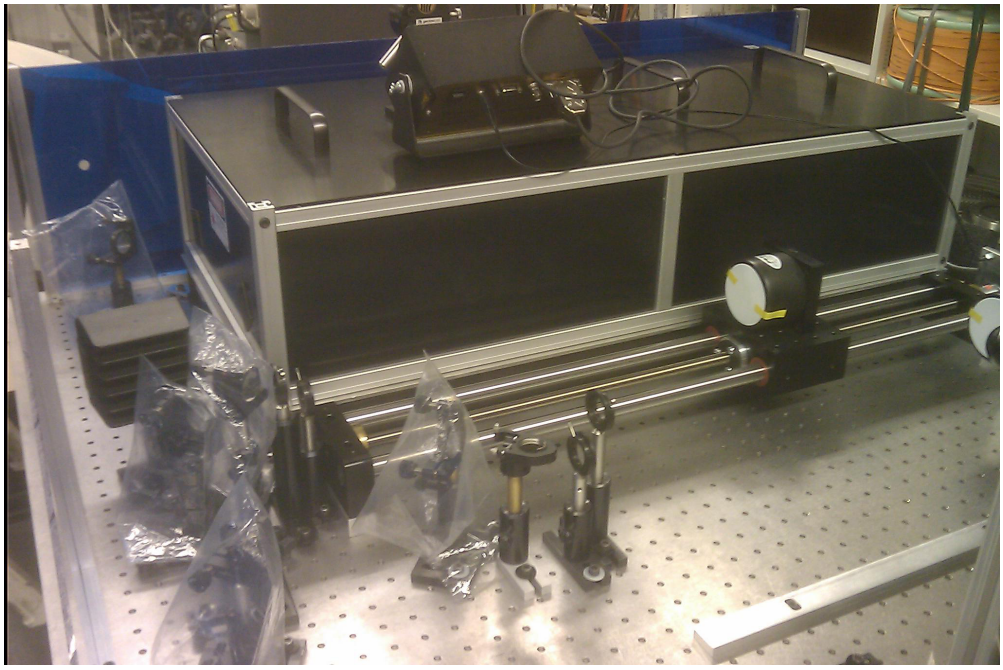

Figure C.2: Laser enclosure and delay line.

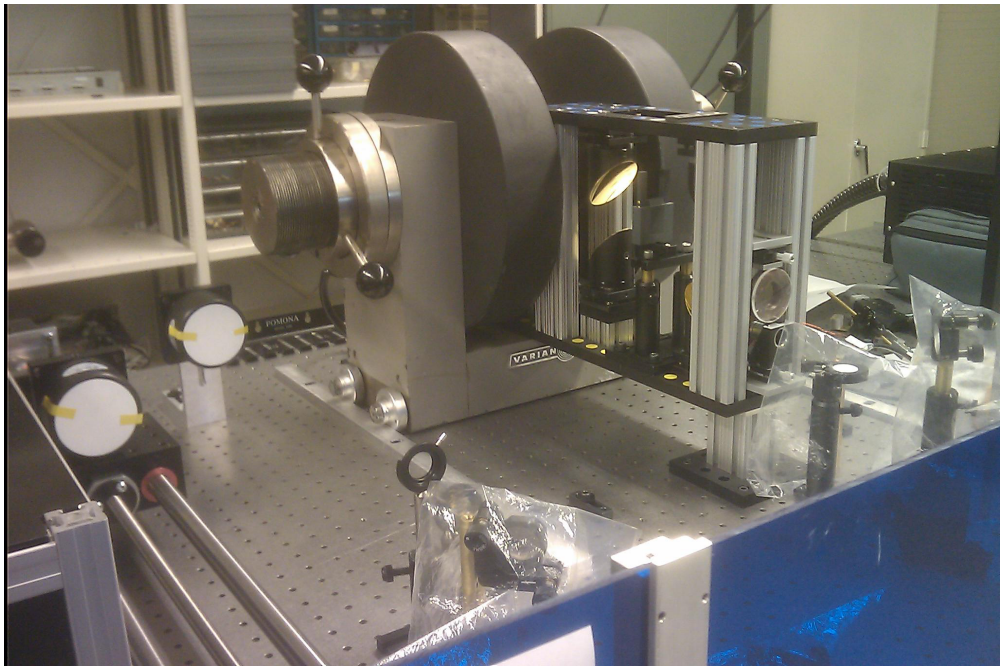

Figure C.3: Electromagnet and THz generation and detection stage.

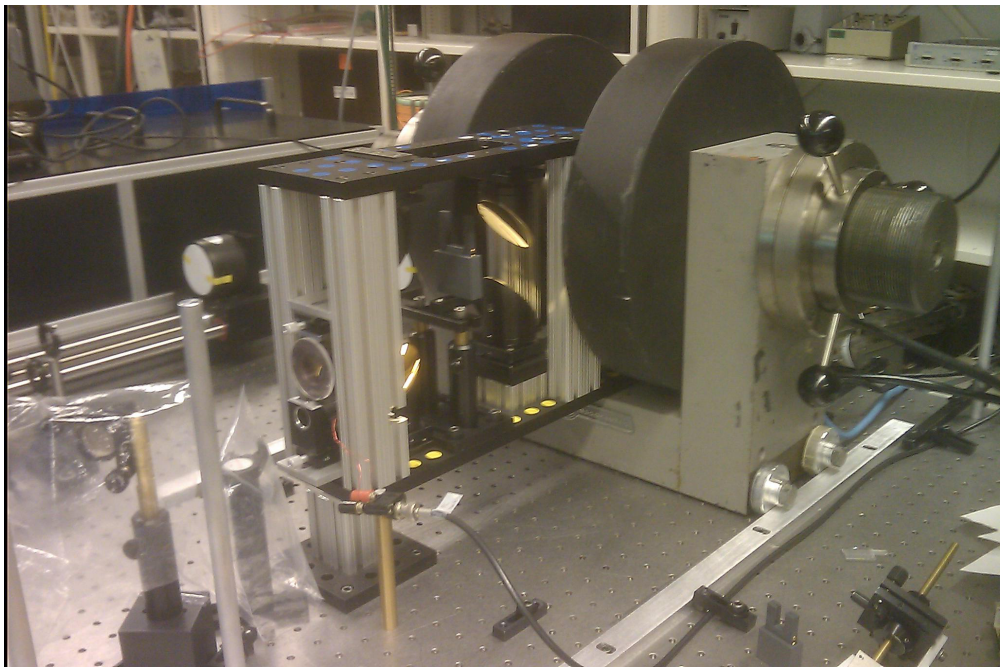

Figure C.4: Another view of the electromagnet and THz generation and detection stage.

Appendix D: 3D Finite-Difference Time-Domain Program

The structures investigated in Chapter 5 were designed with the aid of numerical simulations. These simulations were performed by solving Maxwell's curl equations in linear, isotropic, dispersive, lossy materials using the FDTD method in 3D cartesian space. The Yee discretization scheme [2] is used to find update equations for all six components of the electromagnetic fields on a numerical mesh resulting in a second-order accurate update scheme. Sources are introduced by specifying the values of the electromagnetic fields over a plane of the simulation domain. A more in depth discussion of the FDTD technique and its capabilities can be found in [3].

The form of Maxwell's equations solved in this work is given by

$$\nabla \times \mathbf{E} = -\mu_0 \frac{\partial \mathbf{H}}{\partial \mathrm{t}} + \sigma^* \mathbf{H} \tag{D.1a}$$

$$\nabla \times \mathbf{H} = \epsilon_0 \frac{\partial \mathbf{E}}{\partial \mathrm{t}} + \sigma \mathbf{E} + \mathbf{J}_\mathrm{p} \tag{D.1b}$$

where σ^* and σ represent magnetic and electric loss in the material, respectively, and $\mathbf{J}_\mathrm{p}$ is the electric polarization current density. Material dispersion is included in the simulations by means of the auxiliary differential equation (ADE) method and is represented using the Drude model for the electric permittivity with parameters taken from [1]. This model results in the following equation for $\mathbf{J}_\mathrm{p}$ in the frequency-domain [3]

$$\breve{\mathbf{J}}_\mathrm{p} = -i\omega\epsilon_0 \left(\frac{f_0 \omega_p^2}{\omega^2 - i\omega\gamma_0} \right) \breve{\mathbf{E}}$$

where f_0 is the resonance strength, ω_p is the plasma frequency and γ_0 is the characteristic damping rate. With the application of the inverse Fourier trans-

form, and a single integration with respect to time, the corresponding ADE is found [3]

$$\frac{\partial \mathbf{J}_{\mathrm{p}}}{\partial \mathrm{t}} + \gamma_0 \mathbf{J}_{\mathrm{p}} = \epsilon_0 f_0 \omega_p^2 \mathbf{E} \tag{D.2}$$

The program used to implement the FDTD simulations is written in FORTRAN and can be viewed below. To improve the usability of the program, an interface block is included to provide access to a set of simple FORTRAN functions used to place geometrical objects of a specified material into the simulation space. This greatly reduces the amount of work required in constructing the geometries under investigation.

FDTD3D_DRUDE_PBC.f

```
PROGRAM FDTD3D_DRUDE_PBC
!~~~~~~~~~~~~~~~~~~~~~~~~~~~~~~~~~~~~~~~~~~~~~~~~~~~~~~~~~~~~~~~~~~~~~~~~~~~~
!
! This program numerically solves Maxwell's curl equations in three-
! dimensional source-free space. A perfectly matched layer boundary
! condition is placed at z_min and z_max while the x- and y-axis
! boundaries are periodic. Linear, isotropic, dispersive and lossy
! materials can be modelled. A Drude model is implemented using
! the auxiliary differential equation method to represent the
! dispersive properties of metals.
!
! A very simple CAD environment is also included such that simple
! shapes of a specified material can be added to the simulation
! space. These functions are placed in a separate file (SHAPES.f)
! and included via an interface block.
!
! The perfectly matched layer is implemented using the CPML
! formulation. The CPML implementation is based on that
! (fdtd3D_CPML.f90) written by Jamesina J. Simpson, Assistant
! Professor at the University of New Mexico, Copyright 2005. Prof.
! Simpson's code can be found at the Artech House website under
! the supplementary material for the textbook written by Taflove and
! and Hagness - Computational Electrodynamics: The Finite-Difference
! Time-Domain Method, 3 ed.
!
! Cameron J. E. Straatsma
! MSc Student
! Electrical and Computer Engineering Department
! University of Alberta
! Edmonton, AB  T6G 2V4
! Canada
!
!~~~~~~~~~~~~~~~~~~~~~~~~~~~~~~~~~~~~~~~~~~~~~~~~~~~~~~~~~~~~~~~~~~~~~~~~~~~~

    IMPLICIT NONE

    ! Include interface for external functions
    INTERFACE
        SUBROUTINE cube(center,length,mat_index,grid)
```

```
            INTEGER, DIMENSION(3), INTENT(IN) :: &
                center, length
            INTEGER, INTENT(IN) :: mat_index
            INTEGER, DIMENSION(:,:,:), INTENT(INOUT) :: grid
        END SUBROUTINE cube

        SUBROUTINE sphere(center,radius,mat_index,grid)
            INTEGER, DIMENSION(3), INTENT(IN) :: &
                center
            INTEGER, INTENT(IN) :: &
                radius, mat_index
            INTEGER, DIMENSION(:,:,:), INTENT(INOUT) :: grid
        END SUBROUTINE sphere

        SUBROUTINE cylinder(center,length,orientation,radius, &
            mat_index,grid)
            INTEGER, DIMENSION(3), INTENT(IN) :: &
                center
            INTEGER, INTENT(IN) :: &
                length, radius, mat_index
            CHARACTER, INTENT(IN) :: orientation
            INTEGER, DIMENSION(:,:,:), INTENT(INOUT) :: grid
        END SUBROUTINE cylinder

        SUBROUTINE polygon2D(orientation,center,length,num_vert, &
            vertices,mat_index,grid)
            INTEGER, INTENT(IN) :: &
                center, length, num_vert, mat_index
            CHARACTER, INTENT(IN) :: orientation
            INTEGER, DIMENSION(2,num_vert), INTENT(IN) :: &
                    vertices
            INTEGER, DIMENSION(:,:,:), INTENT(INOUT) :: grid
        END SUBROUTINE polygon2D
    END INTERFACE

!~~~~~~~~~~~~~~~~~~~~~~~~~~~~~~~~~~~~~~~~~~~~~~~~~~~~~~~~~~~~~~~~~~~~~~~~~~~
! Set general simulation parameters
!~~~~~~~~~~~~~~~~~~~~~~~~~~~~~~~~~~~~~~~~~~~~~~~~~~~~~~~~~~~~~~~~~~~~~~~~~~~

    ! Define fundamental constants (MKS units)
    REAL, PARAMETER :: &
        PI = 3.14159265358979323846264338327950288419e0, &
        C = 2.99792458e8, &
        MU_0 = 4.0*PI*1.0e-7, &
        EPS_0 = 1.0/(MU_0*C**2), &
        E = 1.602176487e-19, &
        H = 6.62606896e-34, &
        H_BAR = H/(2.0*PI)

    ! Define size of simulation space and maximum # of iterations
    INTEGER, PARAMETER :: &
        Nx = 300 , &
        Ny = 300 , &
        Nz = 1000, &
        maxiter = 20000

    ! Define mesh size and calculate Courant-stable time step
    REAL, PARAMETER :: &
        delx = 5.0e-7, &
        dely = 5.0e-7, &
        delz = 5.0e-7, &
        dt = 0.99/(C*(1.0/delx**2+1.0/dely**2+ &
            1.0/delz**2)**0.5)

    ! Define thickness of PML regions
    INTEGER, PARAMETER :: &
        NzPML_b = 11, NzPML_t = 11
```

```
    ! Define CPML parameters
    INTEGER, PARAMETER :: &
        m = 4, &
        ma = 2

    REAL, PARAMETER :: &
        sigma_zmax = 0.75*0.8*(m+1)/(delz*(MU_0/EPS_0)**0.5), &
        alpha_zmax = 0.24, &
        kappa_zmax = 15.0

    ! Define TF/SF source boundary location
    INTEGER, PARAMETER :: &
        kstart = NzPML_b+25

    ! Define source parameters

    ! Define center of plane wave
    INTEGER, PARAMETER :: &
        isrc = (Nx-1)/2, &
        jsrc = (Ny-1)/2, &
        ksrc = kstart

    REAL, PARAMETER :: &
        ! Spatial
        lambda0 = 300.0e-6, &
        k0 = 2.0*PI/lambda0, &
        ! Temporal
        omega0 = 2.0*PI*C/lambda0, &
        tw = 0.35e-12, &
        t0 = 2.0*tw, &
        ! Amplitudes
        ampE = 1.0, &
        ampH = ampE/C

!~~~~~~~~~~~~~~~~~~~~~~~~~~~~~~~~~~~~~~~~~~~~~~~~~~~~~~~~~~~~~~~~~~~~~~~~
! Create dynamic storage for required arrays
!~~~~~~~~~~~~~~~~~~~~~~~~~~~~~~~~~~~~~~~~~~~~~~~~~~~~~~~~~~~~~~~~~~~~~~~~

    ! Create EM field update arrays
    ! Magnetic fields
    REAL, DIMENSION(:,:,:), ALLOCATABLE :: &
        Hx, Hy, Hz

    ! Electric fields
    REAL, DIMENSION(:,:,:,:), ALLOCATABLE :: &
        Ex, Ey, Ez

    ! Electric polarization current densities
    REAL, DIMENSION(:,:,:), ALLOCATABLE :: &
        Jx, Jy, Jz

    ! Create geometry array
    INTEGER, DIMENSION(:,:,:), ALLOCATABLE :: &
     ID

    ! Create standard material property arrays
    REAL, DIMENSION(:,:,:), ALLOCATABLE :: &
        MU_R, SIG_H, &
        EPS_R, SIG_E

    ! Create EM field update coefficient arrays
    REAL, DIMENSION(:,:,:), ALLOCATABLE :: &
        Da, Db, Ca, Cb

    ! Create Drude model property variables
    REAL :: &
        omega_p, str, gamma
```

```
    ! Create Drude model ADE coefficient arrays
    REAL, DIMENSION(:,:,:), ALLOCATABLE :: &
        alpha, beta

    ! Create EM field update denominator arrays
    REAL, DIMENSION(:), ALLOCATABLE :: &
        den_Hx, den_Ex, &
        den_Hy, den_Ey, &
        den_Hz, den_Ez

    ! Create 3D CPML discrete convolution field arrays
    ! x-axis
    REAL, DIMENSION(:,:,:), ALLOCATABLE :: &
        psiHxz_b, psiHxz_t, &
        psiExz_b, psiExz_t

    ! y-axis
    REAL, DIMENSION(:,:,:), ALLOCATABLE :: &
        psiHyz_b, psiHyz_t, &
        psiEyz_b, psiEyz_t

    ! Create CPML discrete convolution field coefficient and
    ! property arrays
    ! z-axis
    REAL, DIMENSION(:), ALLOCATABLE :: &
        bHz_b, cHz_b, sigHz_b, alphaHz_b, kappaHz_b, &
        bHz_t, cHz_t, sigHz_t, alphaHz_t, kappaHz_t, &
        bEz_b, cEz_b, sigEz_b, alphaEz_b, kappaEz_b, &
        bEz_t, cEz_t, sigEz_t, alphaEz_t, kappaEz_t

    ! Define source variable
    REAl :: &
        temporal_src

    ! Define temporary variables for output
    REAL :: &
        incE, reflE, transE

    ! Define array loop variables
    INTEGER :: &
        i, j, k, kPML, n

    ! Define file variables for outputting a plane
    CHARACTER(20) :: &
        step, filenameH, filenameE

    ! Define error checking variables
    INTEGER :: ierr
    CHARACTER(100) :: merr

!~~~~~~~~~~~~~~~~~~~~~~~~~~~~~~~~~~~~~~~~~~~~~~~~~~~~~~~~~~~~~~~~~~~~~~~~~~~~
! Allocate memory for required arrays
!~~~~~~~~~~~~~~~~~~~~~~~~~~~~~~~~~~~~~~~~~~~~~~~~~~~~~~~~~~~~~~~~~~~~~~~~~~~~

    WRITE(*,*) "Allocating required arrays..."
    WRITE(*,*) ""

    ! Allocate EM field update arrays
    ! Magnetic fields
    ALLOCATE(Hx(Nx,Ny-1,Nz-1),STAT=ierr,ERRMSG=merr)
    IF (ierr /= 0) THEN
        WRITE(*,*) "ERROR Hx Allocation: ", merr
        STOP
    ENDIF
    ALLOCATE(Hy(Nx-1,Ny,Nz-1),STAT=ierr,ERRMSG=merr)
    IF (ierr /= 0) THEN
        WRITE(*,*) "ERROR Hy Allocation: ", merr
        STOP
```

```
ENDIF
ALLOCATE(Hz(Nx-1,Ny-1,Nz),STAT=ierr,ERRMSG=merr)
IF (ierr /= 0) THEN
    WRITE(*,*) "ERROR Hz Allocation: ", merr
    STOP
ENDIF

! Electric fields
ALLOCATE(Ex(Nx-1,Ny,Nz,2),STAT=ierr,ERRMSG=merr)
IF (ierr /= 0) THEN
    WRITE(*,*) "ERROR Ex Allocation: ", merr
    STOP
ENDIF
ALLOCATE(Ey(Nx,Ny-1,Nz,2),STAT=ierr,ERRMSG=merr)
IF (ierr /= 0) THEN
    WRITE(*,*) "ERROR Ey Allocation: ", merr
    STOP
ENDIF
ALLOCATE(Ez(Nx,Ny,Nz-1,2),STAT=ierr,ERRMSG=merr)
IF (ierr /= 0) THEN
    WRITE(*,*) "ERROR Ez Allocation: ", merr
    STOP
ENDIF

! Electric polarization current densities
ALLOCATE(Jx(Nx-1,Ny,Nz),STAT=ierr,ERRMSG=merr)
IF (ierr /= 0) THEN
    WRITE(*,*) "ERROR Jx Allocation: ", merr
    STOP
ENDIF
ALLOCATE(Jy(Nx,Ny-1,Nz),STAT=ierr,ERRMSG=merr)
IF (ierr /= 0) THEN
    WRITE(*,*) "ERROR Jy Allocation: ", merr
    STOP
ENDIF
ALLOCATE(Jz(Nx,Ny,Nz-1),STAT=ierr,ERRMSG=merr)
IF (ierr /= 0) THEN
    WRITE(*,*) "ERROR Jz Allocation: ", merr
    STOP
ENDIF

! Allocate geometry array
ALLOCATE(ID(Nx,Ny,Nz),STAT=ierr,ERRMSG=merr)
IF (ierr /= 0) THEN
    WRITE(*,*) "ERROR Geometry Allocation: ", merr
    STOP
ENDIF

! Allocate standard material property arrays
ALLOCATE(MU_R(Nx,Ny,Nz),STAT=ierr,ERRMSG=merr)
IF (ierr /= 0) THEN
    WRITE(*,*) "ERROR Relative Permeability Allocation: ",&
        merr
    STOP
ENDIF
ALLOCATE(SIG_H(Nx,Ny,Nz),STAT=ierr,ERRMSG=merr)
IF (ierr /= 0) THEN
    WRITE(*,*) "ERROR Magnetic Loss Allocation: ", merr
    STOP
ENDIF
ALLOCATE(EPS_R(Nx,Ny,Nz),STAT=ierr,ERRMSG=merr)
IF (ierr /= 0) THEN
    WRITE(*,*) "ERROR Relative Permittivity Allocation: ",&
        merr
    STOP
ENDIF
ALLOCATE(SIG_E(Nx,Ny,Nz),STAT=ierr,ERRMSG=merr)
IF (ierr /= 0) THEN
```

```
    WRITE(*,*) "ERROR Electric Loss Allocation: ", merr
    STOP
ENDIF

! Allocate EM field update coefficient arrays
ALLOCATE(Da(Nx,Ny,Nz),STAT=ierr,ERRMSG=merr)
IF (ierr /= 0) THEN
    WRITE(*,*) "ERROR Coefficient Allocation: ", merr
    STOP
ENDIF
ALLOCATE(Db(Nx,Ny,Nz),STAT=ierr,ERRMSG=merr)
IF (ierr /= 0) THEN
    WRITE(*,*) "ERROR Coefficient Allocation: ", merr
    STOP
ENDIF
ALLOCATE(Ca(Nx,Ny,Nz),STAT=ierr,ERRMSG=merr)
IF (ierr /= 0) THEN
    WRITE(*,*) "ERROR Coefficient Allocation: ", merr
    STOP
ENDIF
ALLOCATE(Cb(Nx,Ny,Nz),STAT=ierr,ERRMSG=merr)
IF (ierr /= 0) THEN
    WRITE(*,*) "ERROR Coefficient Allocation: ", merr
    STOP
ENDIF

! Allocate Drudemodel ADE coefficient arrays
ALLOCATE(alpha(Nx,Ny,Nz),STAT=ierr,ERRMSG=merr)
IF (ierr /= 0) THEN
    WRITE(*,*) "ERROR Drude Model Allocation: ", merr
    STOP
ENDIF
ALLOCATE(beta(Nx,Ny,Nz),STAT=ierr,ERRMSG=merr)
IF (ierr /= 0) THEN
    WRITE(*,*) "ERROR Drude Model Allocation: ", merr
    STOP
ENDIF

! Allocate EM field update denominator arrays
ALLOCATE(den_Hx(Nx-1),den_Ex(Nx-1),STAT=ierr,ERRMSG=merr)
IF (ierr /= 0) THEN
    WRITE(*,*) "ERROR Denominator Allocation: ", merr
    STOP
ENDIF
ALLOCATE(den_Hy(Ny-1),den_Ey(Ny-1),STAT=ierr,ERRMSG=merr)
IF (ierr /= 0) THEN
    WRITE(*,*) "ERROR Denominator Allocation: ", merr
    STOP
ENDIF
ALLOCATE(den_Hz(Nz-1),den_Ez(Nz-1),STAT=ierr,ERRMSG=merr)
IF (ierr /= 0) THEN
    WRITE(*,*) "ERROR Denominator Allocation: ", merr
    STOP
ENDIF

! Allocate 3D CPML discrete convolution field arrays
! x-axis
ALLOCATE(psiHxz_b(Nx,Ny-1,NzPML_b-1),STAT=ierr,ERRMSG=merr)
IF (ierr /= 0) THEN
    WRITE(*,*) "ERROR CPML Allocation: ", merr
    STOP
ENDIF
ALLOCATE(psiHxz_t(Nx,Ny-1,NzPML_t-1),STAT=ierr,ERRMSG=merr)
IF (ierr /= 0) THEN
    WRITE(*,*) "ERROR CPML Allocation: ", merr
    STOP
ENDIF
```

```
ALLOCATE(psiExz_b(Nx-1,Ny,NzPML_b),STAT=ierr,ERRMSG=merr)
IF (ierr /= 0) THEN
    WRITE(*,*) "ERROR CPML Allocation: ", merr
    STOP
ENDIF
ALLOCATE(psiExz_t(Nx-1,Ny,NzPML_t),STAT=ierr,ERRMSG=merr)
IF (ierr /= 0) THEN
    WRITE(*,*) "ERROR CPML Allocation: ", merr
    STOP
ENDIF

! y-axis
ALLOCATE(psiHyz_b(Nx-1,Ny,NzPML_b-1),STAT=ierr,ERRMSG=merr)
IF (ierr /= 0) THEN
    WRITE(*,*) "ERROR CPML Allocation: ", merr
    STOP
ENDIF
ALLOCATE(psiHyz_t(Nx-1,Ny,NzPML_t-1),STAT=ierr,ERRMSG=merr)
IF (ierr /= 0) THEN
    WRITE(*,*) "ERROR CPML Allocation: ", merr
    STOP
ENDIF

ALLOCATE(psiEyz_b(Nx,Ny-1,NzPML_b),STAT=ierr,ERRMSG=merr)
IF (ierr /= 0) THEN
    WRITE(*,*) "ERROR CPML Allocation: ", merr
    STOP
ENDIF
ALLOCATE(psiEyz_t(Nx,Ny-1,NzPML_t),STAT=ierr,ERRMSG=merr)
IF (ierr /= 0) THEN
    WRITE(*,*) "ERROR CPML Allocation: ", merr
    STOP
ENDIF

! Allocate CPML discrete convolution field coefficient and
! property arrays
! z-axis
ALLOCATE(bHz_b(NzPML_b-1),cHz_b(NzPML_b-1),STAT=ierr,ERRMSG=merr)
IF (ierr /= 0) THEN
    WRITE(*,*) "ERROR CPML Allocation: ", merr
    STOP
ENDIF
ALLOCATE(sigHz_b(NzPML_b-1),alphaHz_b(NzPML_b-1), &
    kappaHz_b(NzPML_b-1),STAT=ierr,ERRMSG=merr)
IF (ierr /= 0) THEN
    WRITE(*,*) "ERROR CPML Allocation: ", merr
    STOP
ENDIF
ALLOCATE(bHz_t(NzPML_t-1),cHz_t(NzPML_t-1),STAT=ierr,ERRMSG=merr)
IF (ierr /= 0) THEN
    WRITE(*,*) "ERROR CPML Allocation: ", merr
    STOP
ENDIF
ALLOCATE(sigHz_t(NzPML_t-1),alphaHz_t(NzPML_t-1), &
    kappaHz_t(NzPML_t-1),STAT=ierr,ERRMSG=merr)
IF (ierr /= 0) THEN
    WRITE(*,*) "ERROR CPML Allocation: ", merr
    STOP
ENDIF

ALLOCATE(bEz_b(NzPML_b),cEz_b(NzPML_b),STAT=ierr,ERRMSG=merr)
IF (ierr /= 0) THEN
    WRITE(*,*) "ERROR CPML Allocation: ", merr
    STOP
ENDIF
ALLOCATE(sigEz_b(NzPML_b),alphaEz_b(NzPML_b), &
    kappaEz_b(NzPML_b),STAT=ierr,ERRMSG=merr)
IF (ierr /= 0) THEN
```

```
        WRITE(*,*) "ERROR CPML Allocation: ", merr
        STOP
    ENDIF
    ALLOCATE(bEz_t(NzPML_t),cEz_t(NzPML_t),STAT=ierr,ERRMSG=merr)
    IF (ierr /= 0) THEN
        WRITE(*,*) "ERROR CPML Allocation: ", merr
        STOP
    ENDIF
    ALLOCATE(sigEz_t(NzPML_t),alphaEz_t(NzPML_t), &
        kappaEz_t(NzPML_t),STAT=ierr,ERRMSG=merr)
    IF (ierr /= 0) THEN
        WRITE(*,*) "ERROR CPML Allocation: ", merr
        STOP
    ENDIF

    WRITE(*,*) "Arrays allocated successfully"
    WRITE(*,*) ""

!~~~~~~~~~~~~~~~~~~~~~~~~~~~~~~~~~~~~~~~~~~~~~~~~~~~~~~~~~~~~~~~~~~~~~~~~~~~
! Open output files
!~~~~~~~~~~~~~~~~~~~~~~~~~~~~~~~~~~~~~~~~~~~~~~~~~~~~~~~~~~~~~~~~~~~~~~~~~~~

    OPEN (UNIT = 30, FILE = "Hx.txt")
    OPEN (UNIT = 31, FILE = "Hy.txt")
    OPEN (UNIT = 32, FILE = "Hz.txt")

    OPEN (UNIT = 33, FILE = "Ex.txt")
    OPEN (UNIT = 34, FILE = "Ey.txt")
    OPEN (UNIT = 35, FILE = "Ez.txt")

    OPEN (UNIT = 40, FILE = "incE.txt")
    OPEN (UNIT = 41, FILE = "reflE.txt")
    OPEN (UNIT = 42, FILE = "transE.txt")

!~~~~~~~~~~~~~~~~~~~~~~~~~~~~~~~~~~~~~~~~~~~~~~~~~~~~~~~~~~~~~~~~~~~~~~~~~~~
! Initialize simulation
!~~~~~~~~~~~~~~~~~~~~~~~~~~~~~~~~~~~~~~~~~~~~~~~~~~~~~~~~~~~~~~~~~~~~~~~~~~~

    ! EM fields
    Hx(:,:,:) = 0.0
    Hy(:,:,:) = 0.0
    Hz(:,:,:) = 0.0

    Ex(:,:,:,:) = 0.0
    Ey(:,:,:,:) = 0.0
    Ez(:,:,:,:) = 0.0

    Jx(:,:,:) = 0.0
    Jy(:,:,:) = 0.0
    Jz(:,:,:) = 0.0

    ! 3D CPML discrete convolution fields
    ! x-axis
    psiHxz_b(:,:,:) = 0.0
    psiHxz_t(:,:,:) = 0.0
    psiExz_b(:,:,:) = 0.0
    psiExz_t(:,:,:) = 0.0

    ! y-axis
    psiHyz_b(:,:,:) = 0.0
    psiHyz_t(:,:,:) = 0.0
    psiEyz_b(:,:,:) = 0.0
    psiEyz_t(:,:,:) = 0.0

    ! Field update coefficient arrays
    Da(:,:,:) = 0.0
    Db(:,:,:) = 0.0
    Ca(:,:,:) = 0.0
```

```
    Cb(:,:,:) = 0.0

    alpha(:,:,:) = 0.0
    beta(:,:,:) = 0.0

    ! Material property arrays
    MU_R(:,:,:) = 0.0
    SIG_H(:,:,:) = 0.0
    EPS_R(:,:,:) = 0.0
    SIG_E(:,:,:) = 0.0

    omega_p = 0.0
    str = 0.0
    gamma = 0.0

    ! Set background material to vacuum
    ID(:,:,:) = 0

!~~~~~~~~~~~~~~~~~~~~~~~~~~~~~~~~~~~~~~~~~~~~~~~~~~~~~~~~~~~~~~~~~~~~~~~~
! Set material identifcation matrix
!~~~~~~~~~~~~~~~~~~~~~~~~~~~~~~~~~~~~~~~~~~~~~~~~~~~~~~~~~~~~~~~~~~~~~~~~

    WRITE(*,*) "Constructing geometry..."
    WRITE(*,*) ""

! ~~~~~~~~~~~~~~~~~~~~~~~~~~~~~~~~~~~~~~~~~~~~~~~~~~~~~~~~~~~~~~~~~~~~~~~~
! The subroutines to insert shapes into the simulation space are as
! follows:
!
! cube(center,length,mat_index,grid)
! sphere(center,radius,mat_index,grid)
! cylinder(center,length,orientation,radius,mat_index,grid)
! polygon2D(orientation,center,length,num_vert,vertices,
!       mat_index,grid)
!
! ~~~~~~~~~~~~~~~~~~~~~~~~~~~~~~~~~~~~~~~~~~~~~~~~~~~~~~~~~~~~~~~~~~~~~~~~

    ! Set material for the simulation space


    ! Output a slice of the geometry
    OPEN(UNIT = 36, FILE = "geometry_xy.txt")
    OPEN(UNIT = 37, FILE = "geometry_xz.txt")
    OPEN(UNIT = 38, FILE = "geometry_yz.txt")
    ! xy-plane
    DO j = 1, Ny
        DO i = 1, Nx
            WRITE(36,*) ID(i,j,500)
        ENDDO
    ENDDO
    ! xz-plane
    DO k = 1, Nz
        DO i = 1, Nx
            WRITE(37,*) ID(i,Ny/2,k)
        ENDDO
    ENDDO
    ! yz-plane
    DO k = 1, Nz
        DO j = 1, Ny
            WRITE(38,*) ID(Nx/2,j,k)
        ENDDO
    ENDDO
    CLOSE(UNIT = 36)
    CLOSE(UNIT = 37)
    CLOSE(UNIT = 38)

!~~~~~~~~~~~~~~~~~~~~~~~~~~~~~~~~~~~~~~~~~~~~~~~~~~~~~~~~~~~~~~~~~~~~~~~~
! Set material dependent parameters using ID matrix
```

```
!
! Dispersive materials are implemented using a Drude model.
! The coefficients are taken from the following paper:
!
!   A. D. Rakic et al., "Optical properties of metallic films
!       for vertical-cavity optoelectronics devices," Appl.
!       Opt., v. 37, n. 22, pp. 5271-83 (1998)
!~~~~~~~~~~~~~~~~~~~~~~~~~~~~~~~~~~~~~~~~~~~~~~~~~~~~~~~~~~~~~~~~~~~~~~~~

    DO k = 1, Nz
        DO i = 1, Nx
            DO j = 1, Ny
                SELECT CASE (ID(i,j,k))

                CASE(0) ! vacuum
                    MU_R(i,j,k) = 1.0
                    SIG_H(i,j,k) = 0.0
                    EPS_R(i,j,k) = 1.0
                    SIG_E(i,j,k) = 0.0
                    ! Set EM field update coefficients
                    Da(i,j,k) = (2.0*MU_R(i,j,k)*MU_0- &
                        SIG_H(i,j,k)*dt)/(2.0*MU_R(i,j,k)*MU_0+ &
                        SIG_H(i,j,k)*dt)
                    Db(i,j,k) = (2.0*dt)/(2.0*MU_R(i,j,k)*MU_0+ &
                        SIG_H(i,j,k)*dt)
                    Ca(i,j,k) = (2.0*EPS_R(i,j,k)*EPS_0- &
                        SIG_E(i,j,k)*dt)/(2.0*EPS_R(i,j,k)*EPS_0+ &
                        SIG_E(i,j,k)*dt)
                    Cb(i,j,k) = (2.0*dt)/(2.0*EPS_R(i,j,k)* &
                        EPS_0+SIG_E(i,j,k)*dt)

                CASE(1) ! Perfect electric conductor (PEC)
                    MU_R(i,j,k) = 1.0
                    SIG_H(i,j,k) = 0.0
                    EPS_R(i,j,k) = 1.0
                    SIG_E(i,j,k) = 0.0
                    ! Set EM field update coefficients
                    Da(i,j,k) = (2.0*MU_R(i,j,k)*MU_0- &
                        SIG_H(i,j,k)*dt)/(2.0*MU_R(i,j,k)*MU_0+ &
                        SIG_H(i,j,k)*dt)
                    Db(i,j,k) = (2.0*dt)/(2.0*MU_R(i,j,k)*MU_0+ &
                        SIG_H(i,j,k)*dt)

                CASE(2) ! Perfect magnetic conductor (PMC)
                    MU_R(i,j,k) = 1.0
                    SIG_H(i,j,k) = 0.0
                    EPS_R(i,j,k) = 1.0
                    SIG_E(i,j,k) = 0.0
                    ! Set EM field update coefficients
                    Ca(i,j,k) = (2.0*EPS_R(i,j,k)*EPS_0- &
                        SIG_E(i,j,k)*dt)/(2.0*EPS_R(i,j,k)*EPS_0+ &
                        SIG_E(i,j,k)*dt)
                    Cb(i,j,k) = (2.0*dt)/(2.0*EPS_R(i,j,k)* &
                        EPS_0+SIG_E(i,j,k)*dt)

                CASE(3) ! Dielectric
                    MU_R(i,j,k) = 1.0
                    SIG_H(i,j,k) = 0.0
                    EPS_R(i,j,k) = 11.68
                    SIG_E(i,j,k) = 0.0
                    ! Set EM field update coefficients
                    Da(i,j,k) = (2.0*MU_R(i,j,k)*MU_0- &
                        SIG_H(i,j,k)*dt)/(2.0*MU_R(i,j,k)*MU_0+ &
                        SIG_H(i,j,k)*dt)
                    Db(i,j,k) = (2.0*dt)/(2.0*MU_R(i,j,k)*MU_0+ &
                        SIG_H(i,j,k)*dt)
                    Ca(i,j,k) = (2.0*EPS_R(i,j,k)*EPS_0- &
                        SIG_E(i,j,k)*dt)/(2.0*EPS_R(i,j,k)*EPS_0+ &
```

```
        SIG_E(i,j,k)*dt)
    Cb(i,j,k) = (2.0*dt)/(2.0*EPS_R(i,j,k)* &
        EPS_0+SIG_E(i,j,k)*dt)

CASE(4) ! Silver (Ag)
    MU_R(i,j,k) = 1.0
    SIG_H(i,j,k) = 0.0
    SIG_E(i,j,k) = 0.0
    ! Set dispersive material parameters
    omega_p = 9.01*E/H_BAR
    str = 0.845
    gamma = 0.048*E/H_BAR
    ! Set dispersive material coefficients
    alpha(i,j,k) = (2.0-gamma*dt)/(2.0+gamma*dt)
    beta(i,j,k) = (str*EPS_0*dt*omega_p**2)/ &
        (2.0+gamma*dt)
    ! Set EM field update coefficients
    Da(i,j,k) = (2.0*MU_R(i,j,k)*MU_0- &
        SIG_H(i,j,k)*dt)/(2.0*MU_R(i,j,k)*MU_0+ &
        SIG_H(i,j,k)*dt)
    Db(i,j,k) = (2.0*dt)/(2.0*MU_R(i,j,k)*MU_0+ &
        SIG_H(i,j,k)*dt)
    Ca(i,j,k) = (2.0*EPS_0-dt*beta(i,j,k)- &
        SIG_E(i,j,k)*dt)/(2.0*EPS_0+ &
        dt*beta(i,j,k)+SIG_E(i,j,k)*dt)
    Cb(i,j,k) = (2.0*dt)/(2.0*EPS_0+ &
        dt*beta(i,j,k)+SIG_E(i,j,k)*dt)

 CASE(5) ! Gold (Au)
    MU_R(i,j,k) = 1.0
    SIG_H(i,j,k) = 0.0
    SIG_E(i,j,k) = 0.0
    ! Set dispersive material parameters
    omega_p = 9.03*E/H_BAR
    str = 0.760
    gamma = 0.053*E/H_BAR
    ! Set dispersive material coefficients
    alpha(i,j,k) = (2.0-gamma*dt)/(2.0+gamma*dt)
    beta(i,j,k) = (str*EPS_0*dt*omega_p**2)/ &
        (2.0+gamma*dt)
    ! Set EM field update coefficients
    Da(i,j,k) = (2.0*MU_R(i,j,k)*MU_0- &
        SIG_H(i,j,k)*dt)/(2.0*MU_R(i,j,k)*MU_0+ &
        SIG_H(i,j,k)*dt)
    Db(i,j,k) = (2.0*dt)/(2.0*MU_R(i,j,k)*MU_0+ &
        SIG_H(i,j,k)*dt)
    Ca(i,j,k) = (2.0*EPS_0-dt*beta(i,j,k)- &
        SIG_E(i,j,k)*dt)/(2.0*EPS_0+ &
        dt*beta(i,j,k)+SIG_E(i,j,k)*dt)
    Cb(i,j,k) = (2.0*dt)/(2.0*EPS_0+ &
        dt*beta(i,j,k)+SIG_E(i,j,k)*dt)


 CASE(6) ! Aluminum (Al)
    MU_R(i,j,k) = 1.0
    SIG_H(i,j,k) = 0.0
    SIG_E(i,j,k) = 0.0
    ! Set dispersive material parameters
    omega_p = 14.98*E/H_BAR
    str = 0.523
    gamma = 0.047*E/H_BAR
    ! Set dispersive material coefficients
    alpha(i,j,k) = (2.0-gamma*dt)/(2.0+gamma*dt)
    beta(i,j,k) = (str*EPS_0*dt*omega_p**2)/ &
        (2.0+gamma*dt)
    ! Set EM field update coefficients
    Da(i,j,k) = (2.0*MU_R(i,j,k)*MU_0- &
        SIG_H(i,j,k)*dt)/(2.0*MU_R(i,j,k)*MU_0+ &
```

```
        SIG_H(i,j,k)*dt)
    Db(i,j,k) = (2.0*dt)/(2.0*MU_R(i,j,k)*MU_0+ &
        SIG_H(i,j,k)*dt)
    Ca(i,j,k) = (2.0*EPS_0-dt*beta(i,j,k)- &
        SIG_E(i,j,k)*dt)/(2.0*EPS_0+ &
        dt*beta(i,j,k)+SIG_E(i,j,k)*dt)
    Cb(i,j,k) = (2.0*dt)/(2.0*EPS_0+ &
        dt*beta(i,j,k)+SIG_E(i,j,k)*dt)


CASE(7) ! Copper (Cu)
    MU_R(i,j,k) = 1.0
    SIG_H(i,j,k) = 0.0
    SIG_E(i,j,k) = 0.0
    ! Set dispersive material parameters
    omega_p = 10.83*E/H_BAR
    str = 0.575
    gamma = 0.030*E/H_BAR
    ! Set dispersive material coefficients
    alpha(i,j,k) = (2.0-gamma*dt)/(2.0+gamma*dt)
    beta(i,j,k) = (str*EPS_0*dt*omega_p**2)/ &
        (2.0+gamma*dt)
    ! Set EM field update coefficients
    Da(i,j,k) = (2.0*MU_R(i,j,k)*MU_0- &
        SIG_H(i,j,k)*dt)/(2.0*MU_R(i,j,k)*MU_0+ &
        SIG_H(i,j,k)*dt)
    Db(i,j,k) = (2.0*dt)/(2.0*MU_R(i,j,k)*MU_0+ &
        SIG_H(i,j,k)*dt)
    Ca(i,j,k) = (2.0*EPS_0-dt*beta(i,j,k)- &
        SIG_E(i,j,k)*dt)/(2.0*EPS_0+ &
        dt*beta(i,j,k)+SIG_E(i,j,k)*dt)
    Cb(i,j,k) = (2.0*dt)/(2.0*EPS_0+ &
        dt*beta(i,j,k)+SIG_E(i,j,k)*dt)


CASE(8) ! Chromium (Cr)
    MU_R(i,j,k) = 1.0
    SIG_H(i,j,k) = 0.0
    SIG_E(i,j,k) = 0.0
    ! Set dispersive material parameters
    omega_p = 10.75*E/H_BAR
    str = 0.168
    gamma = 0.047*E/H_BAR
    ! Set dispersive material coefficients
    alpha(i,j,k) = (2.0-gamma*dt)/(2.0+gamma*dt)
    beta(i,j,k) = (str*EPS_0*dt*omega_p**2)/ &
        (2.0+gamma*dt)
    ! Set EM field update coefficients
    Da(i,j,k) = (2.0*MU_R(i,j,k)*MU_0- &
        SIG_H(i,j,k)*dt)/(2.0*MU_R(i,j,k)*MU_0+ &
        SIG_H(i,j,k)*dt)
    Db(i,j,k) = (2.0*dt)/(2.0*MU_R(i,j,k)*MU_0+ &
        SIG_H(i,j,k)*dt)
    Ca(i,j,k) = (2.0*EPS_0-dt*beta(i,j,k)- &
        SIG_E(i,j,k)*dt)/(2.0*EPS_0+ &
        dt*beta(i,j,k)+SIG_E(i,j,k)*dt)
    Cb(i,j,k) = (2.0*dt)/(2.0*EPS_0+ &
        dt*beta(i,j,k)+SIG_E(i,j,k)*dt)


CASE(9) ! Nickel (Ni)
    MU_R(i,j,k) = 1.0
    SIG_H(i,j,k) = 0.0
    SIG_E(i,j,k) = 0.0
    ! Set dispersive material parameters
    omega_p = 15.92*E/H_BAR
    str = 0.096
    gamma = 0.048*E/H_BAR
```

```
   ! Set dispersive material coefficients
   alpha(i,j,k) = (2.0-gamma*dt)/(2.0+gamma*dt)
   beta(i,j,k) = (str*EPS_0*dt*omega_p**2)/ &
       (2.0+gamma*dt)
   ! Set EM field update coefficients
   Da(i,j,k) = (2.0*MU_R(i,j,k)*MU_0- &
       SIG_H(i,j,k)*dt)/(2.0*MU_R(i,j,k)*MU_0+ &
       SIG_H(i,j,k)*dt)
   Db(i,j,k) = (2.0*dt)/(2.0*MU_R(i,j,k)*MU_0+ &
       SIG_H(i,j,k)*dt)
   Ca(i,j,k) = (2.0*EPS_0-dt*beta(i,j,k)- &
       SIG_E(i,j,k)*dt)/(2.0*EPS_0+ &
       dt*beta(i,j,k)+SIG_E(i,j,k)*dt)
   Cb(i,j,k) = (2.0*dt)/(2.0*EPS_0+ &
       dt*beta(i,j,k)+SIG_E(i,j,k)*dt)


CASE(10) ! Tungsten (W)
   MU_R(i,j,k) = 1.0
   SIG_H(i,j,k) = 0.0
   SIG_E(i,j,k) = 0.0
   ! Set dispersive material parameters
   omega_p = 13.22*E/H_BAR
   str = 0.206
   gamma = 0.064*E/H_BAR
   ! Set dispersive material coefficients
   alpha(i,j,k) = (2.0-gamma*dt)/(2.0+gamma*dt)
   beta(i,j,k) = (str*EPS_0*dt*omega_p**2)/ &
       (2.0+gamma*dt)
   ! Set EM field update coefficients
   Da(i,j,k) = (2.0*MU_R(i,j,k)*MU_0- &
       SIG_H(i,j,k)*dt)/(2.0*MU_R(i,j,k)*MU_0+ &
       SIG_H(i,j,k)*dt)
   Db(i,j,k) = (2.0*dt)/(2.0*MU_R(i,j,k)*MU_0+ &
       SIG_H(i,j,k)*dt)
   Ca(i,j,k) = (2.0*EPS_0-dt*beta(i,j,k)- &
       SIG_E(i,j,k)*dt)/(2.0*EPS_0+ &
       dt*beta(i,j,k)+SIG_E(i,j,k)*dt)
   Cb(i,j,k) = (2.0*dt)/(2.0*EPS_0+ &
       dt*beta(i,j,k)+SIG_E(i,j,k)*dt)


CASE(11) ! Titanium (Ti)
   MU_R(i,j,k) = 1.0
   SIG_H(i,j,k) = 0.0
   SIG_E(i,j,k) = 0.0
   ! Set dispersive material parameters
   omega_p = 7.29*E/H_BAR
   str = 0.148
   gamma = 0.082*E/H_BAR
   ! Set dispersive material coefficients
   alpha(i,j,k) = (2.0-gamma*dt)/(2.0+gamma*dt)
   beta(i,j,k) = (str*EPS_0*dt*omega_p**2)/ &
       (2.0+gamma*dt)
   ! Set EM field update coefficients
   Da(i,j,k) = (2.0*MU_R(i,j,k)*MU_0- &
       SIG_H(i,j,k)*dt)/(2.0*MU_R(i,j,k)*MU_0+ &
       SIG_H(i,j,k)*dt)
   Db(i,j,k) = (2.0*dt)/(2.0*MU_R(i,j,k)*MU_0+ &
       SIG_H(i,j,k)*dt)
   Ca(i,j,k) = (2.0*EPS_0-dt*beta(i,j,k)- &
       SIG_E(i,j,k)*dt)/(2.0*EPS_0+ &
       dt*beta(i,j,k)+SIG_E(i,j,k)*dt)
   Cb(i,j,k) = (2.0*dt)/(2.0*EPS_0+ &
       dt*beta(i,j,k)+SIG_E(i,j,k)*dt)


CASE(12) ! Beryllium (Be)
```

```
   MU_R(i,j,k) = 1.0
   SIG_H(i,j,k) = 0.0
   SIG_E(i,j,k) = 0.0
   ! Set dispersive material parameters
   omega_p = 18.51*E/H_BAR
   str = 0.084
   gamma = 0.035*E/H_BAR
   ! Set dispersive material coefficients
   alpha(i,j,k) = (2.0-gamma*dt)/(2.0+gamma*dt)
   beta(i,j,k) = (str*EPS_0*dt*omega_p**2)/ &
       (2.0+gamma*dt)
   ! Set EM field update coefficients
   Da(i,j,k) = (2.0*MU_R(i,j,k)*MU_0- &
       SIG_H(i,j,k)*dt)/(2.0*MU_R(i,j,k)*MU_0+ &
       SIG_H(i,j,k)*dt)
   Db(i,j,k) = (2.0*dt)/(2.0*MU_R(i,j,k)*MU_0+ &
       SIG_H(i,j,k)*dt)
   Ca(i,j,k) = (2.0*EPS_0-dt*beta(i,j,k)- &
       SIG_E(i,j,k)*dt)/(2.0*EPS_0+ &
       dt*beta(i,j,k)+SIG_E(i,j,k)*dt)
   Cb(i,j,k) = (2.0*dt)/(2.0*EPS_0+ &
       dt*beta(i,j,k)+SIG_E(i,j,k)*dt)


CASE(13) ! Palladium (Pd)
   MU_R(i,j,k) = 1.0
   SIG_H(i,j,k) = 0.0
   SIG_E(i,j,k) = 0.0
   ! Set dispersive material parameters
   omega_p = 9.72*E/H_BAR
   str = 0.330
   gamma = 0.008*E/H_BAR
   ! Set dispersive material coefficients
   alpha(i,j,k) = (2.0-gamma*dt)/(2.0+gamma*dt)
   beta(i,j,k) = (str*EPS_0*dt*omega_p**2)/ &
       (2.0+gamma*dt)
   ! Set EM field update coefficients
   Da(i,j,k) = (2.0*MU_R(i,j,k)*MU_0- &
       SIG_H(i,j,k)*dt)/(2.0*MU_R(i,j,k)*MU_0+ &
       SIG_H(i,j,k)*dt)
   Db(i,j,k) = (2.0*dt)/(2.0*MU_R(i,j,k)*MU_0+ &
       SIG_H(i,j,k)*dt)
   Ca(i,j,k) = (2.0*EPS_0-dt*beta(i,j,k)- &
       SIG_E(i,j,k)*dt)/(2.0*EPS_0+ &
       dt*beta(i,j,k)+SIG_E(i,j,k)*dt)
   Cb(i,j,k) = (2.0*dt)/(2.0*EPS_0+ &
       dt*beta(i,j,k)+SIG_E(i,j,k)*dt)


CASE(14) ! Platinum (Pt)
   MU_R(i,j,k) = 1.0
   SIG_H(i,j,k) = 0.0
   SIG_E(i,j,k) = 0.0
   ! Set dispersive material parameters
   omega_p = 9.59*E/H_BAR
   str = 0.333
   gamma = 0.080*E/H_BAR
   ! Set dispersive material coefficients
   alpha(i,j,k) = (2.0-gamma*dt)/(2.0+gamma*dt)
   beta(i,j,k) = (str*EPS_0*dt*omega_p**2)/ &
       (2.0+gamma*dt)
   ! Set EM field update coefficients
   Da(i,j,k) = (2.0*MU_R(i,j,k)*MU_0- &
       SIG_H(i,j,k)*dt)/(2.0*MU_R(i,j,k)*MU_0+ &
       SIG_H(i,j,k)*dt)
   Db(i,j,k) = (2.0*dt)/(2.0*MU_R(i,j,k)*MU_0+ &
       SIG_H(i,j,k)*dt)
   Ca(i,j,k) = (2.0*EPS_0-dt*beta(i,j,k)- &
```

```
                    SIG_E(i,j,k)*dt)/(2.0*EPS_0+ &
                    dt*beta(i,j,k)+SIG_E(i,j,k)*dt)
                Cb(i,j,k) = (2.0*dt)/(2.0*EPS_0+ &
                    dt*beta(i,j,k)+SIG_E(i,j,k)*dt)

            ENDSELECT
        ENDDO
    ENDDO
ENDDO

WRITE(*,*) "Geometry constructed"
WRITE(*,*) ""

!~~~~~~~~~~~~~~~~~~~~~~~~~~~~~~~~~~~~~~~~~~~~~~~~~~~~~~~~~~~~~~~~~~~~~~~~
! Calculate and set CPML properties
!~~~~~~~~~~~~~~~~~~~~~~~~~~~~~~~~~~~~~~~~~~~~~~~~~~~~~~~~~~~~~~~~~~~~~~~~

    ! H-field
    ! z-axis
    ! Bottom
    DO k = 1, NzPML_b-1
        sigHz_b(k) = sigma_zmax*((NzPML_b-k-0.5)/(NzPML_b-1.0))**m
        alphaHz_b(k) = alpha_zmax*((k-0.5)/(NzPML_b-1.0))**ma
        kappaHz_b(k) = 1.0+(kappa_zmax-1.0)* &
            (ABS(NzPML_b-k-0.5)/(NzPML_b-1.0))**m
        bHz_b(k) = EXP(-(sigHz_b(k)/kappaHz_b(k)+ &
            alphaHz_b(k))*dt/EPS_0)
        cHz_b(k) = sigHz_b(k)*(bHz_b(k)-1.0)/ &
            (sigHz_b(k)+kappaHz_b(k)*alphaHz_b(k))/ &
            kappaHz_b(k)
    ENDDO
    ! Top
    DO k = 1, NzPML_t-1
        sigHz_t(k) = sigma_zmax*((NzPML_t-k-0.5)/(NzPML_t-1.0))**m
        alphaHz_t(k) = alpha_zmax*((k-0.5)/(NzPML_t-1.0))**ma
        kappaHz_t(k) = 1.0+(kappa_zmax-1.0)* &
            (ABS(NzPML_t-k-0.5)/(NzPML_t-1.0))**m
        bHz_t(k) = EXP(-(sigHz_t(k)/kappaHz_t(k)+ &
            alphaHz_t(k))*dt/EPS_0)
        cHz_t(k) = sigHz_t(k)*(bHz_t(k)-1.0)/ &
            (sigHz_t(k)+kappaHz_t(k)*alphaHz_t(k))/ &
            kappaHz_t(k)
    ENDDO

    ! E-field
    ! z-axis
    ! Bottom
    DO k = 1, NzPML_b
        sigEz_b(k) = sigma_zmax*((NzPML_b-k)/(NzPML_b-1.0))**m
        alphaEz_b(k) = alpha_zmax*((k-1)/(NzPML_b-1.0))**ma
        kappaEz_b(k) = 1.0+(kappa_zmax-1.0)* &
            (ABS(NzPML_b-k)/(NzPML_b-1.0))**m
        bEz_b(k) = EXP(-(sigEz_b(k)/kappaEz_b(k)+ &
            alphaEz_b(k))*dt/EPS_0)
        IF ((sigEz_b(k) == 0.0) .AND. (alphaEz_b(k) == 0.0) &
            .AND. (k == NzPML_b)) THEN
            cEz_b(k) = 0.0
        ELSE
            cEz_b(k) = sigEz_b(k)*(bEz_b(k)-1.0)/ &
                (sigEz_b(k)+kappaEz_b(k)*alphaEz_b(k))/ &
                kappaEz_b(k)
       ENDIF
    ENDDO
    ! Top
    DO k = 1, NzPML_t
        sigEz_t(k) = sigma_zmax*((NzPML_t-k)/(NzPML_t-1.0))**m
        alphaEz_t(k) = alpha_zmax*((k-1)/(NzPML_t-1.0))**ma
        kappaEz_t(k) = 1.0+(kappa_zmax-1.0)* &
```

```
            (ABS(NzPML_t-k)/(NzPML_t-1.0))**m
        bEz_t(k) = EXP(-(sigEz_t(k)/kappaEz_t(k)+ &
            alphaEz_t(k))*dt/EPS_0)
        IF ((sigEz_t(k) == 0.0) .AND. (alphaEz_t(k) == 0.0) &
            .AND. (k == NzPML_t)) THEN
            cEz_t(k) = 0.0
        ELSE
            cEz_t(k) = sigEz_t(k)*(bEz_t(k)-1.0)/ &
                (sigEz_t(k)+kappaEz_t(k)*alphaEz_t(k))/ &
                kappaEz_t(k)
        ENDIF
    ENDDO

    WRITE(*,*) "CPML properties set"
    WRITE(*,*) ""

!~~~~~~~~~~~~~~~~~~~~~~~~~~~~~~~~~~~~~~~~~~~~~~~~~~~~~~~~~~~~~~~~~~~~~~~~~~~
! Calculate and set EM field update denominators
!~~~~~~~~~~~~~~~~~~~~~~~~~~~~~~~~~~~~~~~~~~~~~~~~~~~~~~~~~~~~~~~~~~~~~~~~~~~

    ! x-axis
    den_Hx(:) = 1.0/delx
    den_Ex(:) = 1.0/delx

    ! y-axis
    den_Hy(:) = 1.0/dely
    den_Ey(:) = 1.0/dely

    ! z-axis
    ! H-field
    kPML = NzPML_t-1
    DO k = 1, Nz-1
        IF (k <= NzPML_b-1) THEN
            den_Hz(k) = 1.0/(kappaHz_b(k)*delz)
        ELSEIF (k >= Nz+1-NzPML_t) THEN
            den_Hz(k) = 1.0/(kappaHz_t(kPML)*delz)
            kPML = kPML-1
        ELSE
            den_Hz(k) = 1.0/delz
        ENDIF
    ENDDO
    ! E-field
    kPML = NzPML_t
    DO k = 1, Nz-1
        IF (k <= NzPML_b) THEN
            den_Ez(k) = 1.0/(kappaEz_b(k)*delz)
        ELSEIF (k >= Nz+1-NzPML_t) THEN
            den_Ez(k) = 1.0/(kappaEz_t(kPML)*delz)
            kPML = kPML-1
        ELSE
            den_Ez(k) = 1.0/delz
        ENDIF
    ENDDO

    WRITE(*,*) "EM field update denominators set"
    WRITE(*,*) ""

!~~~~~~~~~~~~~~~~~~~~~~~~~~~~~~~~~~~~~~~~~~~~~~~~~~~~~~~~~~~~~~~~~~~~~~~~~~~
! Start stepping through time
!~~~~~~~~~~~~~~~~~~~~~~~~~~~~~~~~~~~~~~~~~~~~~~~~~~~~~~~~~~~~~~~~~~~~~~~~~~~

    ! Output problem parameters to terminal
    WRITE(*,*) "Mesh size in x: ", delx, "m"
    WRITE(*,*) "Mesh size in y: ", dely, "m"
    WRITE(*,*) "Mesh size in z: ", delz, "m"
    WRITE(*,*) ""

    WRITE(*,*) "Number of cells in x: ", Nx
```

```
    WRITE(*,*) "Number of cells in y: ", Ny
    WRITE(*,*) "Number of cells in z: ", Nz
    WRITE(*,*) ""

    WRITE(*,*) "Time step: ", dt, "s"
    WRITE(*,*) "Maximum # of iterations: ", maxiter
    WRITE(*,*) "Total simulation time: ", maxiter*dt, "s"
    WRITE(*,*) ""

    WRITE(*,*) "Entering time loop"
    WRITE(*,*) ""

    DO n = 1, maxiter

!~~~~~~~~~~~~~~~~~~~~~~~~~~~~~~~~~~~~~~~~~~~~~~~~~~~~~~~~~~~~~~~~~~~~~~~~~~~
! Construct source
!~~~~~~~~~~~~~~~~~~~~~~~~~~~~~~~~~~~~~~~~~~~~~~~~~~~~~~~~~~~~~~~~~~~~~~~~~~~

        temporal_src = -8.0*LOG(2.0)*(n*dt-t0)/tw* &
            EXP(-4.0*LOG(2.0)*((n*dt-t0)/tw)**2)

!~~~~~~~~~~~~~~~~~~~~~~~~~~~~~~~~~~~~~~~~~~~~~~~~~~~~~~~~~~~~~~~~~~~~~~~~~~~
! Update magnetic field (Hx)
!~~~~~~~~~~~~~~~~~~~~~~~~~~~~~~~~~~~~~~~~~~~~~~~~~~~~~~~~~~~~~~~~~~~~~~~~~~~

        DO k = 1, Nz-1
            ! Main grid
            DO j = 1, Ny-1
                DO i = 1, Nx
                    SELECT CASE(ID(i,j,k))

                    CASE(0,1,3,4,5,6,7,8,9,10,11,12,13,14)
                        Hx(i,j,k) = Da(i,j,k)*Hx(i,j,k)+ &
                            Db(i,j,k)*((Ey(i,j,k+1,MOD(n,2)+1)- &
                            Ey(i,j,k,MOD(n,2)+1))*den_Hz(k)+ &
                            (Ez(i,j,k,MOD(n,2)+1)- &
                            Ez(i,j+1,k,MOD(n,2)+1))*den_Hy(j))
                    CASE(2)
                        Hx(i,j,k) = 0.0

                    ENDSELECT
                ENDDO
            ENDDO
        ENDDO

        ! PML, z-axis
        ! Bottom
        DO k = 1, NzPML_b-1
            DO j = 1, Ny-1
                DO i = 1, Nx
                    psiHxz_b(i,j,k) = bHz_b(k)*psiHxz_b(i,j,k)+ &
                        cHz_b(k)*(Ey(i,j,k+1,MOD(n,2)+1)- &
                        Ey(i,j,k,MOD(n,2)+1))/delz
                    Hx(i,j,k) = Hx(i,j,k)+Db(i,j,k)*psiHxz_b(i,j,k)
                ENDDO
            ENDDO
        ENDDO
        ! Top
        kPML = NzPML_t-1
        DO k = Nz+1-NzPML_t, Nz-1
            DO j = 1, Ny-1
                DO i = 1, Nx
                    psiHxz_t(i,j,kPML) = bHz_t(kPML)* &
                        psiHxz_t(i,j,kPML)+cHz_t(kPML)* &
                        (Ey(i,j,k+1,MOD(n,2)+1)- &
                        Ey(i,j,k,MOD(n,2)+1))/delz
                    Hx(i,j,k) = Hx(i,j,k)+ &
                        Db(i,j,k)*psiHxz_t(i,j,kPML)
```

```
            ENDDO
        ENDDO
        kPML = kPML-1
    ENDDO

!~~~~~~~~~~~~~~~~~~~~~~~~~~~~~~~~~~~~~~~~~~~~~~~~~~~~~~~~~~~~~~~~~~~~~~~~
! Periodic boundary condition for Hx
!~~~~~~~~~~~~~~~~~~~~~~~~~~~~~~~~~~~~~~~~~~~~~~~~~~~~~~~~~~~~~~~~~~~~~~~~

    ! j = Ny-1
    DO k = 1, Nz-1
        DO i = 1, Nx
            Hx(i,Ny-1,k) = Hx(i,1,k)
        ENDDO
    ENDDO

!~~~~~~~~~~~~~~~~~~~~~~~~~~~~~~~~~~~~~~~~~~~~~~~~~~~~~~~~~~~~~~~~~~~~~~~~
! Update magnetic field (Hy)
!~~~~~~~~~~~~~~~~~~~~~~~~~~~~~~~~~~~~~~~~~~~~~~~~~~~~~~~~~~~~~~~~~~~~~~~~

    DO k = 1, Nz-1
        ! Main grid
        DO j = 1, Ny
            DO i = 1, Nx-1
                SELECT CASE(ID(i,j,k))

                CASE(0,1,3,4,5,6,7,8,9,10,11,12,13,14)
                    Hy(i,j,k) = Da(i,j,k)*Hy(i,j,k)+ &
                        Db(i,j,k)*((Ex(i,j,k,MOD(n,2)+1)- &
                            Ex(i,j,k+1,MOD(n,2)+1))*den_Hz(k)+ &
                            (Ez(i+1,j,k,MOD(n,2)+1)- &
                            Ez(i,j,k,MOD(n,2)+1))*den_Hx(i))
                CASE(2)
                    Hy(i,j,k) = 0.0

                ENDSELECT
            ENDDO
        ENDDO
    ENDDO

    ! PML, z-axis
    ! Bottom
    DO k = 1, NzPML_b-1
        DO j = 1, Ny
            DO i = 1, Nx-1
                psiHyz_b(i,j,k) = bHz_b(k)*psiHyz_b(i,j,k)+ &
                    cHz_b(k)*(Ex(i,j,k,MOD(n,2)+1)- &
                    Ex(i,j,k+1,MOD(n,2)+1))/delz
                Hy(i,j,k) = Hy(i,j,k)+Db(i,j,k)*psiHyz_b(i,j,k)
            ENDDO
        ENDDO
    ENDDO
    ! Top
    kPML = NzPML_t-1
    DO k =  Nz+1-NzPML_t, Nz-1
        DO j = 1, Ny
            DO i = 1, Nx-1
                psiHyz_t(i,j,kPML) = bHz_t(kPML)* &
                    psiHyz_t(i,j,kPML)+ &
                    cHz_t(kPML)*(Ex(i,j,k,MOD(n,2)+1)- &
                    Ex(i,j,k+1,MOD(n,2)+1))/delz
                Hy(i,j,k) = Hy(i,j,k)+ &
                    Db(i,j,k)*psiHyz_t(i,j,kPML)
            ENDDO
        ENDDO
        kPML = kPML-1
    ENDDO
```

```
!~~~~~~~~~~~~~~~~~~~~~~~~~~~~~~~~~~~~~~~~~~~~~~~~~~~~~~~~~~~~~~~~~~~~~~~~
! Incident Hy
!~~~~~~~~~~~~~~~~~~~~~~~~~~~~~~~~~~~~~~~~~~~~~~~~~~~~~~~~~~~~~~~~~~~~~~~~

        DO j = 1, Ny
            DO i = 1, Nx-1
                Hy(i,j,kstart-1) = Hy(i,j,kstart-1)+ &
                    Db(i,j,kstart-1)*ampE*temporal_src* &
                    COS(k0*(kstart+delz/2.0))
            ENDDO
        ENDDO

!~~~~~~~~~~~~~~~~~~~~~~~~~~~~~~~~~~~~~~~~~~~~~~~~~~~~~~~~~~~~~~~~~~~~~~~~
! Periodic boundary condition for Hy
!~~~~~~~~~~~~~~~~~~~~~~~~~~~~~~~~~~~~~~~~~~~~~~~~~~~~~~~~~~~~~~~~~~~~~~~~

        ! i = Nx-1
        DO k = 1, Nz-1
            DO j = 1, Ny
                Hy(Nx-1,j,k) = Hy(1,j,k)
            ENDDO
        ENDDO

!~~~~~~~~~~~~~~~~~~~~~~~~~~~~~~~~~~~~~~~~~~~~~~~~~~~~~~~~~~~~~~~~~~~~~~~~
! Update magnetic field (Hz)
!~~~~~~~~~~~~~~~~~~~~~~~~~~~~~~~~~~~~~~~~~~~~~~~~~~~~~~~~~~~~~~~~~~~~~~~~

        DO k = 2, Nz-1
            ! Main grid
            DO j = 1, Ny-1
                DO i = 1, Nx-1
                    SELECT CASE(ID(i,j,k))

                    CASE(0,1,3,4,5,6,7,8,9,10,11,12,13,14)
                        Hz(i,j,k) = Da(i,j,k)*Hz(i,j,k)+ &
                            Db(i,j,k)*((Ex(i,j+1,k,MOD(n,2)+1)- &
                            Ex(i,j,k,MOD(n,2)+1))*den_Hy(j)+ &
                            (Ey(i,j,k,MOD(n,2)+1)- &
                            Ey(i+1,j,k,MOD(n,2)+1))*den_Hx(i))
                    CASE(2)
                        Hz(i,j,k) = 0.0

                    ENDSELECT
                ENDDO
            ENDDO
        ENDDO

!~~~~~~~~~~~~~~~~~~~~~~~~~~~~~~~~~~~~~~~~~~~~~~~~~~~~~~~~~~~~~~~~~~~~~~~~
! Periodic boundary condition for Hz
!~~~~~~~~~~~~~~~~~~~~~~~~~~~~~~~~~~~~~~~~~~~~~~~~~~~~~~~~~~~~~~~~~~~~~~~~

        ! i = Nx-1
        DO k = 2, Nz-1
            DO j = 1, Ny-1
                Hz(Nx-1,j,k) = Hz(1,j,k)
            ENDDO
        ENDDO

        ! j = Ny-1
        DO k = 2, Nz-1
            DO i = 1, Nx-1
                Hz(i,Ny-1,k) = Hz(i,1,k)
            ENDDO
        ENDDO

!~~~~~~~~~~~~~~~~~~~~~~~~~~~~~~~~~~~~~~~~~~~~~~~~~~~~~~~~~~~~~~~~~~~~~~~~
! Update electric field (Ex)
!~~~~~~~~~~~~~~~~~~~~~~~~~~~~~~~~~~~~~~~~~~~~~~~~~~~~~~~~~~~~~~~~~~~~~~~~
```

```
        DO k = 2, Nz-1
            ! Main grid
            DO j = 2, Ny
                DO i = 1, Nx-1
                    SELECT CASE(ID(i,j,k))

                    CASE(0,2,3)
                        Ex(i,j,k,MOD(n+1,2)+1) = Ca(i,j,k)* &
                            Ex(i,j,k,MOD(n,2)+1)+Cb(i,j,k)* &
                            ((Hy(i,j,k-1)-Hy(i,j,k))*den_Ez(k)+ &
                            (Hz(i,j,k)-Hz(i,j-1,k))*den_Ey(j))
                    CASE(1)
                        Ex(i,j,k,MOD(n+1,2)+1) = 0.0
                    CASE(4,5,6,7,8,9,10,11,12,13,14)
                        Ex(i,j,k,MOD(n+1,2)+1) = Ca(i,j,k)* &
                            Ex(i,j,k,MOD(n,2)+1)+Cb(i,j,k)* &
                            ((Hy(i,j,k-1)-Hy(i,j,k))*den_Ez(k)+ &
                            (Hz(i,j,k)-Hz(i,j-1,k))*den_Ey(j)- &
                            (1.0+alpha(i,j,k))*0.5d0*Jx(i,j,k))

                    ENDSELECT
                ENDDO
            ENDDO
        ENDDO

        ! PML, z-axis
        ! Bottom
        DO k = 2, NzPML_b
            DO j = 2, Ny
                DO i = 1, Nx-1
                    psiExz_b(i,j,k) = bEz_b(k)*psiExz_b(i,j,k)+ &
                        cEz_b(k)*(Hy(i,j,k-1)-Hy(i,j,k))/delz
                    Ex(i,j,k,MOD(n+1,2)+1) = Ex(i,j,k,MOD(n+1,2)+1)+ &
                        Cb(i,j,k)*psiExz_b(i,j,k)
                ENDDO
            ENDDO
        ENDDO
        ! Top
        kPML = NzPML_t
        DO k = Nz+1-NzPML_t, Nz-1
            DO j = 2, Ny
                DO i = 1, Nx-1
                    psiExz_t(i,j,kPML) = bEz_t(kPML)* &
                        psiExz_t(i,j,kPML)+cEz_t(kPML)* &
                        (Hy(i,j,k-1)-Hy(i,j,k))/delz
                    Ex(i,j,k,MOD(n+1,2)+1) = Ex(i,j,k,MOD(n+1,2)+1)+ &
                        Cb(i,j,k)*psiExz_t(i,j,kPML)
                ENDDO
            ENDDO
            kPML = kPML-1
        ENDDO

!~~~~~~~~~~~~~~~~~~~~~~~~~~~~~~~~~~~~~~~~~~~~~~~~~~~~~~~~~~~~~~~~~~~~~~~~
! Incident Ex
!~~~~~~~~~~~~~~~~~~~~~~~~~~~~~~~~~~~~~~~~~~~~~~~~~~~~~~~~~~~~~~~~~~~~~~~~

        DO j = 1, Ny
            DO i = 1, Nx-1
                Ex(i,j,kstart,MOD(n+1,2)+1) = &
                    Ex(i,j,kstart,MOD(n+1,2)+1)+Cb(i,j,kstart)* &
                    ampH*temporal_src*COS(k0*(kstart-delz/2.0))
            ENDDO
        ENDDO

!~~~~~~~~~~~~~~~~~~~~~~~~~~~~~~~~~~~~~~~~~~~~~~~~~~~~~~~~~~~~~~~~~~~~~~~~
! Periodic boundary condition for Ex
!~~~~~~~~~~~~~~~~~~~~~~~~~~~~~~~~~~~~~~~~~~~~~~~~~~~~~~~~~~~~~~~~~~~~~~~~
```

```
        ! j = 1
        DO k = 2, Nz-1
            DO i = 1, Nx-1
                Ex(i,1,k,MOD(n+1,2)+1) = Ex(i,Ny,k,MOD(n+1,2)+1)
            ENDDO
        ENDDO

!~~~~~~~~~~~~~~~~~~~~~~~~~~~~~~~~~~~~~~~~~~~~~~~~~~~~~~~~~~~~~~~~~~~~~~~~
! Update electric field (Ey)
!~~~~~~~~~~~~~~~~~~~~~~~~~~~~~~~~~~~~~~~~~~~~~~~~~~~~~~~~~~~~~~~~~~~~~~~~

        DO k = 2, Nz-1
            ! Main grid
            DO j = 1, Ny-1
                DO i = 2, Nx
                    SELECT CASE(ID(i,j,k))

                    CASE(0,2,3)
                        Ey(i,j,k,MOD(n+1,2)+1) = Ca(i,j,k)* &
                            Ey(i,j,k,MOD(n,2)+1)+Cb(i,j,k)* &
                            ((Hx(i,j,k)-Hx(i,j,k-1))*den_Ez(k)+ &
                            (Hz(i-1,j,k)-Hz(i,j,k))*den_Ex(i))
                    CASE(1)
                        Ey(i,j,k,MOD(n+1,2)+1) = 0.0
                    CASE(4,5,6,7,8,9,10,11,12,13,14)
                        Ey(i,j,k,MOD(n+1,2)+1) = Ca(i,j,k)* &
                            Ey(i,j,k,MOD(n,2)+1)+Cb(i,j,k)* &
                            ((Hx(i,j,k)-Hx(i,j,k-1))*den_Ez(k)+ &
                            (Hz(i-1,j,k)-Hz(i,j,k))*den_Ex(i)- &
                            (1.0+alpha(i,j,k))*0.5d0*Jy(i,j,k))

                    ENDSELECT
                ENDDO
            ENDDO
        ENDDO

        ! PML, z-axis
        ! Bottom
        DO k = 2, NzPML_b
            DO j = 1, Ny-1
                DO i = 2, Nx
                    psiEyz_b(i,j,k) = bEz_b(k)*psiEyz_b(i,j,k)+ &
                        cEz_b(k)*(Hx(i,j,k)-Hx(i,j,k-1))/delz
                    Ey(i,j,k,MOD(n+1,2)+1) = Ey(i,j,k,MOD(n+1,2)+1)+ &
                        Cb(i,j,k)*psiEyz_b(i,j,k)
                ENDDO
            ENDDO
        ENDDO
        ! Top
        kPML = NzPML_t
        DO k = Nz+1-NzPML_t, Nz-1
            DO j = 1, Ny-1
                DO i = 2, Nx
                    psiEyz_t(i,j,kPML) = bEz_t(kPML)* &
                        psiEyz_t(i,j,kPML)+cEz_t(kPML)* &
                        (Hx(i,j,k)-Hx(i,j,k-1))/delz
                    Ey(i,j,k,MOD(n+1,2)+1) = Ey(i,j,k,MOD(n+1,2)+1)+ &
                        Cb(i,j,k)*psiEyz_t(i,j,kPML)
                ENDDO
            ENDDO
            kPML = kPML-1
        ENDDO

!~~~~~~~~~~~~~~~~~~~~~~~~~~~~~~~~~~~~~~~~~~~~~~~~~~~~~~~~~~~~~~~~~~~~~~~~
! Periodic boundary condition for Ey
!~~~~~~~~~~~~~~~~~~~~~~~~~~~~~~~~~~~~~~~~~~~~~~~~~~~~~~~~~~~~~~~~~~~~~~~~
```

```
        ! i = 1
        DO k = 2, Nz-1
            DO j = 1, Ny-1
                Ey(1,j,k,MOD(n+1,2)+1) = Ey(Nx,j,k,MOD(n+1,2)+1)
            ENDDO
        ENDDO

!~~~~~~~~~~~~~~~~~~~~~~~~~~~~~~~~~~~~~~~~~~~~~~~~~~~~~~~~~~~~~~~~~~~~~~~~
! Update electric field (Ez)
!~~~~~~~~~~~~~~~~~~~~~~~~~~~~~~~~~~~~~~~~~~~~~~~~~~~~~~~~~~~~~~~~~~~~~~~~

        DO k = 1, Nz-1
            ! Main grid
            DO j = 2, Ny
                DO i = 2, Nx
                    SELECT CASE(ID(i,j,k))

                    CASE(0,2,3)
                        Ez(i,j,k,MOD(n+1,2)+1) = Ca(i,j,k)* &
                            Ez(i,j,k,MOD(n,2)+1)+Cb(i,j,k)* &
                            ((Hx(i,j-1,k)-Hx(i,j,k))*den_Ey(j)+ &
                            (Hy(i,j,k)-Hy(i-1,j,k))*den_Ex(i))
                    CASE(1)
                        Ez(i,j,k,MOD(n+1,2)+1) = 0.0
                    CASE(4,5,6,7,8,9,10,11,12,13,14)
                        Ez(i,j,k,MOD(n+1,2)+1) = Ca(i,j,k)* &
                            Ez(i,j,k,MOD(n,2)+1)+Cb(i,j,k)* &
                            ((Hx(i,j-1,k)-Hx(i,j,k))*den_Ey(j)+ &
                            (Hy(i,j,k)-Hy(i-1,j,k))*den_Ex(i)- &
                            (1.0+alpha(i,j,k))*0.5d0*Jz(i,j,k))

                    ENDSELECT
                ENDDO
            ENDDO
        ENDDO

!~~~~~~~~~~~~~~~~~~~~~~~~~~~~~~~~~~~~~~~~~~~~~~~~~~~~~~~~~~~~~~~~~~~~~~~~
! Periodic boundary condition for Ez
!~~~~~~~~~~~~~~~~~~~~~~~~~~~~~~~~~~~~~~~~~~~~~~~~~~~~~~~~~~~~~~~~~~~~~~~~

        ! i = 0
        DO k = 1, Nz-1
            DO j = 1, Ny
                Ez(1,j,k,MOD(n+1,2)+1) = Ez(Nx,j,k,MOD(n+1,2)+1)
            ENDDO
        ENDDO

        ! j = 0
        DO k = 1, Nz-1
            DO i = 1, Nx
                Ez(i,1,k,MOD(n+1,2)+1) = Ez(i,Ny,k,MOD(n+1,2)+1)
            ENDDO
        ENDDO

!~~~~~~~~~~~~~~~~~~~~~~~~~~~~~~~~~~~~~~~~~~~~~~~~~~~~~~~~~~~~~~~~~~~~~~~~
! Update dispersive material polarization current densities
!~~~~~~~~~~~~~~~~~~~~~~~~~~~~~~~~~~~~~~~~~~~~~~~~~~~~~~~~~~~~~~~~~~~~~~~~

        ! x-component
        DO k = 2, Nz-1
            DO j = 2, Ny
                DO i = 1, Nx-1
                    SELECT CASE(ID(i,j,k))

                    CASE(4,5,6,7,8,9,10,11,12,13,14)
                        Jx(i,j,k) = alpha(i,j,k)*Jx(i,j,k)+ &
                            beta(i,j,k)*(Ex(i,j,k,MOD(n+1,2)+1)+ &
                            Ex(i,j,k,MOD(n,2)+1))
```

```
                ENDSELECT
            ENDDO
        ENDDO
    ENDDO

    ! y-component
    DO k = 2, Nz-1
        DO j = 1, Ny-1
            DO i = 2, Nx
                SELECT CASE(ID(i,j,k))

                CASE(4,5,6,7,8,9,10,11,12,13,14)
                    Jy(i,j,k) = alpha(i,j,k)*Jy(i,j,k)+ &
                        beta(i,j,k)*(Ey(i,j,k,MOD(n+1,2)+1)+ &
                        Ey(i,j,k,MOD(n,2)+1))

                ENDSELECT
            ENDDO
        ENDDO
    ENDDO

    ! z-component
    DO k = 1, Nz-1
        DO j = 2, Ny
            DO i = 2, Nx
                SELECT CASE(ID(i,j,k))

                CASE(4,5,6,7,8,9,10,11,12,13,14)
                    Jz(i,j,k) = alpha(i,j,k)*Jz(i,j,k)+ &
                        beta(i,j,k)*(Ez(i,j,k,MOD(n+1,2)+1)+ &
                        Ez(i,j,k,MOD(n,2)+1))

                ENDSELECT
            ENDDO
        ENDDO
    ENDDO

!~~~~~~~~~~~~~~~~~~~~~~~~~~~~~~~~~~~~~~~~~~~~~~~~~~~~~~~~~~~~~~~~~~~~~~~~
! Write to output files
!~~~~~~~~~~~~~~~~~~~~~~~~~~~~~~~~~~~~~~~~~~~~~~~~~~~~~~~~~~~~~~~~~~~~~~~~

    WRITE(30,*) Hx(isrc,jsrc,ksrc)
    WRITE(31,*) Hy(isrc,jsrc,ksrc)
    WRITE(32,*) Hz(isrc,jsrc,ksrc)

    WRITE(33,*) Ex(isrc,jsrc,ksrc,MOD(n+1,2)+1)
    WRITE(34,*) Ey(isrc,jsrc,ksrc,MOD(n+1,2)+1)
    WRITE(35,*) Ez(isrc,jsrc,ksrc,MOD(n+1,2)+1)

    ! Output a plane of the simulation domain (E-Field)
    IF (MOD(n,50) == 0) THEN
        WRITE(step,"(f6.0, a)") REAL(n), ".txt"
        filenameE = "Ex_xy"//step
        OPEN(UNIT = 38, FILE = filenameE)
        DO j = 1, Ny
           DO i = 1, Nx
              WRITE(38,*) Ex(i,j,500,MOD(n+1,2)+1)
           ENDDO
        ENDDO
        CLOSE(UNIT = 38)

        filenameE = "Ex_xz"//step
        OPEN(UNIT = 39, FILE = filenameE)
        DO k = 300, 700
           DO i = 1, Nx
              WRITE(39,*) Ex(i,150,k,MOD(n+1,2)+1)
           ENDDO
```

```
            ENDDO
            CLOSE(UNIT = 39)
        ENDIF

        ! Integrate transmitted E-field over a plane
        transE = SUM(Ex(:,:,600,MOD(n+1,2)+1))
        WRITE(42,*) transE

        ! Periodically write progress to terminal
        IF (MOD(n,10) == 0) THEN
            WRITE(*,"(a,i6,a,i6,a,f6.2,a)") "Done step ", &
                n, " of ", maxiter, &
                " (", REAL(n)/REAL(maxiter)*100, "% complete)"
        ENDIF

!~~~~~~~~~~~~~~~~~~~~~~~~~~~~~~~~~~~~~~~~~~~~~~~~~~~~~~~~~~~~~~~~~~~~~~~~~~~~
! Finish stepping through time
!~~~~~~~~~~~~~~~~~~~~~~~~~~~~~~~~~~~~~~~~~~~~~~~~~~~~~~~~~~~~~~~~~~~~~~~~~~~~

    ENDDO

    WRITE(*,*) ""
    WRITE(*,*) "Exiting time loop"
    WRITE(*,*) ""

!~~~~~~~~~~~~~~~~~~~~~~~~~~~~~~~~~~~~~~~~~~~~~~~~~~~~~~~~~~~~~~~~~~~~~~~~~~~~
! Close output files
!~~~~~~~~~~~~~~~~~~~~~~~~~~~~~~~~~~~~~~~~~~~~~~~~~~~~~~~~~~~~~~~~~~~~~~~~~~~~

    CLOSE(UNIT = 30)
    CLOSE(UNIT = 31)
    CLOSE(UNIT = 32)
    CLOSE(UNIT = 33)
    CLOSE(UNIT = 34)
    CLOSE(UNIT = 35)
    CLOSE(UNIT = 40)
    CLOSE(UNIT = 41)
    CLOSE(UNIT = 42)

!~~~~~~~~~~~~~~~~~~~~~~~~~~~~~~~~~~~~~~~~~~~~~~~~~~~~~~~~~~~~~~~~~~~~~~~~~~~~
! Deallocate memory for required arrays
!~~~~~~~~~~~~~~~~~~~~~~~~~~~~~~~~~~~~~~~~~~~~~~~~~~~~~~~~~~~~~~~~~~~~~~~~~~~~

    WRITE(*,*) "Deallocating required arrays..."
    WRITE(*,*) ""

    ! Deallocate EM field update arrays
    ! Magnetic fields
    DEALLOCATE(Hx,STAT=ierr,ERRMSG=merr)
    IF (ierr /= 0) THEN
        WRITE(*,*) "ERROR Hx Deallocation: ", merr
        STOP
    ENDIF
    DEALLOCATE(Hy,STAT=ierr,ERRMSG=merr)
    IF (ierr /= 0) THEN
        WRITE(*,*) "ERROR Hy Deallocation: ", merr
        STOP
    ENDIF
    DEALLOCATE(Hz,STAT=ierr,ERRMSG=merr)
    IF (ierr /= 0) THEN
        WRITE(*,*) "ERROR Hz Deallocation: ", merr
        STOP
    ENDIF

    ! Electric fields
    DEALLOCATE(Ex,STAT=ierr,ERRMSG=merr)
    IF (ierr /= 0) THEN
        WRITE(*,*) "ERROR Ex Deallocation: ", merr
```

```
    STOP
ENDIF
DEALLOCATE(Ey,STAT=ierr,ERRMSG=merr)
IF (ierr /= 0) THEN
    WRITE(*,*) "ERROR Ey Deallocation: ", merr
    STOP
ENDIF
DEALLOCATE(Ez,STAT=ierr,ERRMSG=merr)
IF (ierr /= 0) THEN
    WRITE(*,*) "ERROR Ez Deallocation: ", merr
    STOP
ENDIF

! Electric polarization current densities
DEALLOCATE(Jx,STAT=ierr,ERRMSG=merr)
IF (ierr /= 0) THEN
    WRITE(*,*) "ERROR Jx Deallocation: ", merr
    STOP
ENDIF
DEALLOCATE(Jy,STAT=ierr,ERRMSG=merr)
IF (ierr /= 0) THEN
    WRITE(*,*) "ERROR Jy Deallocation: ", merr
    STOP
ENDIF
DEALLOCATE(Jz,STAT=ierr,ERRMSG=merr)
IF (ierr /= 0) THEN
    WRITE(*,*) "ERROR Jz Deallocation: ", merr
    STOP
ENDIF

! Deallocate geometry array
DEALLOCATE(ID,STAT=ierr,ERRMSG=merr)
IF (ierr /= 0) THEN
    WRITE(*,*) "ERROR Geometry Deallocation: ", merr
    STOP
ENDIF

! Deallocate material property arrays
DEALLOCATE(MU_R,STAT=ierr,ERRMSG=merr)
IF (ierr /= 0) THEN
    WRITE(*,*) "ERROR Relative Permeability Deallocation: ",&
        merr
    STOP
ENDIF
DEALLOCATE(SIG_H,STAT=ierr,ERRMSG=merr)
IF (ierr /= 0) THEN
    WRITE(*,*) "ERROR Magnetic Loss Deallocation: ", merr
    STOP
ENDIF
DEALLOCATE(EPS_R,STAT=ierr,ERRMSG=merr)
IF (ierr /= 0) THEN
    WRITE(*,*) "ERROR Relative Permittivity Deallocation: ",&
        merr
    STOP
ENDIF
DEALLOCATE(SIG_E,STAT=ierr,ERRMSG=merr)
IF (ierr /= 0) THEN
    WRITE(*,*) "ERROR Electric Loss Deallocation: ", merr
    STOP
ENDIF

! Deallocate EM field update coefficient arrays
DEALLOCATE(Da,STAT=ierr,ERRMSG=merr)
IF (ierr /= 0) THEN
    WRITE(*,*) "ERROR Coefficient Deallocation: ", merr
    STOP
ENDIF
DEALLOCATE(Db,STAT=ierr,ERRMSG=merr)
```

```
IF (ierr /= 0) THEN
    WRITE(*,*) "ERROR Coefficient Deallocation: ", merr
    STOP
ENDIF
DEALLOCATE(Ca,STAT=ierr,ERRMSG=merr)
IF (ierr /= 0) THEN
    WRITE(*,*) "ERROR Coefficient Deallocation: ", merr
    STOP
ENDIF
DEALLOCATE(Cb,STAT=ierr,ERRMSG=merr)
IF (ierr /= 0) THEN
    WRITE(*,*) "ERROR Coefficient Deallocation: ", merr
    STOP
ENDIF

! Deallocate dispersive material model ADE coefficient arrays
DEALLOCATE(alpha,STAT=ierr,ERRMSG=merr)
IF (ierr /= 0) THEN
    WRITE(*,*) "ERROR Drude Model Deallocation: ", merr
    STOP
ENDIF
DEALLOCATE(beta,STAT=ierr,ERRMSG=merr)
IF (ierr /= 0) THEN
    WRITE(*,*) "ERROR Drude Model Deallocation: ", merr
    STOP
ENDIF

! Deallocate EM field update denominator arrays
DEALLOCATE(den_Hx,den_Ex,STAT=ierr,ERRMSG=merr)
IF (ierr /= 0) THEN
    WRITE(*,*) "ERROR Denominator Deallocation: ", merr
    STOP
ENDIF
DEALLOCATE(den_Hy,den_Ey,STAT=ierr,ERRMSG=merr)
IF (ierr /= 0) THEN
    WRITE(*,*) "ERROR Denominator Deallocation: ", merr
    STOP
ENDIF
DEALLOCATE(den_Hz,den_Ez,STAT=ierr,ERRMSG=merr)
IF (ierr /= 0) THEN
    WRITE(*,*) "ERROR Denominator Deallocation: ", merr
    STOP
ENDIF

! Deallocate 3D CPML discrete convolution field arrays
! x-axis
DEALLOCATE(psiHxz_b,STAT=ierr,ERRMSG=merr)
IF (ierr /= 0) THEN
    WRITE(*,*) "ERROR CPML Deallocation: ", merr
    STOP
ENDIF
DEALLOCATE(psiHxz_t,STAT=ierr,ERRMSG=merr)
IF (ierr /= 0) THEN
    WRITE(*,*) "ERROR CPML Deallocation: ", merr
    STOP
ENDIF

DEALLOCATE(psiExz_b,STAT=ierr,ERRMSG=merr)
IF (ierr /= 0) THEN
    WRITE(*,*) "ERROR CPML Deallocation: ", merr
    STOP
ENDIF
DEALLOCATE(psiExz_t,STAT=ierr,ERRMSG=merr)
IF (ierr /= 0) THEN
    WRITE(*,*) "ERROR CPML Deallocation: ", merr
    STOP
ENDIF
```

```
! y-axis
DEALLOCATE(psiHyz_b,STAT=ierr,ERRMSG=merr)
IF (ierr /= 0) THEN
    WRITE(*,*) "ERROR CPML Deallocation: ", merr
    STOP
ENDIF
DEALLOCATE(psiHyz_t,STAT=ierr,ERRMSG=merr)
IF (ierr /= 0) THEN
    WRITE(*,*) "ERROR CPML Deallocation: ", merr
    STOP
ENDIF

DEALLOCATE(psiEyz_b,STAT=ierr,ERRMSG=merr)
IF (ierr /= 0) THEN
    WRITE(*,*) "ERROR CPML Deallocation: ", merr
    STOP
ENDIF
DEALLOCATE(psiEyz_t,STAT=ierr,ERRMSG=merr)
IF (ierr /= 0) THEN
    WRITE(*,*) "ERROR CPML Deallocation: ", merr
    STOP
ENDIF

! Deallocate CPML discrete convolution field coefficient and
! property arrays
! z-axis
DEALLOCATE(bHz_b,cHz_b,STAT=ierr,ERRMSG=merr)
IF (ierr /= 0) THEN
    WRITE(*,*) "ERROR CPML Deallocation: ", merr
    STOP
ENDIF
DEALLOCATE(sigHz_b,alphaHz_b,kappaHz_b,STAT=ierr,ERRMSG=merr)
IF (ierr /= 0) THEN
    WRITE(*,*) "ERROR CPML Deallocation: ", merr
    STOP
ENDIF
DEALLOCATE(bHz_t,cHz_t,STAT=ierr,ERRMSG=merr)
IF (ierr /= 0) THEN
    WRITE(*,*) "ERROR CPML Deallocation: ", merr
    STOP
ENDIF
DEALLOCATE(sigHz_t,alphaHz_t,kappaHz_t,STAT=ierr,ERRMSG=merr)
IF (ierr /= 0) THEN
    WRITE(*,*) "ERROR CPML Deallocation: ", merr
    STOP
ENDIF

DEALLOCATE(bEz_b,cEz_b,STAT=ierr,ERRMSG=merr)
IF (ierr /= 0) THEN
    WRITE(*,*) "ERROR CPML Deallocation: ", merr
    STOP
ENDIF
DEALLOCATE(sigEz_b,alphaEz_b,kappaEz_b,STAT=ierr,ERRMSG=merr)
IF (ierr /= 0) THEN
    WRITE(*,*) "ERROR CPML Deallocation: ", merr
    STOP
ENDIF
DEALLOCATE(bEz_t,cEz_t,STAT=ierr,ERRMSG=merr)
IF (ierr /= 0) THEN
    WRITE(*,*) "ERROR CPML Deallocation: ", merr
    STOP
ENDIF
DEALLOCATE(sigEz_t,alphaEz_t,kappaEz_t,STAT=ierr,ERRMSG=merr)
IF (ierr /= 0) THEN
    WRITE(*,*) "ERROR CPML Deallocation: ", merr
    STOP
ENDIF
```

```
    WRITE(*,*) "Arrays deallocated successfully"
    WRITE(*,*) ""

    WRITE(*,*) "Exiting program"

END PROGRAM FDTD3D_DRUDE_PBC
```

SHAPES.f

```
!~~~~~~~~~~~~~~~~~~~~~~~~~~~~~~~~~~~~~~~~~~~~~~~~~~~~~~~~~~~~~~~~~~~~~~~~~~~~
!
! This file includes a group of FORTRAN functions used to place
! geometrical objects into the FDTD simulation space. Rectangles,
! spheres, cylinders and generic 2D polygons can be implemented.
!
! Cameron J. E. Straatsma
! MSc Student
! Electrical and Computer Engineering Department
! University of Alberta
! Edmonton, AB  T6G 2V4
! Canada
!
!~~~~~~~~~~~~~~~~~~~~~~~~~~~~~~~~~~~~~~~~~~~~~~~~~~~~~~~~~~~~~~~~~~~~~~~~~~~~

! Implement a cube structure
SUBROUTINE cube(center,length,mat_index,grid)
    IMPLICIT NONE

    INTEGER, DIMENSION(3), INTENT(IN) :: &
        center, length
    INTEGER, INTENT(IN) :: mat_index
    INTEGER, DIMENSION(:,:,:), INTENT(INOUT) :: grid

    INTEGER :: xmin, xmax, ymin, ymax, zmin, zmax
    INTEGER :: i, j, k

    xmin = center(1)-length(1)/2
    ymin = center(2)-length(2)/2
    zmin = center(3)-length(3)/2
    xmax = center(1)+length(1)/2
    ymax = center(2)+length(2)/2
    zmax = center(3)+length(3)/2

    DO k = zmin, zmax
        DO j = ymin, ymax
            DO i = xmin, xmax
                grid(i,j,k) = mat_index
            ENDDO
        ENDDO
    ENDDO

END SUBROUTINE cube

! Implement a sphere structure
SUBROUTINE sphere(center,radius,mat_index,grid)
    IMPLICIT NONE

    INTEGER, DIMENSION(3), INTENT(IN) :: &
        center
    INTEGER, INTENT(IN) :: &
        radius, mat_index
    INTEGER, DIMENSION(:,:,:), INTENT(INOUT) :: grid

    INTEGER :: xmin, xmax, ymin, ymax, zmin, zmax
```

```
    INTEGER :: ii,jj,kk
    INTEGER :: i, j, k

    xmin = center(1)-radius
    ymin = center(2)-radius
    zmin = center(3)-radius
    xmax = center(1)+radius
    ymax = center(2)+radius
    zmax = center(3)+radius

    DO k = zmin, zmax
        kk = ABS(center(3)-k)-0.5
        DO j = ymin, ymax
            jj = ABS(center(2)-j)-0.5
            DO i = xmin, xmax
                ii = ABS(center(1)-i)-0.5
                IF ((ii**2+jj**2+kk**2)**0.5 <= radius) THEN
                    grid(i,j,k) = mat_index
                ENDIF
            ENDDO
        ENDDO
    ENDDO

END SUBROUTINE sphere

! Implement a cylinder structure
SUBROUTINE cylinder(center,length,orientation,radius, &
    mat_index,grid)
    IMPLICIT NONE

    INTEGER, DIMENSION(3), INTENT(IN) :: &
        center
    INTEGER, INTENT(IN) :: &
        length, radius, mat_index
    CHARACTER, INTENT(IN) :: orientation
    INTEGER, DIMENSION(:,:,:), INTENT(INOUT) :: grid

    INTEGER :: xmin, xmax, ymin, ymax, zmin, zmax
    INTEGER :: ii,jj,kk
    INTEGER :: i, j, k

    IF (orientation == 'x') THEN

        xmin = center(1)-length/2
        ymin = center(2)-radius
        zmin = center(3)-radius
        xmax = center(1)+length/2
        ymax = center(2)+radius
        zmax = center(3)+radius

        DO k = zmin, zmax
            kk = ABS(center(3)-k)-0.5
            DO j = ymin, ymax
                jj = ABS(center(2)-j)-0.5
                DO i = xmin, xmax
                    IF ((jj**2+kk**2)**0.5 <= radius) THEN
                        grid(i,j,k) = mat_index
                    ENDIF
                ENDDO
            ENDDO
        ENDDO

    ELSE IF (orientation == 'y') THEN

        xmin = center(1)-radius
        ymin = center(2)-length/2
        zmin = center(3)-radius
        xmax = center(1)+radius
```

```
        ymax = center(2)+length/2
        zmax = center(3)+radius

        DO k = zmin, zmax
            kk = ABS(center(3)-k)-0.5
            DO j = ymin, ymax
                DO i = xmin, xmax
                    ii = ABS(center(1)-i)-0.5
                    IF ((ii**2+kk**2)**0.5 <= radius) THEN
                        grid(i,j,k) = mat_index
                    ENDIF
                ENDDO
            ENDDO
        ENDDO

    ELSE IF (orientation == 'z') THEN

        xmin = center(1)-radius
        ymin = center(2)-radius
        zmin = center(3)-length/2
        xmax = center(1)+radius
        ymax = center(2)+radius
        zmax = center(3)+length/2

        DO k = zmin, zmax
            DO j = ymin, ymax
                jj = ABS(center(2)-j)-0.5
                DO i = xmin, xmax
                    ii = ABS(center(1)-i)-0.5
                    IF ((ii**2+jj**2)**0.5 <= radius) THEN
                        grid(i,j,k) = mat_index
                    ENDIF
                ENDDO
            ENDDO
        ENDDO

    ENDIF

END SUBROUTINE cylinder

! Implement a 2D polygon structure
SUBROUTINE polygon2D(orientation,center,length,num_vert,vertices, &
    mat_index,grid)
!~~~~~~~~~~~~~~~~~~~~~~~~~~~~~~~~~~~~~~~~~~~~~~~~~~~~~~~~~~~~~~~~~~~~~~~~
!
! This function is an implementation of a points-in-polygon test.
! The code is a FORTRAN adaptation of the MATLAB function "inpoly"
! written by Darren Engwirda, copyright 2006. The original function
! can be found on the MATLAB Central File Exchange.
!
!~~~~~~~~~~~~~~~~~~~~~~~~~~~~~~~~~~~~~~~~~~~~~~~~~~~~~~~~~~~~~~~~~~~~~~~~
    IMPLICIT NONE

    INTEGER, INTENT(IN) :: &
        center, length, num_vert, mat_index
    CHARACTER, INTENT(IN) :: orientation
    INTEGER, DIMENSION(num_vert,2), INTENT(IN) :: &
        vertices
    INTEGER, DIMENSION(:,:,:), INTENT(INOUT) :: grid

    INTEGER :: xmin, xmax, ymin, ymax, zmin, zmax
    INTEGER, DIMENSION(num_vert,2) :: edge
    INTEGER, DIMENSION(:,:), ALLOCATABLE :: points
    LOGICAL, DIMENSION(:), ALLOCATABLE :: in, on
    INTEGER :: p1, p1min, p1max, p11, p12, p2, p2t, p21, p22, &
        n1, n2, start, lower, upper, i, j, k, n, nc

    IF (orientation == 'x') THEN
```

```
    xmin = center-length/2
    xmax = center+length/2
    ymin = MINVAL(vertices(:,1))
    ymax = MAXVAL(vertices(:,1))
    zmin = MINVAL(vertices(:,2))
    zmax = MAXVAL(vertices(:,2))

    ALLOCATE(points((ymax-ymin+1)*(zmax-zmin+1),2))

    n = 1
    DO k = zmin,zmax
        DO j = ymin, ymax
            IF (n <= SIZE(points,1)) THEN
                points(n,:) = [j,k]
                n = n+1
            ENDIF
        ENDDO
    ENDDO

ELSE IF (orientation == 'y') THEN
    xmin = MINVAL(vertices(:,1))
    xmax = MAXVAL(vertices(:,1))
    ymin = center-length/2
    ymax = center+length/2
    zmin = MINVAL(vertices(:,2))
    zmax = MAXVAL(vertices(:,2))

    ALLOCATE(points((xmax-xmin+1)*(zmax-zmin+1),2))

    n = 1
    DO k = zmin,zmax
        DO i = xmin, xmax
            IF (n <= SIZE(points,1)) THEN
                points(n,:) = [i,k]
                n = n+1
            ENDIF
        ENDDO
    ENDDO

ELSE IF (orientation == 'z') THEN
    xmin = MINVAL(vertices(:,1))
    xmax = MAXVAL(vertices(:,1))
    ymin = MINVAL(vertices(:,2))
    ymax = MAXVAL(vertices(:,2))
    zmin = center-length/2
    zmax = center+length/2

    ALLOCATE(points((xmax-xmin+1)*(ymax-ymin+1),2))

    n = 1
    DO j = ymin, ymax
        DO i = xmin, xmax
            IF (n <= SIZE(points,1)+1) THEN
                points(n,:) = [i,j]
                n = n+1
            ENDIF
        ENDDO
    ENDDO

ENDIF

DO n = 1, num_vert-1
    edge(n,1) = n
    edge(n,2) = n+1
ENDDO
edge(num_vert,:) = [num_vert,1]
```

```
n = SIZE(points,1)
nc = SIZE(edge,1)

ALLOCATE(in(n))
ALLOCATE(on(n))

in(:) = .FALSE.
on(:) = .FALSE.

DO i = 1, nc
    n1 = edge(i,1)
    n2 = edge(i,2)
    p21 = vertices(n1,2)
    p22 = vertices(n2,2)

    IF (p21 < p22) THEN
        p11 = vertices(n1,1)
        p12 = vertices(n2,1)
    ELSE
        p2t = p21
        p21 = p22
        p22 = p2t
        p11 = vertices(n2,1)
        p12 = vertices(n1,1)
    ENDIF

    IF (p11 > p12) THEN
        p1min = p12
        p1max = p11
    ELSE
        p1min = p11
        p1max = p12
    ENDIF

    IF (points(1,2) >= p21) THEN
        start = 1
    ELSE IF (points(n,2) < p21) THEN
        start = n+1
    ELSE
        lower = 1
        upper = n
        DO k = 1, n
            start = NINT(0.5*(lower+upper))
            IF (points(start,2) < p21) THEN
                lower = start
            ELSE IF (points(start-1,2) < p21) THEN
                EXIT
            ELSE
                upper = start
            ENDIF
        ENDDO
    ENDIF

    DO j = start, n
        p2 = points(j,2)
        IF (p2 <= p22) THEN
            p1 = points(j,1)
            IF (p1 >= p1min) THEN
                IF (p1 <= p1max) THEN

                    on(j) = on(j) .OR. (((p22-p2)*(p11-p1)- &
                        (p21-p2)*(p12-p1)) == 0)

                    IF ((p2 < p22) .AND. (((p22-p21)*(p1-p11)) &
                        < ((p2-p21)*(p12-p11)))) THEN
                        in(j) = .NOT. in(j)
                    ENDIF
                ENDIF
```

```
                ELSE IF (p2 < p22) THEN
                    in(j) = .NOT. in(j)
                ENDIF
            ELSE
                EXIT
            ENDIF
            in(j) = in(j) .OR. on(j)
        ENDDO
    ENDDO

    DO k = 1, n
        IF (in(k) .EQV. .TRUE.) THEN
            IF (orientation == 'x') THEN
                grid(xmin:xmax,points(k,1),points(k,2)) = &
                    mat_index
            ELSE IF (orientation == 'y') THEN
                grid(points(k,1),ymin:ymax,points(k,2)) = &
                    mat_index
            ELSE IF (orientation == 'z') THEN
                grid(points(k,1),points(k,2),zmin:zmax) = &
                    mat_index
            ENDIF
        ENDIF
    ENDDO

END SUBROUTINE polygon2D
```

Appendices References

[1] A. D. Rakić, A. B. Djurišić, J. M. Elazar, and M. L. Majewski, "Optical properties of metallic films for vertical-cavity optoelectronic devices," *Appl. Opt.*, vol. 37, no. 22, pp. 5271–83, 1998.

[2] K. S. Yee, "Numerical Solution of Initial Boundary Value Problems Involving Maxwell's Equations in Isotropic Media," *IEEE T. Antenn. Propag.*, vol. 14, no. 3, pp. 302–7, 1966.

[3] A. Taflove and S. C. Hagness, *Computational Electrodynamics: The Finite-Difference Time-Domain Method*, 3rd ed. Norwood, MA: Artech House, 2005.